Università degli Studi di Catania

International PhD in Chemical Sciences

XXVI Cycle

Graphene and Related Materials: from "Scotch-Tape" to Advanced Production Methods

Paola Russo

Supervisor:
Chiar.mo Prof. G. Compagnini

Coordinator:
Chiar.mo Prof. R. Purrello

PhD Thesis

A.Y. 2010-2013

To my Family

Index

Introduction

Nanotechnology is the act of purposefully manipulating matter at the atomic scale, otherwise known as the "nanoscale."

The name "nanotechnology" derives from the Greek words *nanos*, which means dwarf, and *technologia*, which means systematic treatment of an art. The term was coined in 1976, when Norio Taniguchi outlined his vision of atom-by-atom or molecule-by-molecule manipulation of matter for the semiconductor industry.

Nowadays nanotechnology is used to describe the creation and exploitation of materials with structural features in between those of atoms and bulk materials, with at least one dimension in the nanometer. The science and technology of nanomaterials have created great excitement and expectations in the last few years. By its very nature, the subject is of immense academic interest, having to deal with very tiny objects in the nanometer regime. There has been explosive growth of nanoscience and technology in the last decade, primarily because of the availability of new methods of

synthesizing nanomaterials, as well as tools for characterization and manipulation. Furthermore, there is a better understanding of the size-dependent electrical, optical and magnetic properties of individual nanostructures of semiconductors, metals and other materials.

The top-down and bottom-up approaches are the terms used to classify nanotechnology, based on the technique used for the production of the nanostructures. Top-down methods consist of size reduction of larger structures, while the basis of bottom-up approaches is the employment of atomic or molecular precursors as building blocks materials for the construction of new nanostructures.

The properties of materials with nanometric dimensions are significantly different from those of atoms or bulk materials. Suitable control of the properties of nanometer-scale structures can lead to new science as well as new products. Most properties of solids depend on the microstructure, i.e. the chemical composition, the arrangement of the atoms (the atomic structure) and the dimensionality that is one of the most defining material parameters. The same chemical compound can exhibit dramatically different properties depending on whether it is arranged in a zero-dimensional

(0D), one-dimensional (1D), two-dimensional (2D), or three-dimensional (3D) crystal structure. In other words, if one changes one or several of these parameters, the properties of a solid will vary.

In recent years, many nanomaterials with different size, shape and structure have been discovered; these materials can show a metallic behaviour, or be semi-conductive or insulators, resulting in advanced applications in various fields. For example carbon-based nanomaterials play an increasingly pervasive role in nanoscale science, thus because the variety of crystallographic forms of carbon places this element into the focus of attention both in terms of basic research as well as applications.

My research project, during my PhD in Chemical Sciences, was the synthesis and characterization of carbon-based nanomaterials. In particular, during the first year of my PhD, I focused my attention on the synthesis of graphene, a carbon-based nanomaterial arranged in a two-dimensional (2D) crystal structure. The main purpose of the study was to optimize the method of synthesis of graphene, using the “Scotch-tape” technique, to obtain greater amounts of graphene compared to samples consisting of several layers. Although this technique

leads to high quality graphene sheets, it is not the suitable approach to obtain a gram-scale production of graphene for its employment in nanoelectronics.

During the second year, my studies focused on the synthesis and characterization of graphene-based nanomaterials. In particular, I have dealt with graphene nanowalls (GNWs), which consist of few graphene layers vertically oriented on a suitable substrate. These materials have attracted the interest of many researchers due to their potential applications as cathode materials for field emission devices.

During the third and last year of my PhD, I studied the effects of ablation of a graphite target either with a nanosecond or a femtosecond laser, in liquids. In particular, I carried out my studies and experiments at the University of Catania and at the University of Waterloo (Canada) at the Department of Mechanical and Mechatronics Engineering, in the Centre for Advanced Materials Joining (CAMJ). It was found that the laser ablation of graphite can lead to the synthesis of large graphene domains employing the nanosecond laser, while the use of a femtosecond laser produces large amounts of porous graphene sheets, that are recovered at the water-air interface and the graphene quantum dots that are dispersed in the

liquid. These materials, the porous graphene and graphene quantum dots, are attracting the interest of all the scientific community due to their potential applications in many fields such as energy storage and water treatment, respectively.

The main purpose of my whole research across these years was the study of new methods for the synthesis of graphene-based nanomaterials in order to employ them in nanoelectronics and environmental-oriented fields.

Chapter 1. Carbon Materials

1.1. Carbon in Nature

Carbon (from the Latin language, *Carbo*, which means coal) as a non-metal element is the 15th most abundant element in the Earth's crust and the fourth most abundant element in the universe by mass after hydrogen, helium, and oxygen. The extraordinary ability of this chemical element to combine with itself and other chemical elements in different ways is the basis of organic chemistry and of life, since it is part of DNA, proteins and so on. It is precisely this chemical versatility, which allows having a vast amount of carbon-based structures. The element is found free in nature and itself is used as coke in steel making to reduce iron oxide to iron, as carbon black in printing, and as charcoal in sugar refining. Carbon is also important environmentally as carbon dioxide; it is about 350 parts per million of the atmosphere, plants take it in as they grow and it is dissolved in all natural waters. Carbon is a component of rocks as carbonates of calcium (limestone), magnesium, and iron. It is also found in

abundance in the sun, stars, comets, and atmospheres of most planets.

1.2. Carbon Compounds

The carbon element is the first element of column IV, in the periodic table, and its ground state electronic configuration is [(ls^2) ($2s^2 2p^2$)]. Out of its six electrons, four electrons in its valence shell form three hybridizations (sp, sp^2, sp^3) which lead to the formation of many stable carbon structures, allotropes, in all dimensions. The classification scheme of carbon allotropes based on the concept of the hybridization type of the valence orbitals of the carbon atoms and the relationship of different hybridized carbon allotropes is shown in Figure 1-1. Carbon, is capable to be very hard or very soft, it has the highest melting point among all the known elements. The use of this unique chemical element is almost unlimited from the hardest diamond for drilling to the softest form, graphite, for using it as a lubricant and in skin health and beauty. The three-dimensional forms of carbon, diamond and graphite, are widely known. However, in the last decades many exciting carbon nanomaterials have been discovered, and

intensively studied due to their unique structure, electronic, mechanical, optical, and chemical characteristics.

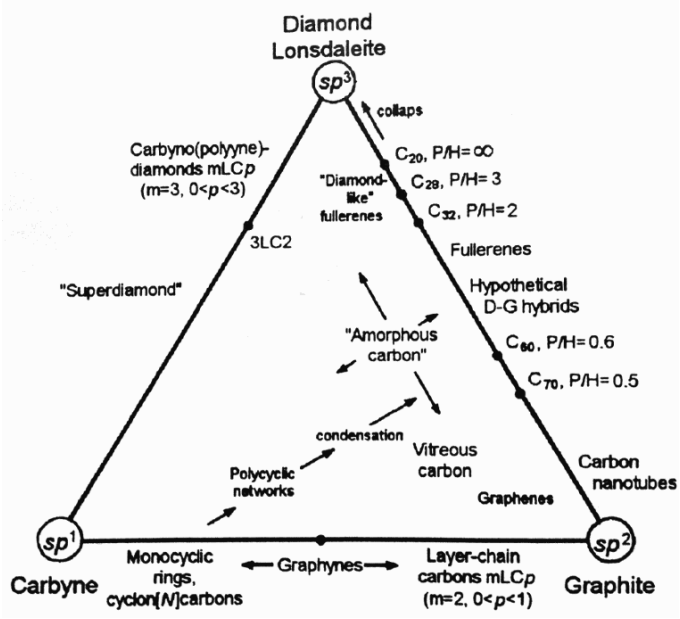

Figure 1-1: Classification of the carbon allotropes based on the type of hybridization and relationship between them. [Taken from ref. (1)]

The property of a bulk material is largely determined by the types of the constituent chemical elements and the nature of the chemical bonds that 'hold' the atoms and molecules together to form the material. However, this 'conventional wisdom' no longer holds in the nanometer regime in which, in addition to the chemical bonds, the size, dimensionality, and shape also play important roles in determining the properties

of the materials, especially the electronic, magnetic, and optical properties. The size matters when it becomes comparable to the length scale of a certain physical phenomenon that is concerned. Depending on their relative sizes in different spatial directions, carbon compounds can be divided into categories of different dimensionality ranging from 3D to 2D, 1D and 0D. The above classification is introduced for materials with simple shapes such as slabs/sheets (2D), wires/tubes/rods (1D), and cubes/spheres (0D).

The most known allotropes of carbon, as mentioned before are diamond and graphite, then to these must be added the other crystalline forms, that have different dimensionality from the 3D. These allotropes are the fullerenes and the graphene quantum dots (0D), the carbon nanotubes and the polyynes (1D), and graphene and the graphene-based materials (2D). The structures and chemical bonding of all these crystalline forms of carbon are reviewed in the next paragraphs. In the paragraph 1.7, the carbon-based hybrid nanomaterials will be discussed, where with the term “hybrid nanomaterials” we refer to a class of materials that are unique conjugates of two different structures and have found applications and appeals in many fields.

1.3. Carbon allotropes in 3D: Graphite and Diamond

Graphite and diamond are two different crystalline forms of the same element, and they exhibit different physical and chemical properties. If graphite can be is easily exfoliated, it is black, highly reflective and it behaves like a semimetal, the diamond on the contrary, is extremely hard, transparent and acts as an insulator. The main reason of these differences is related to the different crystal structure of the two allotropes. Graphite has a hexagonal crystal structure, and the basis of this crystal structure is the graphene plane, which is an extended hexagonal array of carbon atoms with sp^2-hybridazation. Graphite has two types of crystal forms: the hexagonal form and the rhombohedral one. The commonest and more stable form is the hexagonal, known also as *alpha*, where the stacking order of the layers is ABABAB..., shown in Figure 1-2. The rhombohedral form (or *beta*) with a stacking sequence ABCABC... is a minor component of well-crystallized graphite. The proportion of the *beta* form of graphite could be increased or decreased by deformation processes and by high temperature treatment, respectively (1). For both these crystal

forms of graphite the in plane C-C distance is 0.142 nm, an intermediate value between Csp^3- Csp^3 and Csp^2=Csp^2 bond lengths, 0.153 and 0.132 nm, respectively. Each C-C bond in the carbon layer plane has about one-third double bond character.

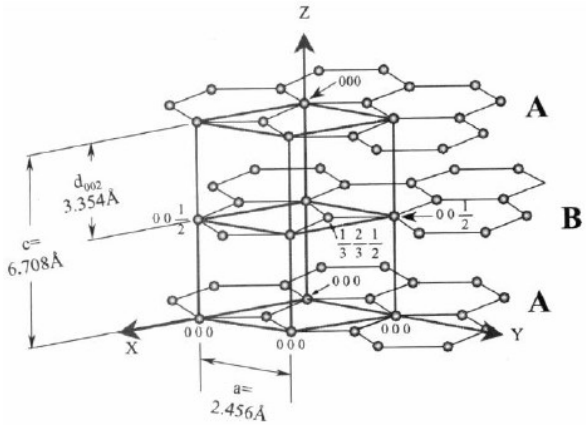

Figure 1-2: Crystal structure of the hexagonal graphite

The distance between two consecutive layers in graphite, interlayer distance, is 0.335 nm that results from a different type of bonding. It is well known that within the planes, the carbon atoms arranged in the hexagonal lattice are covalently bonded, while there is no unanimity regarding the nature of the interlayer bonding. The common assumption has been that the interlayer forces are of the van der Waals type, even if other authors define it cautiously as “a much weaker force

than the in-plane covalent bond". This could explain the easy exfoliation of graphite and its lubrication properties.

In diamond, the carbon atoms are arranged in a variation of the face-centred cubic crystal structure called a diamond lattice. Frequently diamond is found in a cubic form in which each carbon atom is linked to four other carbon atoms by sp^3 σ bonds in a strain-free tetrahedral array, as shown in Figure 1-3.

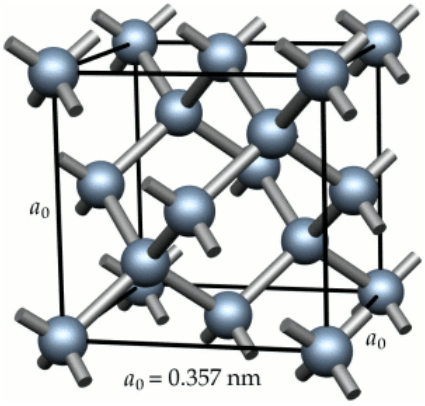

Figure 1-3: Crystal structure of diamond

The crystal structure is zincblende type and the C-C bond length is 0.154 nm. Diamond also exists in a hexagonal form (Lonsdaleite) with a Wurtzite crystal structure and a C-C bond length of 0.152 nm. Diamond is less stable than graphite, but the conversion rate from diamond to graphite is negligible at

ambient conditions. Most natural diamonds form at high-pressure and high-temperature conditions existing at depths of 140 to 190 kilometers in the Earth mantle.

Diamonds have been adapted for many uses because of the material's exceptional physical characteristics. Most notable are its extreme hardness and thermal conductivity (900– 2,320 $W \cdot m^{-1} \cdot K^{-1}$), as well as wide bandgap and high optical dispersion. Above 1,700 °C in vacuum or oxygen-free atmosphere, diamond converts to graphite; in air, transformation starts at ~700 °C. In diamonds, the bonds form an inflexible three-dimensional lattice, whereas in graphite, the atoms are tightly bonded into sheets, which can slide easily over one another, making the overall structure weaker.

1.4. Carbon Allotropes in 0D: Fullerenes and Graphene Quantum Dots

H. Kroto and R. Smalley (2) discovered fullerenes, C_{60} molecules, in the mass spectrum of laser-ablated graphite in 1985. The experiments that led to the discovery of the fullerenes aimed at understanding the mechanism by which long-chain carbon molecules formed in interstellar space and circumstellar shells. It was only in 1990 (3) that crystals of C_{60}

molecules were isolated from soot formed from graphite arc electrodes. The C_{60} structure is also known as Buckminsterfullerene, because of its resemblance to the geodetic domes built by R. Buckminster Fuller.

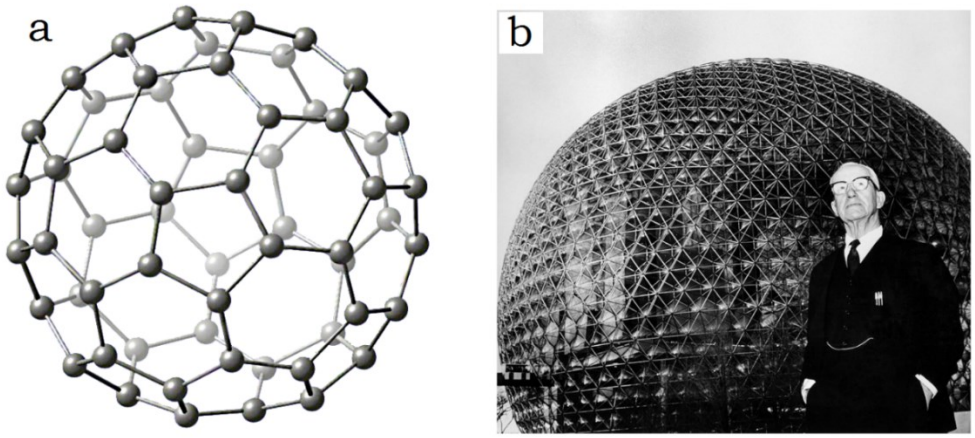

Figure 1-4: a) Crystal structure of C_{60}; b) geodetic dome built by R. Buckminster Fuller

The C_{60} molecule shows a regular truncated icosahedron structure consisting of 20 hexagons and 12 pentagons. The 60 carbon atoms in C_{60} are located at vertices of the truncated icosahedron and every carbon site is equivalent to every other site. The distance between the C-atoms and the centre of the molecule is about 3.55 Å, while the C-C bond length is 1.44 Å that is almost identical to that in graphite 1.42 Å. In the

fullerene, each carbon atom is trigonally bonded to three nearest-neighbour carbon atoms and it can be regarded as derived from the wrapping of a graphene sheet (single layer of crystalline graphite).

Beside the C_{60} structure, during its synthesis it is possible to form larger molecular weight fullerenes C_n (n>60). The most abundant is the C_{70} even if sufficient quantities of C_{76}, C_{78} and C_{84} are found. The crystal structures of these molecules are more complex than that of the C_{60} molecules. The C_{70} molecule shows an ellipsoidal crystal structure, presents D_{5h} symmetry, and contains 37 faces (25 hexagons and 12 pentagons) with a carbon atom at the vertices of each polygon and a bond along each polygon edge, Figure 1-5. Its structure is similar to that of C_{60} molecule but has a belt of six hexagons inserted at the equator. The molecule has eight bond lengths ranging between 1.37 and 1.46 Å. Each carbon atom in the structure is bonded covalently with three others (4). At high temperature (T >> 340 K), the fcc phase (a=15.01 Å) of C_{70} with freely rotating molecules is most stable, but since the ideal hexagonal close packed (hcp) phase with c/a= 1.63 is almost equally stable, fcc crystals of C_{70} tend to be severely twinned and show many stacking faults. A transition to another hcp phase with

a=b=10.11 Å and a larger c/a ratio of 1.82 occurs at about 340 K. The higher mass fullerenes (C_{76}, C_{84}), with multiple isomers of different shapes, also crystallize in the fcc structure at room temperature, with an fcc lattice constant which is approximately proportional to $n^{1/2}$, where n is the number of carbon atoms in the fullerene (1).

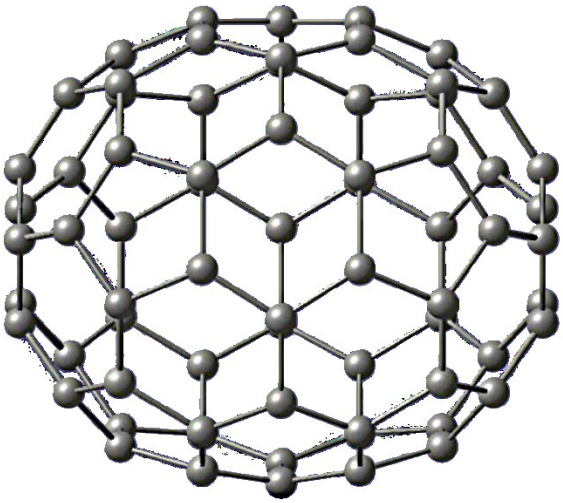

Figure 1-5: Crystal structure of C_{70}

In the past few years, another zero-dimensional form (OD) of carbon has attracted and continues to attract the interest of many research groups. In particular, we can indicate it as "the zero-dimensional form of graphene", which are called "graphene quantum dots". During the past years, these 0D

forms have been much less studied than graphene, carbon nanotubes and fullerenes, but recently, there has been significant advancement in both the theoretical and experimental fronts. The increasing interest towards graphene quantum dots (GQDs) is related to their unique optical and electronic properties due to their quantum confinement and edges effects.

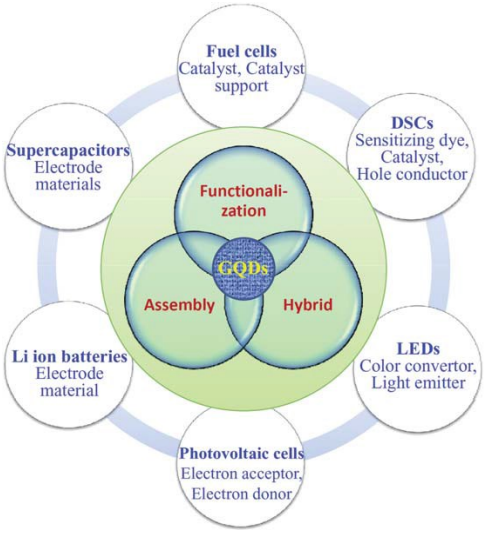

Figure 1-6: Applications of graphene quantum dots [Taken from ref. (5)]

Their properties differ from those of 2-D graphene and have great potential for a variety of applications principally in photovoltaic devices (6) and bio-related applications such as fluorescence labelling and bio-imaging (7). The common way to

describe the graphene quantum dots is referring to them as graphene sheets (less than 10 layers in thickness) whose dimensions are in the range from few nm to ~100 nm, as quantum confinement effect has been clearly observed in graphene dot of 110 nm in diameter (8).

1.5. Carbon Allotropes in 1D: Carbon Nanotubes and Polyynes (Carbynes)

In 1991, during the study of the surface of some carbon electrodes used in the manufacture of fullerenes (9) in an arc discharge tube, Iijima noticed the presence of structures consisting of several concentric tubes of carbon; the so-called "carbon nanotubes" were discovered. This new "nano-allotrope" of carbon consists of two separate regions with different physical and chemical properties. The first is the sidewall of the tube and the second is the end cap of the tube, which presents a structure similar to fullerene C_{60} (10). The structure of carbon nanotubes (CNTs) can be thought deriving from the cylindrical folding up of graphene sheets (honeycomb lattice of carbon atoms) with a wide range of diameters between 1 and over 80 nm (depending on the number of walls comprising the nanotubes) and with a length that exceeds 10

μm. The length to diameter ratio is about 1000 for most of the CNTs, so they are considered as one-dimensional structures (1D). Therefore, these materials are expected to possess additional interesting electronic, mechanical and molecular properties.

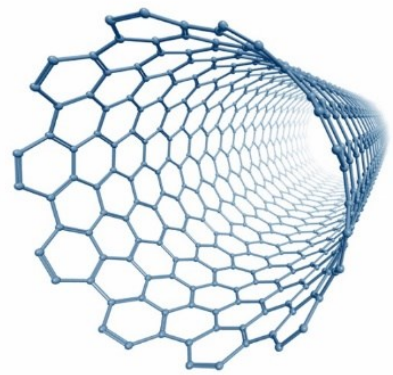

Figure 1-7: Structure of a carbon nanotube

Carbon nanotubes are distinguished depending on the number of graphene sheets comprising the nanotubes. In particular, carbon nanotubes composed of one graphene sheet are labelled as single-wall carbon nanotube (SWCNTs or SWNTs), those made of two graphene sheets as double-wall carbon nanotubes (DWCNTs or DWNTs), while the multi-wall carbon nanotubes (MWCNTs or MWNTs) are composed of many graphene sheets.

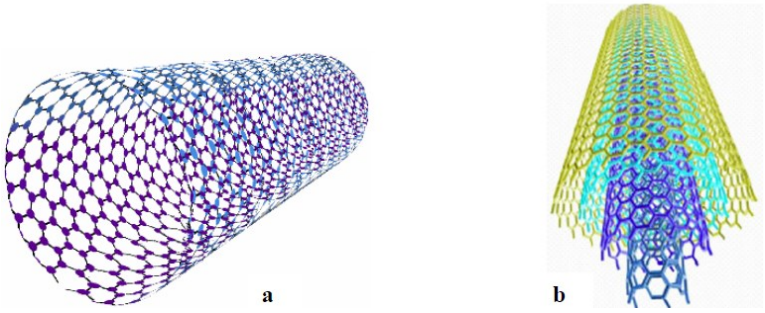

Figure 1-8: Structure of: a) SWCNTs, b) MWCNTs

One of the most interesting features of carbon nanotubes is that they could exhibit either metallic or semiconducting behaviour depending only on diameter and helicity of the arrangement of graphitic rings in their walls (11; 12).The graphene sheets can be rolled up in different ways, which lead to various helical structures. Precisely, the vector connecting two crystallographically equivalent lattice points (the points O and A in the Figure 1-9) in an unrolled honeycomb lattice, i.e. the graphene sheet, defines the structure of a carbon nanotube. When the two points coincide (aim achieved by the rolling up of the graphene sheet), a tube with a circumference corresponding to the line AO is produced. The vector connecting the two lattice points, A and O, in an unrolled graphene sheet is called the *chiral vector*, and it is

perpendicular to the tube axis. The *chiral vector* can be expressed with two fundamental translational vectors $\mathbf{a}_1$, $\mathbf{a}_2$:

$$\boldsymbol{C}_h = n\boldsymbol{a}_1 + m\boldsymbol{a}_2 \equiv (n,m)$$

Where n and m are integers with $0 \leq |m| \leq n$, and $\mathbf{a}_1$, $\mathbf{a}_2$ are the primitive unit cell vectors in the basal plane of the graphite structure.

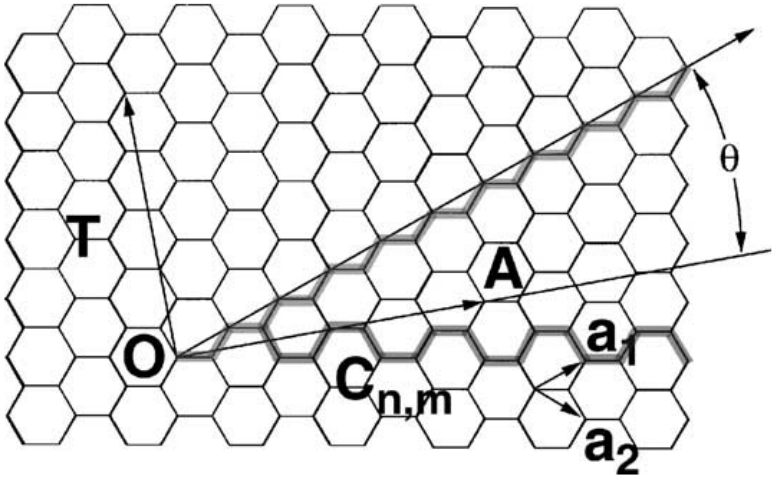

Figure 1-9: SWCNT geometry. Lattice vectors are denoted a_1 and a_2, while the OA vector is the C_h chiral vector. The θ angle is the chiral angle of the nanotube. [Taken from ref. (13)]

The structure of SWNTs is specified by the set of two integers (n, m) labelled as *chiral indices*. The diameter d_t and the chiral

angle θ, depicted in Figure 1-9, can be expressed in terms of n and m

$$d_t = \frac{a\sqrt{n^2 + nm + m^2}}{\pi}$$

$$\theta = \cos -1 \left(\frac{2n + m}{2\sqrt{n^2 + nm + m^2}} \right) \qquad \left(|\theta| \leq \frac{\pi}{6} \right)$$

Where $a = |\boldsymbol{a}_1| = |\boldsymbol{a}_2| = 0.246$ nm (14).

Depending on the chiral indices, the carbon nanotubes are distinguished in:

- *Armchair type*, when $n = m \left(\theta = \frac{\pi}{6} \right)$
- *Zig-zag type*, when $m = 0$ $(\theta = 0)$
- *Chiral type*, when $n \neq m \neq 0$

The different chiralities are shown in Figure 1-10.

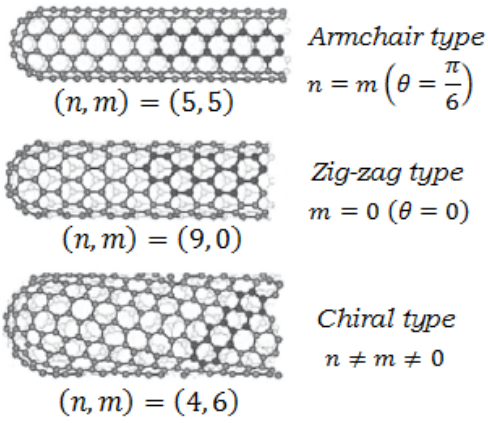

Figure 1-10: Different chirality of SWNTs

The diameter of the SWNTs depends on the synthesis conditions and especially on the diameter of the catalyst particles employed for the synthesis (14), and it ranges from 0.7 to 3 nm. The MWNTs, as mentioned before, consist of many graphene sheets (from 2 to about 40) rolled up, their diameters are in the range of 4-50 nm and their lengths are around 10 μm. The interlayer distance between the rolled graphene sheets is 0.344 nm that is 2.5% wider than the value presented by the graphite (0.3354 nm).

For what concern the electrical properties of the CNTs, the electronic band structure calculations predict that the (*n*, *m*) indices determine the metallic or semiconducting behaviour of SWNTs. When $n - m = 3j$, where j is an integer, the tube is

metallic, otherwise when $n - m \neq 3j$ the tubes are semiconductors.

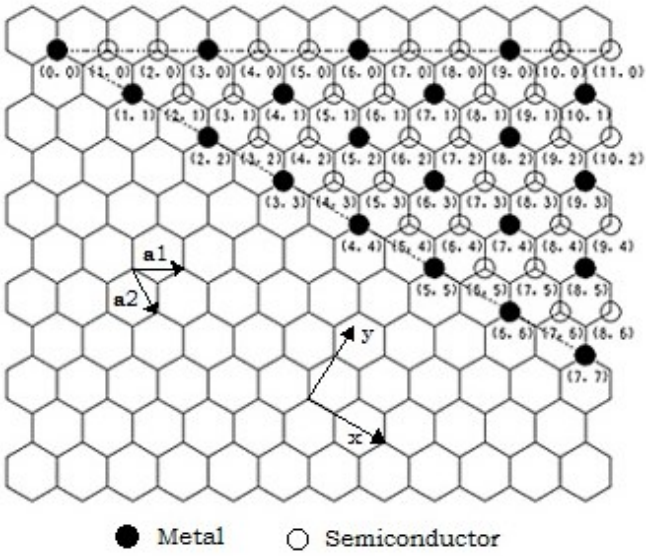

Figure 1-11: Electrical behaviour of SWNTs

The energy gap of semiconducting carbon nanotubes is inversely proportional to the diameter of the tube, and to be independent of the chiral angle θ. According to the tight bending calculation, the equation for the energy gap E_g is:

$$E_g = \frac{2\gamma a_{C-C}}{d_t}$$

Where γ is the nearest neighbour interaction energy, a_{C-C}= 0.142 nm being the carbon-carbon bond distance, and d_t is the nanotube diameter (15).

For what concern the electric properties, the carbon nanotubes exhibit quantum mechanical electric transport phenomena owing to their small size and structural perfection. The metallic CNTs can act as wires, while the semiconducting ones can be seen to act as transistors (14).

For their high stiffness, coupled with their low density, nanotubes might be useful as nanoscale mechanical parts. It is predict by theoretical estimates, that the carbon nanotubes possess a Young's modulus of the order of 1 TPa. Moreover, carbon nanotubes retain unusual strength in the large-strain region. The CNTs can be bent up to 110° without undergoing catastrophic fracture being extraordinarily flexible and resistant (14).

As mentioned in the previous paragraphs, due to the strong carbon-carbon chemical bonds and to the light mass of carbon atoms, carbon materials such as graphite and diamond show the highest thermal conductivity among materials. Phonons (lattice vibrations) are the major and exclusive carriers of heat for graphite and diamond, respectively. Since, the thermal

conductivity of a material strongly depends on the grain sizes in the sample, CNTs exhibit a thermal conductivity equal or higher than those of graphite parallel to the basal planes (~3000 W $(m \cdot K)^{-1}$ at 100 K) and natural diamond (~10^4 W $(m \cdot K)^{-1}$ at 80 K), due to their high crystallinity and directionality (14).

The other one-dimensional carbon allotropes are the carbynes, which are linear chains of carbon atoms. In particular, carbyne is supposed to occur in two isomeric forms: the polyynes and the polycumulene. The carbon atoms in the polyynes present conjugated $C(sp^1) \equiv C(sp^1)$ bonds, while the polycumulenes possess cumulated $C(sp^2) \equiv C(sp^2)$ double bonds.

El Goresy and Donnay (16) first discovered polyynes in 1968; in their work, they call this new form of carbon as "white carbon" or *Chaoite*, which presents a hexagonal crystal structure. At the same time, other two groups published a series of papers reporting the discovery of other carbyne forms with hexagonal structures named as *Carbon-VI*, *VII*, *IX* etc. formed in experiments involving attempts to vaporize graphite at 2550 K and low pressure (17; 18), and by

dehydropolymerisation of acetylene: *a-carbyne* and *ß-carbyne* (19; 20).

Table 1. Crystal structure data for some carbynes

Carbyne	*Chaoite*	*a-carbyne*	*ß-carbyne*	*Carbon VI*
Structure[a]	hex	hex	hex	rhomb.
a_0/pm	895	894	824	923
c_0/pm	1408	1536	768	1224
Density[b]	3.43	2.68	3.13	
Ref.	(16)	(19) (20)	(19) (20)	(17) (18)

a-hex= hexagonal, rhomb.= rhombohedral; b= $g \cdot cm^{-3}$

Table 1: Lattice parameters for some of these carbyne forms [Adapted from ref. (1)]

Despite many publications on carbynes, the acceptance of the existence and significance of polyynes is still a slow process. This skepticism is related to the fact that polyynes are unstable; they have a strong tendency to be oxidized by the oxygen that causes their destruction (21; 22; 23). Moreover, because the carbyne structure requires stabilization, these linear carbon chains lean to undergo chain-chain cross-linking reaction towards sp^2 graphene structures as a final product

(21), avoiding the possibility to isolate carbynes as large crystal forms.

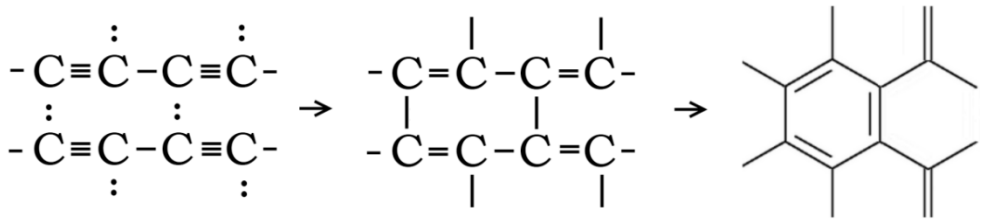

Figure 1-12: Chain-chain cross-linking reaction of polyynes [Adapted from ref. (21)]

Polyynes have been studied in the gas phase and they have been found in the interstellar molecular clouds (24; 25). Different routes can artificially produce these linear carbon chains. Some are listed below: the oxidative dehydropolycondensation of acetylene, the polycondensation of carbon sub-oxide with bis(bromomagnesium) acetylide, reactions based on the chemical transformations of polymers (dehydroalogenation of halogen-containing polymers, defluorination of polytetrafluoroethylene, dehydrogenation of polyacetylene, condensation of carbon vapour produced by various techniques, e.g., laser ablation of graphite and arc discharge (26).

During the last years, a series of papers were published regarding the possibility for the creation of new materials based on carbynes. First all, carbynes are semiconducting materials and this feature opens up prospects for creation of a new element basis for microelectronics based on carbon only. Secondly, carbyne is a high-temperature phase of carbon, which is stable at T>2000°C. It is distinguished from other carbon materials by its stability with respect to the formation of compounds with hydrogen; this makes polyynes very promising for application as the material of the first wall in devices for controlled thermonuclear fusion. Moreover, it is found that carbyne has a potential application in medicine due to its high biocompatibility and no toxicity. In particular, carbyne-containing polymers materials could be employed in reconstructive surgery, thus because they can be implanted into living organisms and be in contact with native blood for a long time. These materials are available as fibers, films or the coating bearing the carbyne surface layer, which serves as a protective coating (26).

1.6. Carbon allotropes in 2D: Graphene and Graphene-based materials.

In the last 30 years, there have been numerous reports studying the 0D, 1D and 3D materials, although it is in the 2D systems that the top-down and bottom-up approaches of the nanotechnology are currently being developed. Noteworthy, research works based on the synthesis of 2D materials, as isolated forms, are dated from the past ten years.

More than 70 years ago, Landau and Peierls argued that strictly two-dimensional (2D) crystals were thermodynamically unstable and are not possible to exist. Their theory pointed out that a divergent contribution of thermal fluctuations in low-dimensional crystal lattices should lead to such displacements of atoms as they become comparable to interatomic distances at any finite temperature. The argument was later extended by Mermin and has been strongly supported by many experimental observations. Indeed, the melting temperature of thin films rapidly decreases with decreasing the thickness, and they become unstable (segregate into islands or decompose) at a thickness of, typically, dozens of atomic layers. For this reason, atomic monolayers have so far been known only as an

integral part of larger 3D structures, commonly grown epitaxially on top of monocrystals with matching crystal lattices.

Graphite, as described previously, is a layered material with strong in-plane bonds, however the van der Waals-like couplings between the layers weaken the structure. Because of this layered structure, many researchers tried to split such materials into individual atomic layers, although it remained unclear whether freestanding atomic layers could exist in principle. This common knowledge was contradicted in 2004 by the experimental discovery of graphene by Geim and Novoselov (27) and other freestanding 2D atomic crystals such as the graphene nanowalls (28; 29) and the single layers of boron nitride (30).

The most intriguing material, among the aforementioned 2D forms of carbon, is graphene (Chapter 2). It is a monolayer of sp^2-bonded carbon atoms arranged in a honey carbon lattice. Since its discovery in 2004 (27), it has revolutionized all the scientific field due to its exceptional electrical, physical and chemical properties and its discoverers (Geim and Novoselov) earned the Nobel Prize in Physics in 2010. The promising

applications of this exceptional material have opened up new opportunities for future devices and systems.

It was reported, that modifying the structure of graphene (basal planes or edges) it is possible to improve the graphene properties, so the interest towards the fabrication of new graphene-based materials is growing among many research groups. These new types of materials can be employed for the design of nanoscale transistors (31), gas sensors (27), fuel cells (32), solar cells (33), organic light-emitting diodes (OLEDs) displays (34), and bio-related sensors (7). Many works are focusing on the synthesis of graphene nanowalls (GNWs), which are two-dimensional carbon nanostructures standing vertically on a substrate and they are considered one of the most promising graphene-based materials used in nanoelectronics as field emitters (35), (36). Recently, is growing the scientific interest towards other graphene-based materials such as porous graphene (PG) and graphene quantum dots (GQDs). The former is described as a graphene sheet with some carbon atoms vacancies (holes/pores) in the plane, while the latter are zero-dimensional materials and can be regarded as small fragments of graphene sheets with dimensions less than 100 nm. Both these materials are attracting the interest

of many researchers for their unique properties. For instance, porous graphene for its particular spongy structure has been suggested as a suitable membrane for gas separation (37), energy storage (38; 39), and as a basic material in nanoelectronics applications (40; 41). Otherwise, graphene quantum dots have potential applications in photovoltaics, water treatment (42) and in bio-related applications (7). These graphene-based materials will be discussed in depth in the next chapters.

1.7. Hybrid Nanomaterials: Definition

Products and their properties have to meet increasingly high and complex requirements. They are expected to offer a wide range of functions, weight as little as possible, be easy to handle and cost little to buy and maintain. This cannot always be achieved to the desired extent using classic materials. Scientists and engineers realized on, that mixtures of materials can show superior properties compared with their pure counterparts. It was only at the end of the 20th and the beginning of the 21st century that it was recognized by scientists, due to the availability of novel physical–chemical characterization methods, that the field of nanoscience could

open many perspectives for approaches to new materials. The combination of different analytical techniques gives rise to novel insights into hybrid nanomaterials and makes it clear that bottom-up strategies from the molecular level towards materials' design will lead to novel properties in this new class of materials.

If we have to give an answer to the common question: "what is a hybrid nanomaterial?" we can state that hybrid nanomaterials are unique conjugates of two different structures. In particular, the term hybrid in a simplistic manner, as reported by Bhanu P. Chauhan (43), means fusion, union, or combination of the features, into one monolithic identity to exploit the advantages of combined features and to negate the disadvantages of the individual components. Makisima (44) defined hybrid materials as mixtures of two or more materials with newly formed chemical bonds. The categorization of hybrid materials and their related materials was proposed as follows:

1. *Composites:* Mixture of materials consisting of matrix and micron-level dispersion
2. *Nano composites*: Sub-micron level mixture of similar kinds of materials

3. *Hybrids:* Sub-micron level mixture of different kinds of materials
4. *Nano-hybrids:* Atomic or molecular level mixture of different materials with chemical-bonds between their different materials

Makisima explained that the difference between hybrids and nano-hybrids was not so obvious, and that nanocomposites include hybrids and nano-hybrids in many cases. On the other hand, Ashby (45) defined hybrid materials as "a combination of two or more materials in a predetermined geometry and scale, optimally serving a specific engineering purpose". Hagiwara and Suzuki (46) described hybrid materials as an intentional combination of two or more materials, complimenting each other to have super-functions or new functions, which component materials did not possess. According to their criterion, the difference between hybrid materials and composites lies in their functions and/or properties, specifically hybrid materials are presumed to show superior functions or properties comparing to traditional composites.

Although there is no a single definition for these materials, unique is the idea that drives many researchers to the synthesis of these hybrid materials, namely the creation of this

new class of materials leads to fusion of the desired properties with the elimination of undesired behaviour providing an appealing property profile for such materials. For this reason, these materials have many potential applications in various fields even though their original components might not have been considered for those applications (43).

1.8. Carbon-based Hybrid Nanomaterials

Physical properties of carbon based nanomaterials (i.e., fullerenes, carbon nanotubes, polyynes and graphene) are an attractive platform for applications in optoelectronics and photovoltaics. They can act as semiconductors, metals, and dielectrics. Moreover, these materials can be transparent or opaque, and their surfaces may be passive (basal planes of graphite) or chemically active (edge planes of graphite). Thus, numerous variations of mechanical, electrical, or chemical properties can be achieved by using carbon nanomaterials and controlling their structure and surface chemistry, i.e. the band gap of semiconducting nanotubes or nanodiamonds can be tuned by changing the size and/or the doping elements.

As aforementioned, combinations of these carbon materials can create new carbon-based hybrid materials, enlarging the

area of their applications. For example, solar cells based on mixture of carbon nanotubes and carbon fullerenes (47) demonstrated enhanced efficiency, while SWCNTs filled with fullerenes (48; 49) have been realized and are expected to have a crucial influence in computing architectures.

In the next three sub-paragraphs, it will be briefly discussed about three carbon-based hybrid nanomaterials: the fullerene@SWNTs (Fullerene Peapods), the polyynes@SWNTs and the polyynes@graphene. The last two types of carbon hybrids materials have been synthesized by my research group and me and the results have been already published (50; 51).

1.8.1. Fullerene@SWNTs

The Fullerene@SWNTs, also known as fullerene peapods, where synthesized for the first time by Smith et al. in 1998 during the pulsed laser vaporization of graphite in presence of metallic catalysts (52). In this type of hybrid material, the fullerenes C_{60} are encapsulated inside the nanotubes, as shown in Figure 1-13.

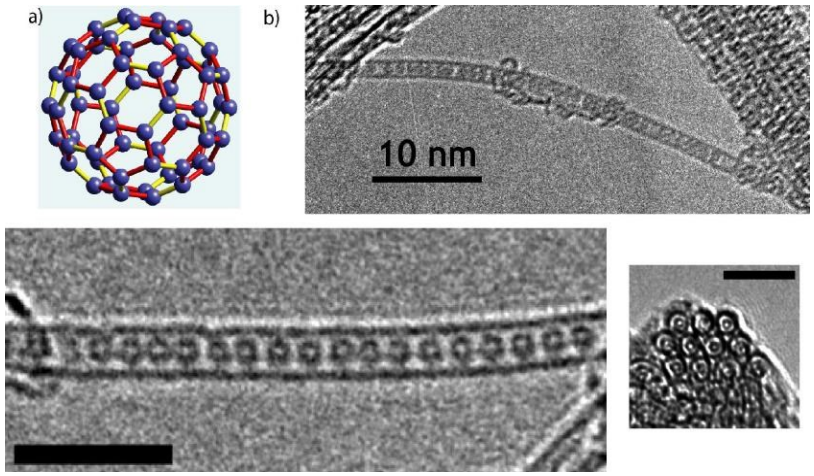

Figure 1-13: Fullerene@SWNTs. The figure shows the fullerenes molecules (a) trapped inside the nanotubes (b) [taken from http://www.stanford.edu/group/GGG/1D.html]

The fullerene peapods can be classified according to the type of their two constituents, the host nanotubes and the encapsulated fullerenes. The classification is given according to the type of: a) the nanotube; b) the fullerene and c) the arrangement of the fullerenes inside the nanotube (53).
According to the type of nanotube, we can have:

1. Fullerene@SWNTs as synthesized by Smith in 1998 (52).
2. Fullerene@MWNTs synthesized the first time in 2003 (54; 55).

3. Non-carbon nanotubes such as the multi-wall boron nitride nanotube peapods, synthesized in 2003 (56).

According to the type of fullerene, the classification is:

1. Pristine fullerene (C_{60}, C_{70}) (52)
2. Endohedral fullerenes (referring to the icosahedral C_{60} symmetry (57)), that is, Endohedral metallofullerenes (58; 59) and the $N@C_{60}$ fullerene (60)
3. Functionalized fullerenes (61)
4. Heterofullerenes (62; 63)
5. ^{13}C isotope enriched fullerene peapods (64)

According to the arrangement type, the encapsulated fullerenes can form a linear chain (52) or can organize themselves in a 'silo' configuration (56) in larger diameter nanotubes. Since their discovery, fullerene@SWNTs, have been widely studied due to their anticipated unique electronic properties and potential applications, e.g., in high temperature superconductors (65).

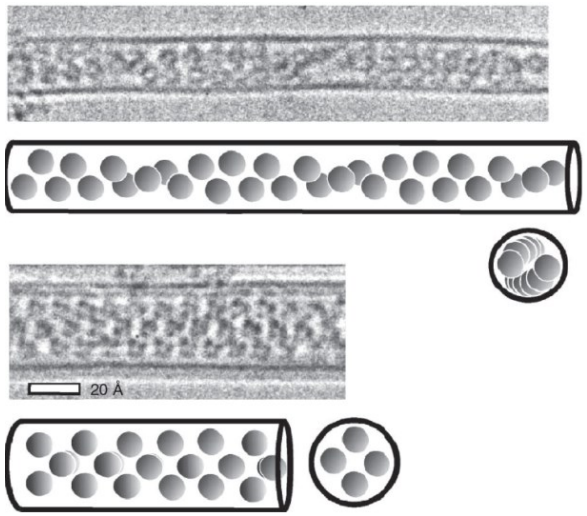

Figure 1-14: "silo" arrangement of fullerene peapods inside CNTs [taken from ref. (53)].

This type of carbon hybrid could be employed also as transistors; they can alone act as solar cells as they have the active medium as well as the electrode naturally integrated. Indeed, solar cells consist of an active medium, which provides an electron-hole pair upon light excitation, which are separated from each other with an electrode. Li et al. (66) in their work, reported that fullerenes encapsulated inside SWCNTs act as the active electron-hole producing medium.

1.8.2. Polyynes@CWNTs

In the 1.5 paragraph, it was mentioned that, polyynes are very unstable and they can easily undergo to degradation. Due to their conjugate π electrons, that are doubly degenerated, they are expected to be better candidates for molecular devices than the carbon nanowires (CNWs) because polyynes are smaller than CNWs. Moreover, it was found by Zhao et al. that CNWs are much more stable inside the inner tube of MWCNTs (67).

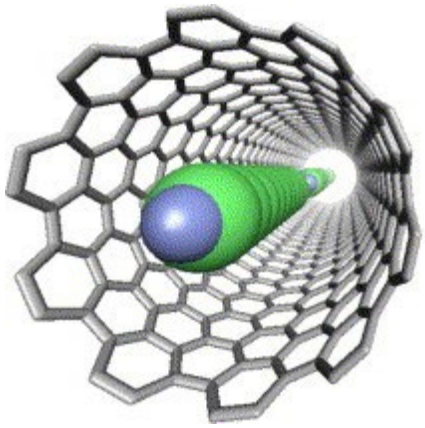

Figure 1-15: Polyynes@SWNTS [Taken from ref. (68)]

For this reason, it is plausible to hypothesize the stabilization of polyynes inside SWNTs, where the walls protect the

polyynes avoiding their destruction. The hybrid materials that result from the combination of polyynes and the SWNTs are commonly indicated as “polyynes@SWNTs”. A schematic model is shown in Figure 1-15. The polyynes@SWNTs were synthesized by Nishide and co-workers incorporating chromatographically purified $C_{10}H_2$ into SWNTs by the liquid-phase doping method (68). The evidence for the incorporation of the polyynes inside the SWNTs was provided by the Raman spectroscopy.

Raman spectroscopy is a powerful technique to study the vibrational properties of the carbon-based materials. In particular, it is very sensitive to the type of hybridization of the carbon atoms. The different carbon materials possess different Raman features that permit to distinguish them from each other. The sp-hybridized linear carbon chains, polyynes, generally show Raman bands around 1800-2100 cm^{-1}, related to the carbon triple bonds. The position of these bands varies with the length of the chain. In particular, it was predicted by Kastner (69) a shift of the bands to lower frequencies with increasing chain length. In the figure below are reported the Raman spectra, taken from ref. (68), of the pristine SWNTs (black line) and the one relative to the hybrid material made of

polyynes inside the SWNTs (red line). In particular, the signal at 2066 cm^{-1}, is associated with the vibrational frequency of sp-carbon bonds in the polyyne molecules and it is consistent with the presence of trapped polyynes inside SWNTs.

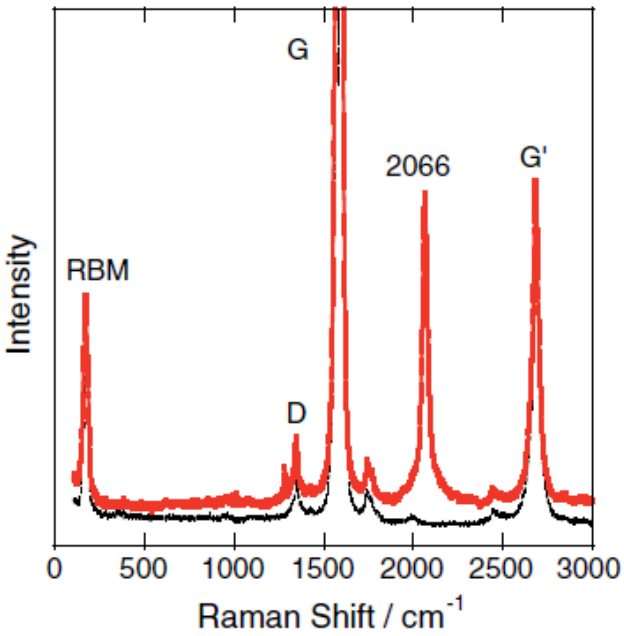

Figure 1-16: Raman spectra of pristine SWNTs (black line) and of polyynes@SWNTS hybrid material [Taken from ref. (68)].

In 2010 my research group and me, we were successfully able to synthesize polyynes inside multiwall carbon nanotubes (MWCNTs), also known as polyynes@MWNTs (50).

The hybrid materials were produced by arc discharge of two graphitic electrodes submerged in liquid nitrogen. During our experiments, we noticed that the experimental parameters influenced the structure properties of the materials produced. In particular, we found that the electrode size and the values of the discharge current play a key role on the quality of the nanotubes and on the type of nanotubes produced (CNTs and/or polyynes@MWNTs) (50). The analysis characterization of the systems obtained, such as Raman and TEM confirmed the presence of linear carbon chains trapped inside the MWNTs as shown in Figure 1-17. The presence of the peak at ~1850 cm^{-1}, that is in the region of the sp-carbon bonds vibrational frequency (1800-2200 cm^{-1}) is consistent with the presence of trapped polyynes inside the MWNTs. If we compare the Raman spectrum we obtained analyzing our samples with the one obtained by Nishide (68), we can noticed that the peak at 1850 cm^{-1} is red-shifted, thus because, as aforementioned, theoretical studies suggest a red-shift of the sp Raman features with increasing chain length (69). Noteworthy, our results are consistent with the results reported by Zhao et al. (67), who first reported the presence of a carbon chain inside MWCNTs.

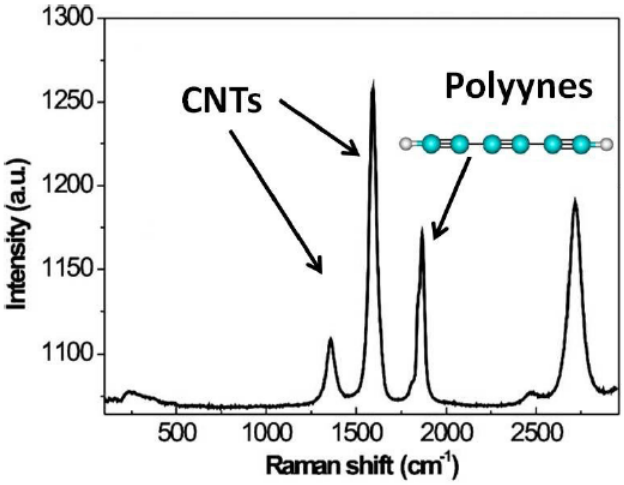

Figure 1-17: Raman spectrum of polyynes@MWNTs. [ref. (50)]

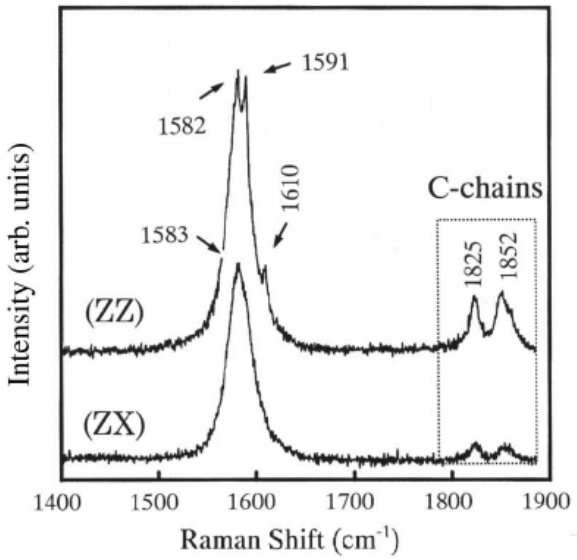

Figure 1-18: CNWs@MWNTs [taken from ref. (67)]

1.8.3. Polyynes@Graphene

Linear carbon chains, as mentioned in the previous paragraphs, are very unstable and they easily tend to undergo chain-chain cross-linking reactions towards more stable sp^2 phase and for such a reason it is very difficult to obtain Raman spectra of isolated and well-identified polyynes. For this reason, polyynes are usually investigated by SERS (Surface Enhanced Raman Scattering) that permits to enhance the signals of the polyynes with the use of silver nanoparticles, thus because the resulting enhancement of Raman cross sections can be attributed to the excitation of the surface plasmon resonance in the silver nanoparticles (70).

Recently, many works proposed graphene as a suitable substrate for SERS, due to its electronic structure, which can promote charge transfer phenomena. In particular, graphene could amplify the Raman signal for probe molecules at high bond conjugation, disposed parallel to the graphene surface, as reported by Ling (71) and Naumenko (72).

In order to investigate the potential application of graphene as a SERS substrate, in 2011 my research group and me, we produced a new sp-sp^2 hybrid carbon nanostructure composed of polyynes (1D) interacting with graphene layers (2D). When

the solution containing the polyynes was drop casted on the top of the graphene layers, we observed a remarkable change of the graphene electronic and phononic behavior after the interaction with the linear carbon chains.

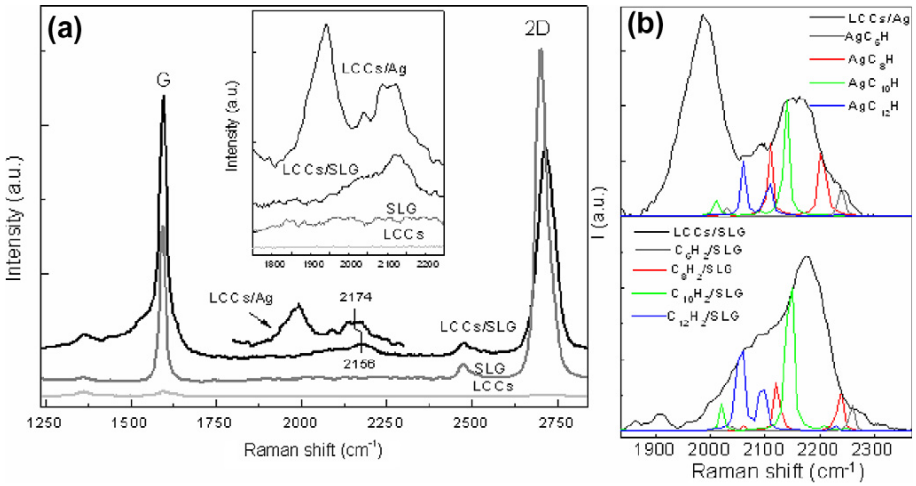

Figure 1-19: Experimental Raman spectra of LCCs deposited on single layer graphene (LCCs/SLG) compared with LCCs on silver nanoparticles (LCCs/Ag) and SLG spectra. Raman spectrum of LCC solution deposited on SiO2 is also shown for comparison. In the inset, a magnification of the 1700–2300 cm_1 region is shown. (b) Magnification of the 1800–2500 cm_1 region is shown for LCCs/Ag and LCCs/SLG and compared with DFT calculations of the Raman active modes of single chains HAC2nAHinteracting with Ag and SLG units [Taken from ref. (51)]

The SERS activity of graphene layers (SLG) towards the polyynes was examined in comparison with the other enhancer systems (silver colloids). If we look at the Raman spectra reported in Figure 1-19, we can see that the polyynes signals

without any enhancer system show only the signals relative to sp^2 phase, due to their tendency to interchain crosslinking when they are not stabilized. When polyynes were deposited on the top of a graphene layer, their signals were enhanced, thus confirming the possibility to use graphene as a SERS substrate (51).

Chapter 2. Graphene

2.1. What is Graphene

"Graphene", is the name given to the carbon allotrope made of a planar monolayer of carbon atoms arranged into a two-dimensional (2D) honeycomb lattice.

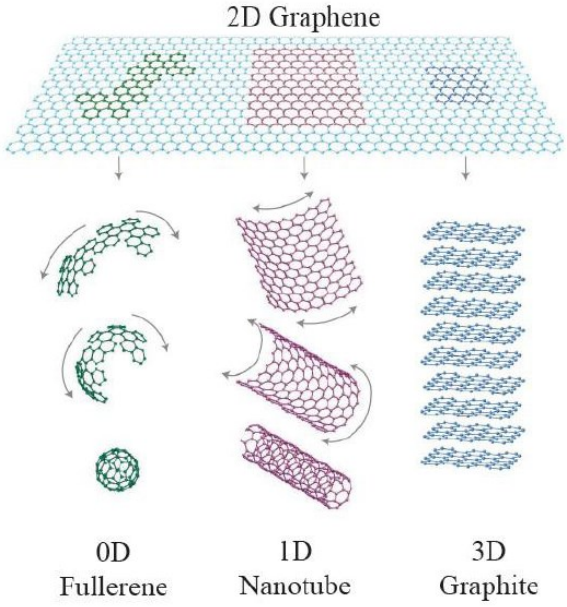

Figure 2-1: Graphene as the building block of the other carbon allotropes

Among the other carbon structures, graphene plays a very important role, as it is the basis for the understanding of the electronic properties in other allotropes, since it is considered as the building block of the other carbon allotropes. According to that common thought, fullerenes derive from the wrapping of graphene, while from its rolling up, the carbon nanotubes are obtained. The stacking of many graphene layers along the z-axis leads to the formation of graphite, as schematically showed in Figure 2-1. As mentioned in the previous chapter, graphene was studied theoretically for more than sixty years, and its existence was thought to be impossible, thus because it was believed that 2D materials did not exist without a 3D base. However, in 2004, the scientific world had to change his mind, when Geim and Novoselov demonstrated experimentally the existence of graphene (27). Such discovery has revolutionized the field of electronics owing to the excellent electronic and mechanical properties and chemical stability of graphene, which paves the way for many potential applications from nanoelectronics to the biochemical field.

2.2. Crystal Structure and Properties of Graphene

Graphene is a single layer of carbon atoms packed into a two-dimensional hexagonal crystal lattice. The lattice of graphene consists of two equivalent interpenetrating triangular carbon sublattices A and B, each one contains a half of the carbon atoms. The primitive cell of graphene is composed of two non-equivalent atoms (Figure 2-2), indicated as A (black circles) and B (white circles), each forming a triangular 2D network, but translated from each other by a carbon-carbon distance equal to $a_{C-C} = 1.42$ Å.

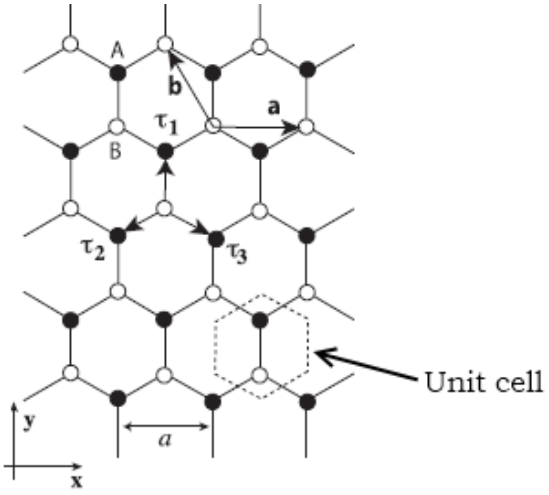

Figure 2-2: Honeycomb lattice of graphene [Adapted from ref. (73)]

The lattice vectors can be written as:

$$\mathbf{a}_1 = \frac{a}{2}(1, \sqrt{3}), \qquad \mathbf{a}_2 = \frac{a}{2}(1, -\sqrt{3}),$$

where $a = \sqrt{3}a_{C-C} = 2.46$ Å is the lattice constant.

The honeycomb structure is not a Bravais lattice because the atomic positions A and B are not equivalent, and for this reason, they cannot be connected with a lattice vector $\boldsymbol{R} = n_1\boldsymbol{a}_1 + n_2\boldsymbol{a}_2$, where n_1 and n_2 are integers. If we look only at the A atomic positions (or the B atomic positions) they make up a hexagonal Bravais lattice and researchers usually refer to them as the A sublattice (or B sublattice).
The primitive reciprocal lattice vectors $\mathbf{b}_1$ and $\mathbf{b}_2$, satisfying $a_1 b_1 = a_2 b_2 = 2\pi$ and $a_1 b_2 = a_2 b_1 = 0$ are given by

$$\mathbf{b}_1 = \frac{2\pi}{a}\left(1, \frac{1}{\sqrt{3}}\right), \qquad \mathbf{b}_2 = \frac{2\pi}{a}\left(1, -\frac{1}{\sqrt{3}}\right)$$

The resulting reciprocal lattice is shown in Figure 2-3, which is a hexagonal Bravais lattice. The first Brillouin zone (BZ) is

hexagonal as shown in the figure below and it has a side length of $4\pi/3a$.

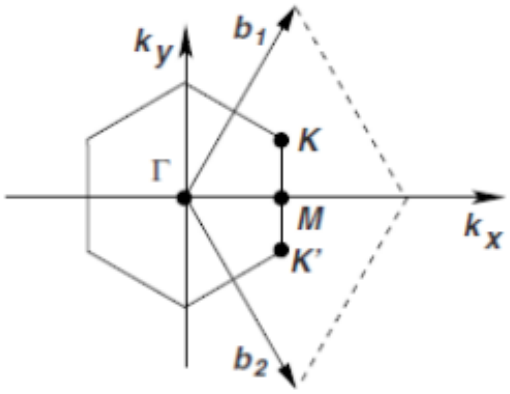

Figure 2-3: First Brillouin zone of graphene [Adapted from ref. (74)]

The corners of the first Brillouin zone are called K or K' points, which are also referred to as Dirac points, because the energy spectrum at these corners can be described by the mass less Dirac equation. Their positions in momentum space are given by:

$$\mathbf{K} = \left(\frac{2\pi}{3a}, \frac{2\pi}{\sqrt{3}a}\right), \qquad \mathbf{K'} = \left(\frac{2\pi}{3a}, -\frac{2\pi}{\sqrt{3}a}\right)$$

Each carbon atom within a single plane has three nearest neighbors: the sites of one sub-lattice (A –black circles) are at

the centers of triangles defined by tree nearest neighbors of the other one (B – white circles). The positions of the three nearest-neighbor vectors in real space are given by:

$$\boldsymbol{\tau}_1 = \frac{a}{2}\left(1, \sqrt{3}\right), \quad \boldsymbol{\tau}_2 = \frac{a}{2}\left(1, -\sqrt{3}\right), \quad \boldsymbol{\tau}_3 = -a(1, 0)$$

The structure of graphene, composed of two equivalent triangular carbon sublattices, has important consequences for the electronic properties of graphene. The ground-state electronic shell configuration of carbon atoms is $1s^2 2s^2 2p^2$. It has six electrons; four of them are valence electrons, while the other two are core electrons. In graphene, the carbon atoms have sp^2 hybridization, generated by the superposition of 2s orbitals with two of the 2p orbitals, the $2p_x$ and $2p_y$ orbitals precisely. These orbitals lie in the graphene plane; they are oriented 120° to each other and form the energetically stable and localized σ-bonds with the three nearest-neighbor carbon atoms in the honeycomb lattice. The remaining free $2p_z$ orbital for each carbon atom lies perpendicular to the plane and presents π symmetry orientation. The overlap of these orbitals states between neighboring atoms plays an important role in the electronic properties of graphene.

The band structure obtained from the tight-binding model produces symmetric conduction and valence bands with respect to the Fermi energy, also called the *charge neutrality point* or *Dirac point*, set at 0 eV. Since there is no band gap between the conduction and valence bands graphene is usually designated a semimetal material with no overlap or zero-gap semiconductor (75).

Since graphene was discovered, its electronic properties have attracted the interest of the researchers, who looked at graphene as substitute of silicon in the fabrication of electronic devices. However, the absence of an energy band gap that restricts its use for digital applications, lead many researchers for searching alternative strategies capable of inducing a band gap in graphene sheets. For example, chemical doping, interaction with substrates and the application of external electric/magnetic fields are only some of the strategies that have been proposed so far. Besides the fascinating electronic properties of graphene, also its outstanding mechanical properties have attracted interest for electronic applications, since graphene holds great promise as a building block in nanoelectro-mechanical systems (NEMS), which are devices integrating electrical and mechanical

functionality on the nanoscale. The name derives from typical device dimensions in the nanometer range, leading to low mass, high mechanical resonance frequencies, potentially large quantum mechanical effects such as zero point motion, and a high surface-to-volume ratio useful for surface-based sensing mechanisms (76). The materials utilized for the fabrication of these devices have been the carbon-based materials; in particular, researchers employed carbon nanotubes and graphene, because the properties of these materials meet the needs of NEMS. In fact, the mechanical properties of graphene, such as the large Young's modulus, are fundamental to the stability of NEMS, while its semiconductor activity allow graphene to function as transistors. Consequently, the study of the mechanical properties of graphene becomes crucial for the design and control of nanographene devices. The NEMS devices are functional only in response to an external applied force and it is beneficial to have the active element having as low mass as possible and as high of a quality factor as possible (77). The highest limit would be a one atom thick resonator and reaching this limit requires robustness, stiffness and stability of the material employed (78). Compared to silicon-based

materials, graphene is very strong and stiff and during these years, many researchers worked on the measurement of the Young's modulus of graphene with both experimental and molecular dynamics (MD) simulation approaches. The Young's modulus is a measure of the stiffness of a material, of graphene in this case, and together with the other two elastic parameters, the shear modulus and the Poisson's ratio, defines the mechanical properties of graphene. The value of the Young's modulus ranges from 0.5 TPa (79), measured using atomic force microscope (AFM), to 1.0 TPa calculated by Lee et al. (80), who measured the elastic properties and intrinsic breaking strength of free-standing monolayer graphene membranes by nanoindentation in an atomic force microscope, and their experiments established graphene as the strongest material ever measured.

2.3. Overview of the potential applications of graphene

All these outstanding properties of graphene render it a unique material, for which a cornucopia of potential applications has been proposed so far. Many researchers showed that modifying the surface of graphene (basal planes or edges) it is possible to

modify the properties of graphene in order to employ it for the design of nanoscale transistors (31), gas sensors (27), fuel cells, energy storage and organic light-emitting diodes (OLEDs) displays (34). Recently, some studies showed that the graphene-based OLEDs can increase the performance of indium tin oxide (ITO) compounds, used in transparent conductive electrodes (81), and also graphene would be better in terms of being more flexible, less fragile, and having the potential of being cheaper than ITO. Graphene is able to withstand more strain than materials such as ITO while retaining its electrical properties (34). Bae and coworkers in their study reported that while an ITO touch-screen broke under 2-3% strain, a graphene touch-screen withstood up to approximately 6% and was limited by the electrodes on the screen rather than by the graphene itself (34). Graphene can also be used in the medical field for the design of nanosensors that can lead to detect illnesses (82).

The widespread research into the properties and applications of graphene attests to the growing interest in this fascinating material. Graphene's strength and flexibility, together with its interesting charge carrier and other properties, can improve the existing technologies and can pay the way for the

development of new ones. In the next paragraphs, the different production techniques of graphene will be described.

2.4. Graphene synthesis

Since the discovery of graphene in 2004, several methods have been proposed for its synthesis. These methods consist of either top down approaches or bottom up ones. As a rule, the top-down methods consist of size reduction of larger structures, while the basis of bottom-up approaches is the use of atomic or molecular precursors as building blocks materials for the construction of new nanostructures. For the synthesis of graphene, the mechanical, chemical and laser exfoliation and the chemical synthesis can be categorized as top-down approaches. The unzipping of carbon nanotubes, the chemical vapor deposition (CVD) and the epitaxial growth are considered bottom-up methods. In Figure 2-4, a scheme of the methods commonly employed for the synthesis of graphene is presented. The developing of all these different ways to obtain graphene and the relentless pursuit of new methods, highlight the importance of having synthetic methods that can lead to a gram scale production of high quality graphene sheets in order to exploit its properties.

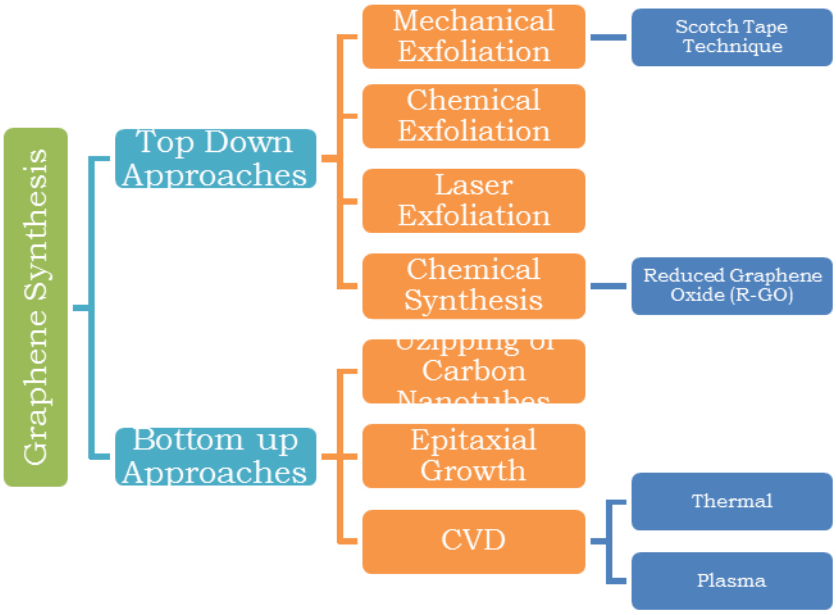

Figure 2-4: Approaches for the synthesis of graphene

However, the achieving of a gram scale and cheap method for the fabrication of graphene is still a challenge. In the upcoming paragraphs, some of the methods employed for the synthesis of graphene will be described.

2.4.1. Mechanical Exfoliation

The mechanical exfoliation of graphite, was the first recognized method employed by Geim and Novoselov for the synthesis of graphene, performed in 2004 (27). It is well-known, that the

stacking of many graphene layers along the c axis forms graphite. The interlayer distance is 3.34 Å and the layers are stacked together by weak van der Waals forces with interaction energy of about 2 eV/nm^2. The force required for the mechanical cleaving to detach one mono-atomic layer from graphite is ~300 nN/μm^2 (83), and this weak force can be easily achieved with an adhesive tape. In particular, in 2004 Geim and Novoselov first used an adhesive tape to detach a mono-atomic graphene sheet by a mechanical cleaving technique from a piece of highly oriented pyrolytic graphite (HOPG). The authors prepared graphite flakes of few millimeters that were then compressed against a layer of wet photoresist over a glass substrate. In order to attach the graphite flakes to the photoresist layer, the samples were baked. The detachment of graphene and few layer graphene was performed using an adhesive tape to peel off the graphite flakes and then the flakes were released in acetone. The layers were firstly transfer from the acetone solution to a Si substrate (n-doped Si with a SiO_2 top layer), and then cleaned with water and propanol. The graphene layers with a thickness less than 9 nm well adhered on the Si substrate and the adherence force between graphene and the substrate was claimed to be van der

Waals and/or capillary forces. Across the years, many research groups have used this economic and facile approach to produce high quality graphene layers in order to use them for the fabrication of nanoelectronic devices. The costless and advantageous of the technique brought scientists to extend this process for fabricating other 2D materials like boron nitride (BN), molybdenum disulfide (MoS_2), and niobium diselenide ($NbSe_2$) (84; 85). However, the mechanical exfoliation process needs improvements for large-scale, defect-free graphene for its use in nanoelectronics.

The first year of my PhD, I focused my attention on the synthesis of graphene by mechanical exfoliation of graphite with the "scotch tape technique". The experimental results will be discussed in the next chapter.

2.4.2. Chemical Exfoliation

Another top down approach for the synthesis of graphene is the chemical exfoliation of graphite that takes place along the normal to graphite basal plane of the original flakes. Generally, the exfoliation of graphite is achieved by the use of different kind of species that can intercalate between the graphite planes. Graphite can accept many species into the space

between graphite layer planes, in particular the species with the ionic radii smaller than the graphite interlayer spacing, can fit easily between the graphite planes to form the graphite intercalation compounds (GICs). The intercalating compounds can be classified in, donor-type intercalation compounds (e.g., K-GIC) where the intercalates donate electrons to the host graphite and acceptor-type intercalation compounds (i.e., H_2SO_4- and $FeCl_3$-GICs) that accept electrons from the host (86). For the production of graphene sheets, usually alkali metals are employed as intercalating compounds. As an example, we can mention the work of Kaner and coworkers (87), which employed the KC_8 as intercalation compound. A highly exothermic reaction between the KC_8 compound and aqueous solution of ethanol causes the exfoliation of graphite:

$$KC_8 + CH_3CH_2OH \rightarrow 8C + KOCH_2CH_3 + \frac{1}{2}H_2$$

According to this equation, potassium ions dissolve into the solution producing the potassium ethoxide along with hydrogen gas evolution that helps in separating the graphitic layers. The filtration of the solution provides the few-layer exfoliated graphene that is then purified by washing it with ethanol.

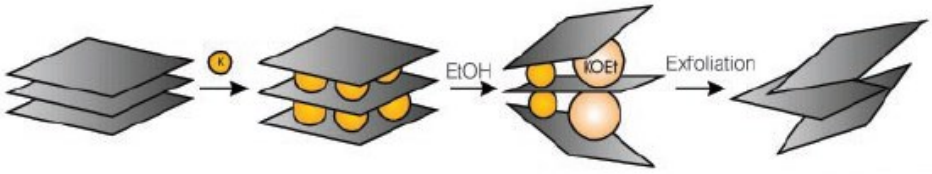

Figure 2-5: Scheme of the chemical exfoliation process [Adapted from ref. (87)]

Another approach for the exfoliation of graphite is the one proposed by Hernandez and coworkers (88). This approach consists in the dispersion and exfoliation of pure graphite by its sonication in organic solvents, in particular in the N-methyl-pyrrolidone (NMP) that provides the best thermodynamic stabilization of the solution (88). This method permits to obtain high-quality, unoxidized monolayer graphene sheets. According to the authors, the exfoliation of graphite (or any other layered material) with the addition of mechanical energy is possible when the surface energy of the solute and solvent are the same. In this case, the energy that is required to exfoliate graphene should be equivalent to the solvent-graphene interaction for the solvents whose surface energies are analogous to that of the suspended graphene (88). Generally, the chemical exfoliation of graphite is a low-cost

and scalable method, and it permits the deposition of the obtained graphene sheets on many substrates.

2.4.3. Laser exfoliation of graphite

The mechanical and chemical exfoliation approaches are based on the detachment of single and/or few layers graphene sheets from the graphite that has a layered structure, where the layers are stacked together by weak van der Waals forces. Every time that these weak forces are broken either with a scotch tape or with the intercalation of certain compounds within the layers, it is possible to obtain mono-atomic graphene layers. Recently an alternative top down approach has been employed for the detachment of graphite, i.e. the laser exfoliation.

One of the first work where it was theorized the potential exfoliation of graphite films using femtosecond laser pulses was reported by Jeschke et al. in 2001 (89). In its work, Jeschke presented a theoretical study, performed by molecular dynamics (MD), of the microscopic processes leading to the femtosecond ablation of graphite. According to the author, due to its layered structure, graphite exhibits two different ablation mechanisms and therefore two different ablation thresholds. In

particular, the mechanism for the low fluence ablation threshold is the exfoliation of graphite, while the high fluence threshold corresponds to bond breaking processes inside the graphite layers and leads to ultrafast melting and expansion of the structure (89). The authors theorized that a fluence of F= 0.35 J/cm^2 was enough to break the bonds of the graphite planes, while a fluence of 0.21 J/cm^2 is below the disruption threshold of the graphite planes and at this fluence the detachment of graphite plane occurs. The snapshots of the dynamics of graphite are reported in the figure below, adapted from ref. (89).

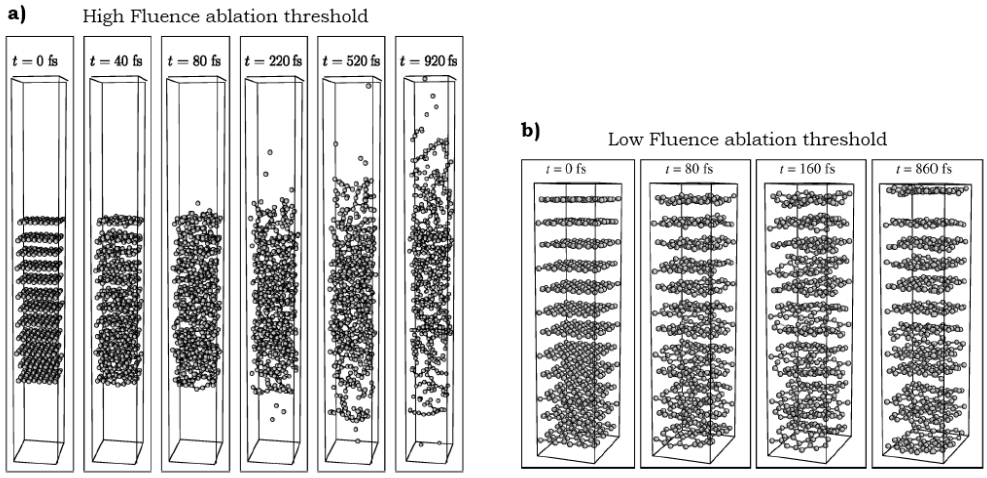

Figure 2-6: Snapshots of the dynamics of graphite for: a) high fluence ablation threshold and b) low fluence ablation threshold. [Adapted from ref. (89)]

The authors reported that the mechanism that leads to the exfoliation of the graphite is due to the laser pulse. Actually, the laser pulse leads to a strong vibrational excitation of the graphite layers, with a movement of the atoms perpendicular to the graphite planes. This excitation reaches a maximum at t=160 fs after the laser pulse maximum and at this time the graphite planes are subjected to a compression, the interlayer distance decreases to ~1.8 Å, and the planes strongly interact and collide. This leads to a momentum transfer and the surface plane that had up to that time zero total momentum starts to leave the crystal in the positive *z* direction. When Jeschke performed this study, graphene had not yet been discovered, but this theoretical study could be considered also as a model for the production of graphene by the use of a femtosecond laser.

In 2008, Carbone and coworkers (90) reported, by means of time-resolved electron crystallography, the observation of the structural dynamics of graphite following an excitation by an ultrashort laser pulse. The time-resolved diffraction data showed that the graphite, after the impulsive laser excitation, first contracts along the c axis on the time scale of 0.5 to 3 ps, whose velocity depends on the excitation fluence, and then the

graphite undergoes a large expansion which leads to the detachment of graphene layers, as reported by Jeschke in 2001.

Another theoretical study for the detachment of graphene layers from a graphite surface with ultrashort laser pulses was reported in 2010 by Miyamoto (91). Qian and coworkers (92) instead reported an experimental work, in the same year. The authors were able to perform the exfoliation of graphite using the laser pulses of a neodymium-doped yttrium aluminum garnet laser (Nd:YAG).

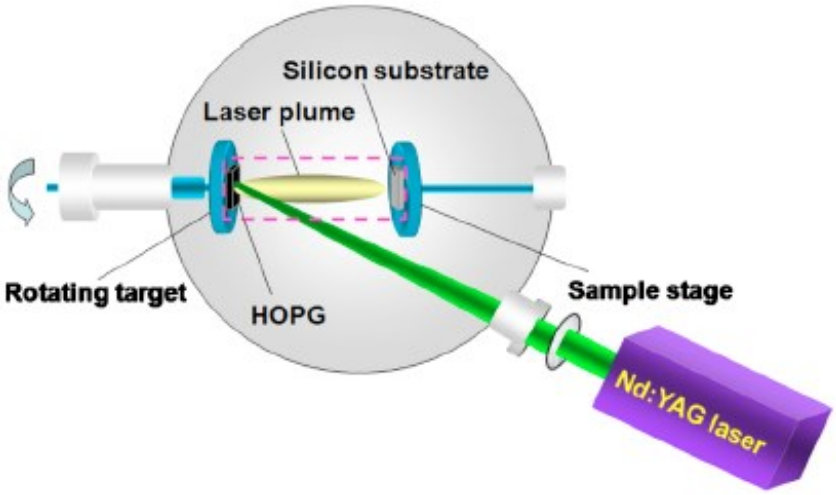

Figure 2-7: Schematic view of the experimental setup. [Taken from ref. (92)]

The authors reported the production of different types of carbon nanostructures by varying the laser fluences, in particular they obtained amorphous carbon, graphene and thin graphite films. The experiments were performed in a chamber filled with argon at a pressure of 1Torr and a target of highly oriented pyrolytic graphite (HOPG) was irradiated at fluences from 0.8 to 20 J/cm^2. The samples obtained at different fluences were characterized by scanning electron microscopy (SEM), transmission electron microscopy (TEM) and Raman spectroscopy. The analysis showed that the graphene sheets are obtained after the irradiation of HOPG from 1 to 10 J/cm^2, while amorphous carbon and thin graphite films are produced at 0.8 and 20 J/cm^2, respectively.

Recently, my research group and me, we reported a novel approach for a large-scale and green synthesis of graphene sheets by the pulsed laser ablation in water of HOPG (93).

The application of laser irradiation to ablate materials from a target was firstly reported in early 1960s when the ruby lasers became available. Soon after, pulsed laser ablation (PLA) of solid materials has been developed.

The PLA has attracted intensive attention, because of its great potential in laser-based material processing including thin

solid film preparation, nanocrystals growth, surface cleaning, and microelectronic device fabrication. Usually, the PLA synthesis of nanomaterials can be performed in two distinct environments: in a vacuum, or gaseous, environment or in a liquid medium. For the former, PLA is usually combined with a tube furnace or vacuum chamber, as shown in Figure 2-8a). In 1993, the laser ablation was firstly achieved in liquid media (pulsed laser ablation in liquid (PLAL) Figure 2-8b), to fabricate a colloidal solution of nanoparticles.

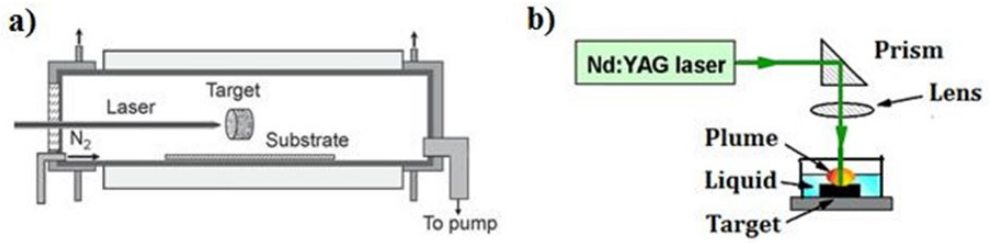

Figure 2-8: Schematic for pulsed laser ablation in a) vacuum environment and b) in liquid medium

In 1993, Cotton applied a pulsed laser to ablate pure metal targets in various solvents to form colloidal solutions containing metal NPs (94). Since then, PLAL became a general approach that permits to obtain a large variety of nanomaterials in the colloidal state, such as metallic particles,

metal oxides, semiconductors, and carbon-related materials depending on the nature of the target ablated (95), (96), (97). PLAL is somewhat different from the other laser ablation approaches that operate in vacuum or gaseous environments because the liquid medium not only provides some effective controlling parameters for fabrication, but also greatly affects the morphology and microstructure of the products. Moreover, it has been observed that the size and shape of the nanoparticles can be modified by laser post irradiation. The ablation of a target material upon laser irradiation is a very complex process. The incident laser pulse penetrates into the surface of the material within a certain penetration depth. This dimension is dependent on the laser wavelength and on the refraction index of the target material and is typically in the range of 10 nm. The strong electrical field generated by the laser light is sufficient to remove electrons from the bulk of the penetrated volume, within 10 picoseconds, for a nanosecond laser pulse. The free electrons oscillate within the electromagnetic field and can collide with the atoms of the bulk material, thus transferring some energy to the lattice. The irradiated surface is then heated up and vaporized. At a high enough laser flux, the material is typically converted to a

plasma which contains various energetic species including atoms, molecules, electrons, ions, clusters, and particulates, and therefore possesses some unique characteristics such as high temperature, high pressure, and high density. Subsequently, the large pressure difference between the laser produced initial seed plasma and ambient atmosphere causes a rapid expansion of the plasma plume and then it cools down. Under suitable condensation conditions (temperature and pressure), the plasma species will nucleate and grow into desirable nanostructures, either on a substrate or in a cool liquid medium.

Therefore, laser ablation of a solid target in a confining liquid has been demonstrated to be an effective and general route to synthesize nanocrystals and nanostructures. Notably, three advantages of laser ablation in liquids over other techniques for the nanocrystals synthesis are: 1) “simple and clean” chemical synthesis, due to the process with reduced byproducts formation, simpler starting materials, catalyst-free, etc. 2) variety of metastable phases that may not be attainable by the same mild preparation methods. 3) Possibility of synthesis of nanocrystals and new nanostructures, with the

purpose of fundamental research and study of their potential applications.

2.4.4. Chemical synthesis: Graphene from reduction of Graphene Oxide

The chemical synthesis of graphene from the reduction of graphene oxide (GO) is a top-down approach that has been used from 2006. The first researcher that demonstrated the existence of monolayer flakes of reduced graphite oxide was Boehm in 1961 (*Z. Naturforschg.* 17 b, 150). This method consists in the synthesis of graphite oxide (GO) that is then dispersed by sonication in a solution and finally it is reduced to graphene with appropriate reducing agents. Three methods can be employed to perform the oxidation of graphite, which are the Brodie method (1860), the Staudenmaier (1898), and the Hummers one (1958). In all these three methods, the oxidation of graphite is achieved by the use of strong acids and oxidants. However, the most employed method is the Hummers one because it is safer and less hazardous than the other two. According to this technique, when graphite is mixed with sodium nitrite, sulfuric acid, and potassium permanganate (98), it is oxidized and the interlayer spacing

increase from 3.34 Å up to 5.62 Å or 7 Å depending on the duration of the oxidative reaction (1h and 24h respectively). When the graphite is dispersed in polar liquids, the molecules insert between the layers and this further expands the graphite structure leading to the detachment of single layers from the GO bulk. The sonication of the solution helps this process. Finally, in order to reduce the GO layers to graphene layers, the solution is treated with hydrazine hydrate (99). In the figure below is presented a scheme showing the steps of the chemical synthesis of graphene sheets.

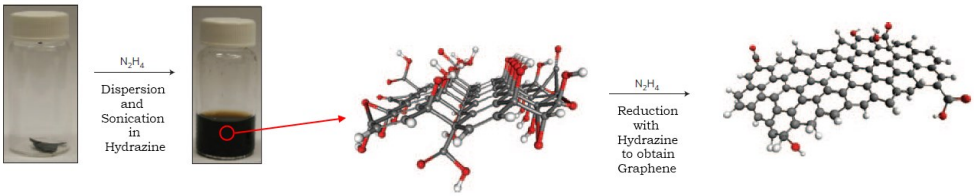

Figure 2-9: schematic showing the chemical synthesis of graphene from the reduction of GO. [Adapted from ref. (99)]

In 2009, Cote and coworkers employed the Langmuir-Blodgett assembly technique to deposit GO single layers on different types of substrates (100), and this technique can be extended to the deposition of the reduced graphene layers on any type of substrates. This possibility and the low temperature process are some of the advantages of the chemical synthesis of

graphene. Unfortunately, the chemical process shows many disadvantages such as the fact that the process involves many steps and the use of hazardous explosive chemicals such hydrazine; it does not provide large-scale production of graphene sheets, and the graphene obtained presents some defects. Furthermore, the reduction of GO is not always complete and this may affect the electronic properties of the graphene sheets. In conclusion, the chemical way does not provide better quality of graphene sheets than the other methods, and this technique needs further improvements.

2.5. Characterization techniques of graphene

Most of the synthetic methods illustrated in the previous paragraphs provide not only samples consisting of single layer graphene, but bi-layer and few-layers graphene are also produced. Therefore, it becomes necessary to have techniques that allow the analysis and characterization of the obtained graphene samples, in terms of determination of the number of layers and the purity of sample (absence or presence of defects). Actually, the characterization of graphene plays an important role in the field of graphene research and generally,

it involves measurements based on both microscopic and spectroscopic techniques.

2.5.1. Optical Microscope

An efficient tool for the identification of graphene sheets relies on the optical microscopy, which gives a wide field of view. After the discovery of graphene, this technique was primarily used to image various layers since it is a cheap and non-destructive technique. The identification of graphene sheets, down to one layer in thickness, with the optical microscopy is possible due the different optical contrast between the graphene layers and the substrates on which the layers are deposited. This method is based on the contrast arising from the interference of the reflected light beams at the air-to-graphene, graphene-to-dielectric, and (in the case of thin dielectric films) dielectric-to-substrate interfaces (101). The optical microscopy imaging permits to distinguish a single layer graphene sheet (SLG) from bi-layer and few layers graphene from the different contrast, but in order to have a good identification of the layers, this technique requires graphene layers to be deposited on silicon wafer with a certain thickness of silicon dioxide (~300 nm in thickness). Single, bi,

and multi-layers graphene (<10 layers) on Si substrate with a 300 nm SiO_2 are differentiated using contrast spectra, generated from the reflection light of a white-light source (102). SiO_2 is the most commonly overlay materials on silicon for enhancing the contrast of graphene layers (103).

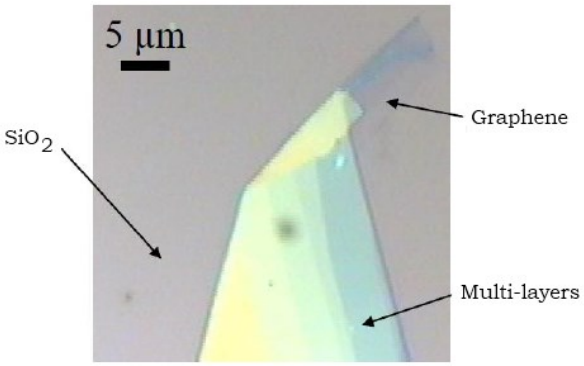

Figure 2-10: Optical image of SLG and multi-layer graphene

Blake et al. (103) demonstrated that one governing factor that modulates the contrast is the wavelength of the incident light. They found that under normal white light illumination, sheets were invisible on 200 nm SiO_2, while thick and thin sheets were visible on 300 nm SiO_2 when green light was used, whereas sheets were visible on 200 nm SiO_2 by blue light. The Figure 2-10 shows the optical image of the different layers of the micromechanically exfoliated graphene on silicon substrate with 300 nm SiO_2 over-layer. As illustrated above, the

detection technique demonstrated is dependent on the substrate thickness and incident light wavelength. More research is needed to facilitate graphene-based sheets visualization independent of support material without any modification of the graphene.

2.5.2. Scanning Electron Microscopy (SEM) and Transmission Electron Microscopy (TEM)

The scanning electron microscopy (SEM) is a characterization technique employed for the observation of graphene.

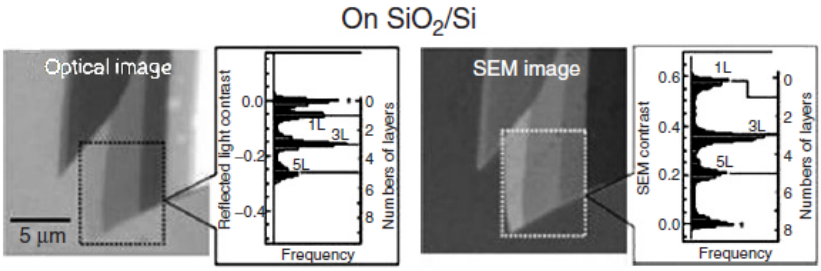

Figure 2-11: Determination of number of layers by optical microscopy and SEM for graphene on SiO2/Si [adapted from ref. (104)].

This method is similar to optical microscope and it is another way to determine the number of layers. Hiura et al. in 2010 (104) demonstrated that the secondary electron intensity from

the sample operating at low electron acceleration voltage has a linear relationship with the number of graphene layers as shown in the figure. In general, TEM is frequently used to image nano-size materials to the atomic scale resolution where a transmitted electron beam passes through the ultra-thin sample and reaches to the imaging lenses and detector.

As graphene is an atom thick layer, it seems that the TEM can resolve atomic features of the graphene. However, the use of traditional TEMs is limited by their resolution at low operating voltage, whereas the operation at high voltage damages the monolayer.

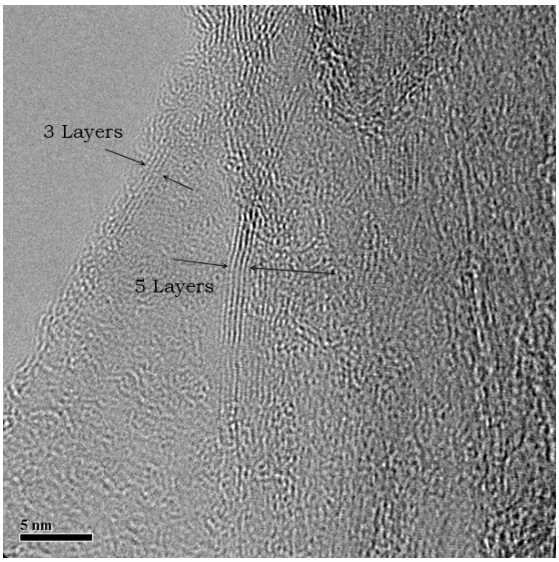

Figure 2-12: TEM image of graphene layers

TEM can not only observe the morphological feature of graphene but also count the number of graphene layers accurately. It is known that the edges of the graphene films always fold back, allowing a cross sectional view of the films. These edges can be observed by TEM leading to an accurate calculation of the number of layers at multiple locations on the films. Moreover, TEM is often supported with the electron diffraction pattern, which shows a hexagonal pattern of the graphene crystal structure.

2.5.3. Atomic Force Microscopy (AFM)

The Atomic Force Microscopy (AFM) is another characterization technique that permits to determine the number of the layers in a graphene sample. Based on the interlayer distance in graphite of 3.5 Å, the thickness of a graphene flake or the number of layers is determined; in fact, from the step of graphene on substrate, it is possible to estimate the number of graphene layer. The method is relatively slow, but the 3.5 Å step height for each successive layer is well within the detection limits for the atomic force microscopes.

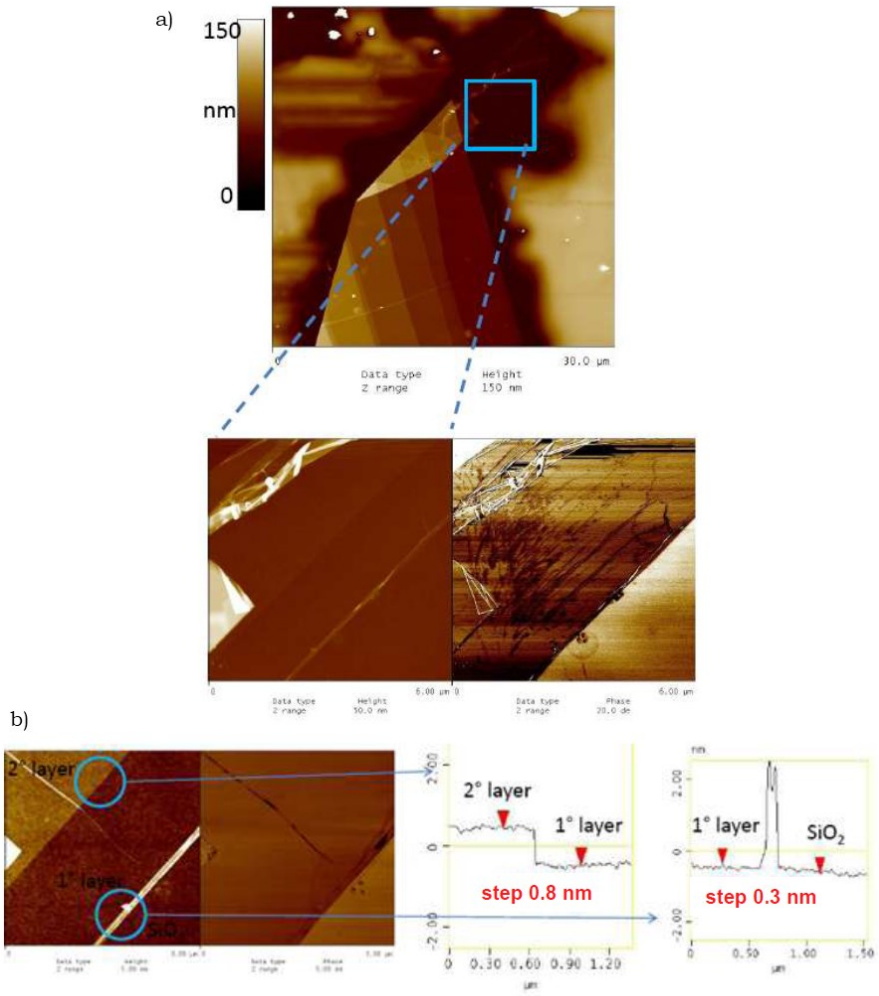

Figure 2-13: a) AFM image of graphene layers, b) determination of the number of graphene layers.

However, experimentally sometimes it is hard to get the theoretical thickness of 0.35 nm, due to the differences in tip

attraction/repulsion between the insulating substrate and semimetallic graphene. Therefore, the AFM method for measurement of the graphene layer number is not accurate, and it has a very low throughput (105).

2.5.4. Raman Spectroscopy

Generally, Raman spectroscopy is a powerful tool for the characterization of carbon based materials. From the analysis of the main features in the Raman spectra in terms of position, width, intensity and shape of the bands is possible to distinguish and characterize the various carbon allotropes. In graphene research, Raman spectroscopy is employed for the identification of the number of layers, and to detect the presence of defects and it has been used as a probe to investigate the mechanical, electrical, and optical properties of graphene. The Raman analysis, compared with the previous techniques, is a quick, nondestructive and effective way for the structure and quality characterization of graphene layers.
The major Raman features of graphene are the G band (~ 1580 cm^{-1}) and 2D band (~ 2700 cm^{-1}).

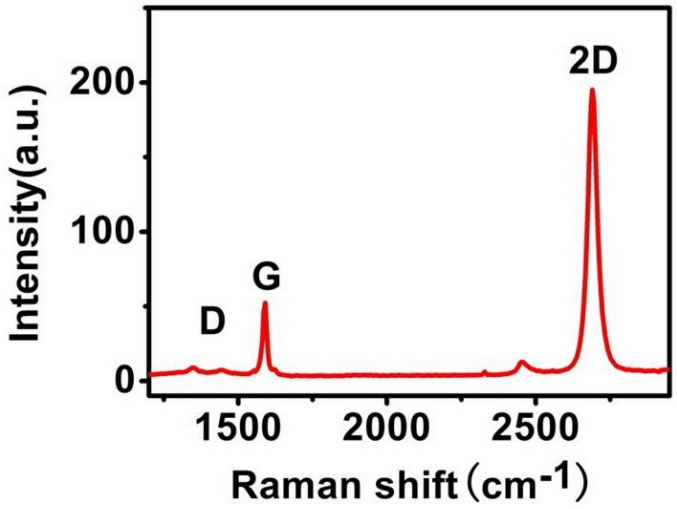

Figure 2-14: Raman spectrum of graphene [taken from the web]

In the case of a disordered sample or at the edge of a graphene sample, the so-called disorder-induced D-band can be detected, and it lays at about half of the frequency of the 2D band (around 1350 cm-1). Moreover, another weak disorder-induced feature the D′-band appears at ~1620 cm^{-1}. A typical Raman spectrum of graphene is shown in Figure 2-14. As mentioned before, from the analysis of the Raman bands of graphene is possible to obtain information about the number of layers of a sample and to determine the quality of the layers in terms of absence of defects. In particular, from the shape and intensity of the 2D band is possible to distinguish between

single layer, bi-layer and few-layers graphene. Ferrari el al. (106) have shown that the 2D band splits into two components for bulk graphite and in four components for bi-layer graphene, as shown in Figure 2-15(b). An increase in the number of layers reduces the relative intensity of 2D band and increases its FWHM, while the monolayer shows a single sharp 2D peak and it is four times more intense than the G peak. When the D band does not appear in the Raman spectrum of graphene, as shown in Figure 2-15(a), this confirms the absence of defects in the layer.

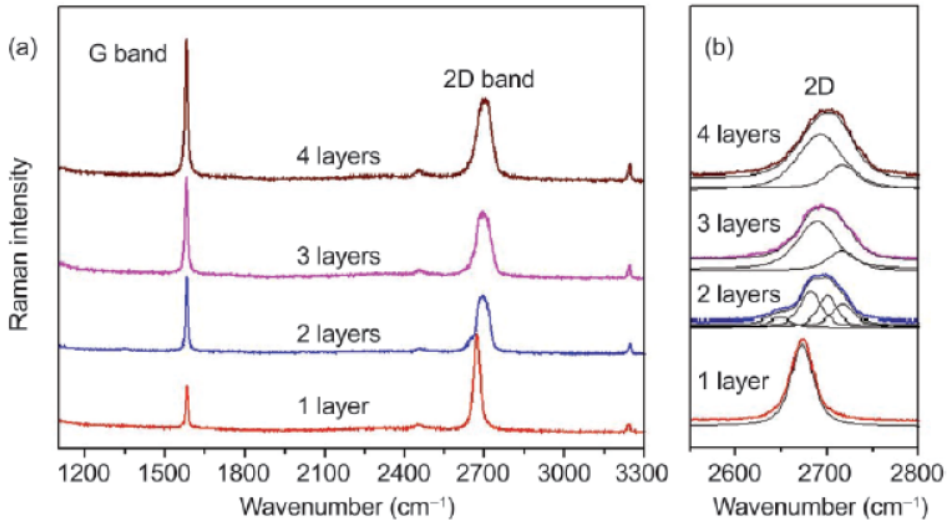

Figure 2-15: a) Raman spectra of single-, bi-, and few-layers graphene. b) evolution of the spectra (at 514 nm) with the number of layers.

2.6. Experimental results: mechanical and laser exfoliation

2.6.1. Mechanical exfoliation

The first year of my PhD course, I performed the synthesis of graphene employing the mechanical exfoliation technique. The method employed is schematically shown in Figure 2-16.

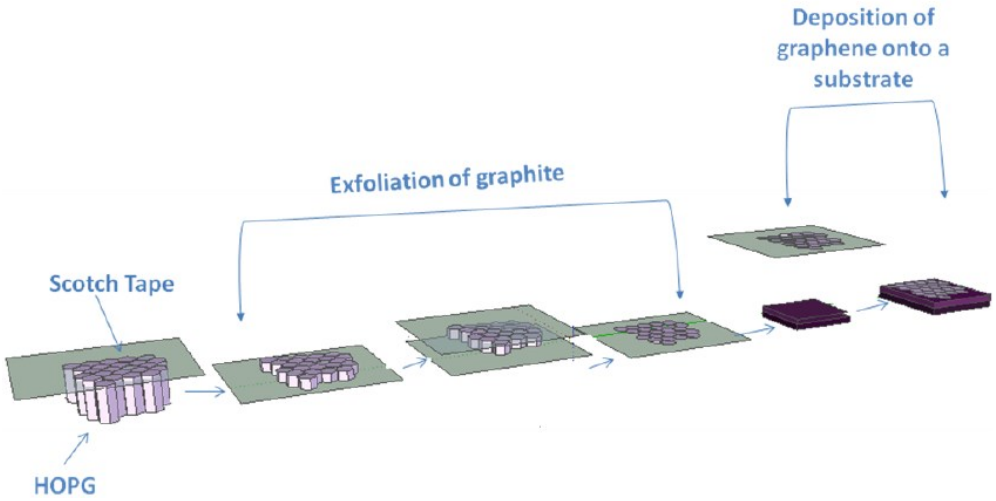

Figure 2-16: Scheme of the mechanical exfoliation process

A target of HOPG was peeled off many times with a scotch tape until some layers remained attached to the tape. Then, another piece of tape was used to further exfoliate the layers

and the resulting tape with few-layers of graphene attached on it, was deposited onto a substrate of Si with 285 nm of SiO_2. After the removal of the tape, single layers and few-layers of graphene were transferred from the tape onto the substrate. To provide identification of single layers, the samples were investigated with an optical microscope and then by AFM. After the identification, Raman spectroscopy was performed in order to confirm the production of graphene sheets. For the individuation of graphene, we employed an optical microscope with a 100x objective, while AFM analysis was carried out in air using a commercial instrument (Multimode Nanoscope IIIa, Digital Instruments, Santa Barbara, California) equipped with a phase extender apparatus and a Q-box module (107). Raman scattering has been excited by 514.5 nm radiation coming from an Ar ion laser. The incident laser beam was focused by a 100x objective and the laser power on the samples was kept to a minimum to avoid heating. In Figure 2-17(a) is shown an optical image of a graphene layer experimentally obtained and it is possible to distinguish a single, bi- and multi-layers graphene domain. The single layer has been highlighted with a blue square, and on it, it was performed the AFM (Figure 2-17(b)) and Raman (Figure 2-17(e)) analysis. Both the

characterization techniques confirmed that the analysed layer was a single sheet of graphene showing a step of ~ 0.3 nm between the layer and substrate, since the interlayer distance in graphite is 0.34 nm. Moreover, the Raman spectrum displayed the G band appearing at 1582 cm^{-1} and the 2D band at 2700 cm^{-1}, as the Raman spectrum of graphene reported in literature (106; 108) and described in the previous chapter.

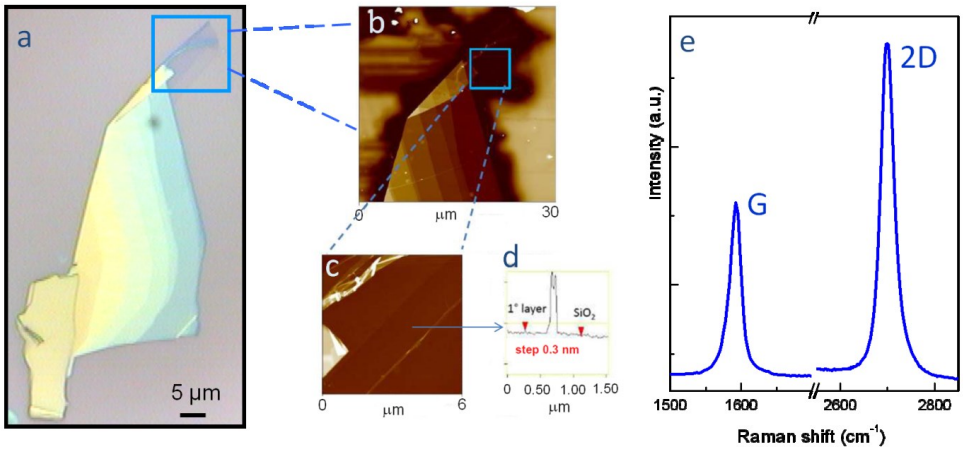

Figure 2-17: a) optical and b) AFM images of the graphene layer obtained experimentally. c) magnification of the topographic image shown in (b). d) Section of the layer showing the layer thickness. e) Raman spectrum of the layer.

During the Raman characterization, we found that some graphene samples showed different spectra from the one reported in Figure 2-17(e). In Figure 2-18 are reported the

Raman spectra of two layers, which are representative of a very common situation randomly observed in our production method.

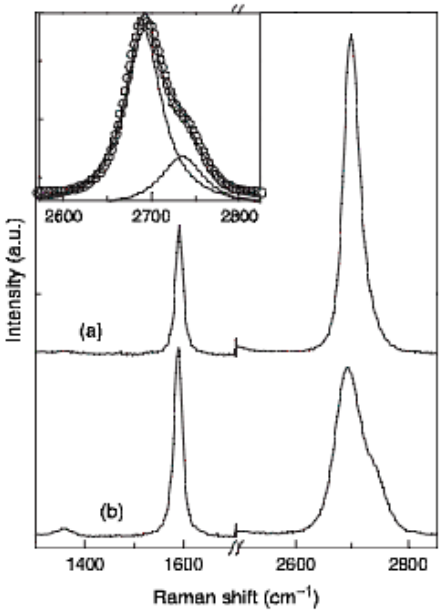

Figure 2-18: Raman spectra for two typical single layer of graphene obtained after mechanical exfoliation and deposition onto a SiO2/Si substrate. The inset shows a deconvolution of the 2D band relative to spectrum (b).

If we compare the spectra (a) and (b), we can detect some differences. In particular, spectrum (a) exhibits the characteristic features of single layer graphene, while spectrum (b) shows an asymmetric and broader 2D band and a different 2D/G intensity ratio. The 2D band in spectrum (b)

can be fitted with two distinct peaks (see inset in Figure 2-18), which we denote by 2D− (at 2691 cm−1) and 2D+ (at 2734 cm−1) according to a notation reported in literature (109). In order to obtain indication on the morphology and structural parameters of the two layers, AFM analysis was performed and the results are shown in Figure 2-19. In the figure the topographic (a), (d) and the phase lag (b), (e) images are showed together with the section analysis (c), (f). This revealed that both the analysed sheets consist of a single layer graphene with a step height of about 0.4 nm in agreement with literature data (110).

It can be noticed that, the morphology of the two layers is markedly different as revealed by the topographic images. In particular, while the layer in Figure 2-19(a) (related to spectrum (a) in Figure 2-18) appears as a flat surface, the one in Figure 2-19(d) (related to spectrum (b) in Figure 2-18) seems to have corrugation lines, which appears as creases in a tissue. These lines can be responsible for an induced stress in the layer and should be the cause of the already discussed differences between the two Raman spectra.

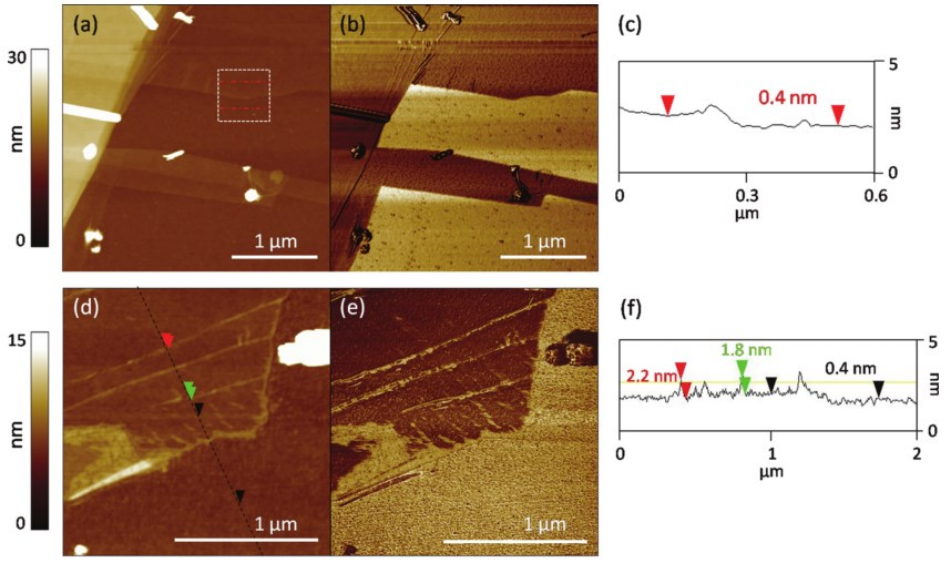

Figure 2-19: Topographic (a), (d) and phase (b), (e) images relative to the flakes analyzed by Raman spectroscopy and reported in Figure 2-18. Sections are also shown in (c) and (f), showing the layer thicknesses and the height of the observed creases (bright contrast in the phase and topographic images).

Some research groups have reported Raman studies of the 2D mode of single layer graphene under uniaxial strain, observing an induced modification of the 2D band (109; 111). The application of uniaxial strain induced after the deposition of the graphene onto a flexible PDMS (polydimethylsiloxane) substrate has shown a 2D band shift toward lower frequencies with a remarkable response. Moreover, it was observed an asymmetric peak broadening, and a clear splitting in two distinct peaks 2D- and 2D+. This splitting increases with

increasing the strain value. It was also found that the intensity ratio of the two components 2D+ and 2D- depends on the angle between the direction of the applied strain (ε) and the polarization of the incident light (P) during Raman measurements. In particular, the studies showed that when the incident light polarization is parallel to the direction of strain, the 2D- is dominant, while the 2D+ is dominant in the perpendicular case.

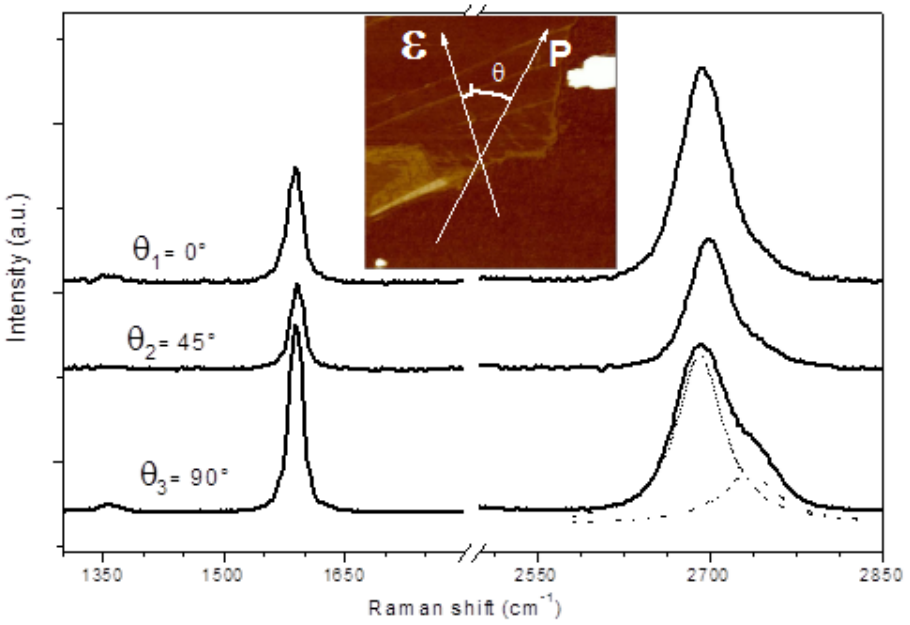

Figure 2-20: Evolution of the 2D modes for the corrugated single layer graphene as a function of the angle (θ) between the strain direction (ε) and the polarization of the incident light (P).

Following these findings and assuming the folds as a kind of deformation, we collected different Raman spectra varying the angle between the orientations of the strain (ε) and the orientation of the polarization of the incident light (P). In such a case, we assume that the strain direction is perpendicular to the folds. Some of the Raman spectra obtained are shown in Figure 2-20; in this case, θ is the angle between the polarization of the incident light and the direction orthogonal to the observed folds in sample (b) (see inset in Figure 2-20). As expected, the intensity ratio of the two peaks (2D- and 2D+) varies with the angle between P and ε. In particular it is remarkable that the 2D+ peak intensity at P // ε is smaller than the intensity when P $\perp$ ε (2D-), in agreement with ref. (109). From these observations, it is possible to assess that the "Scotch tape" deposition method can induce, accidentally and randomly, deformations on the deposited single layer graphene, which can be easily observed by AFM. These corrugations results in a strain that can be measured using Raman spectroscopy. In particular, the entity of such a strain, as aforementioned, leads to a separation of the 2D in the two components 2D+ - 2D-. The trend is shown in Figure 2-21.

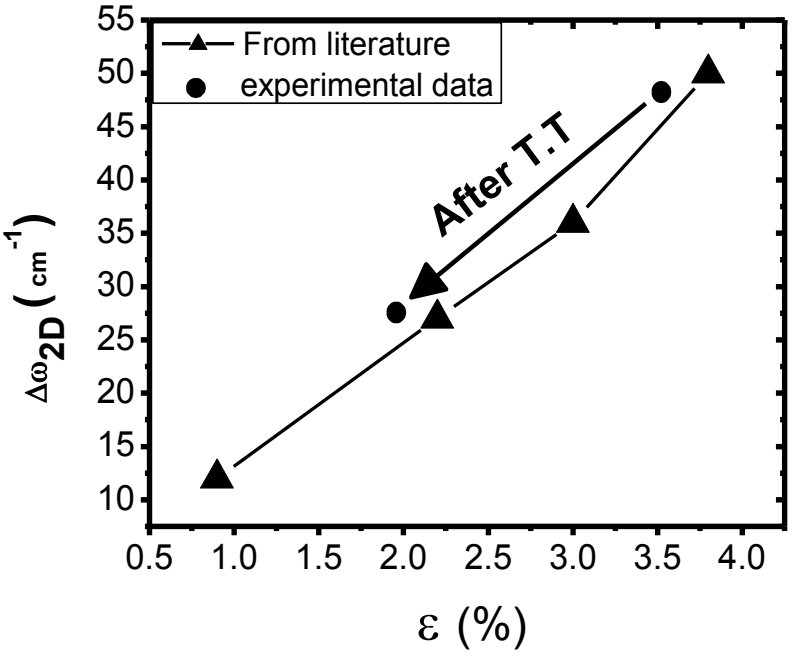

Figure 2-21: Change in the $2D^{-}$–$2D^{+}$ distance as a function of the strain as reported in ref. (109). The figure also reports the splitting value for the corrugated sample, before and after a thermal treatment at 300°C in vacuum.

Early results have shown that thermal annealing at 300°C consistently reduce the strain value as reported in the same Figure 2-21. Further measures are underway to clarify the role of temperature in releasing the strain. These data have been already published ref. (112).

2.6.2. Laser exfoliation of graphite

The laser exfoliation of graphite for the synthesis of graphene sheets was performed by laser ablation of a graphite target in water. In Figure 2-22 is shown the scheme of the laser exfoliation of HOPG.

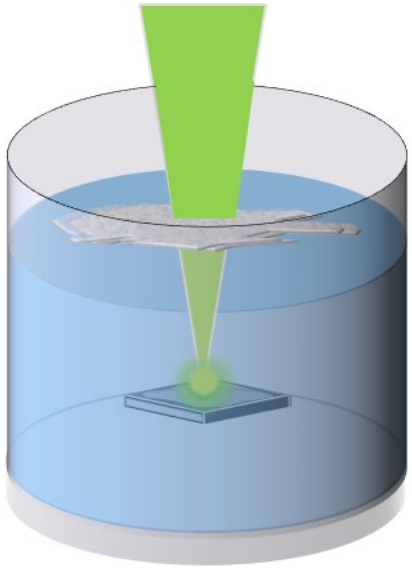

Figure 2-22: Scheme of the laser exfoliation of graphite with a nanosecond laser

The target was placed at the bottom of a vessel, covered with two centimeters of Millipore grade deionized water and then irradiated using the second harmonic (532 nm, 5 ns pulse,

and 10 Hz repetition rate) of a Nd:YAG laser. The synthesis was performed employing different fluences.

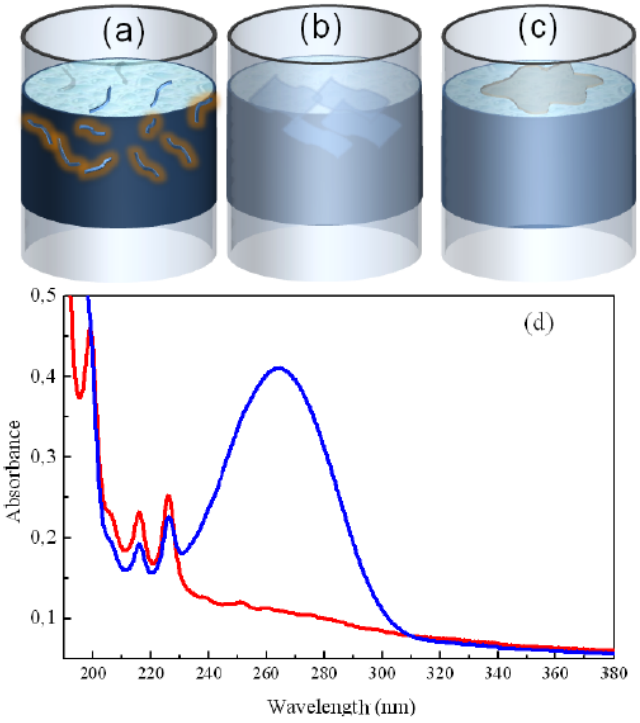

Figure 2-23: Schematic representation of the observed three ((a)–(c)) phases during and after the irradiation of graphite in water. (d) Absorbance spectra for low (red) and high (blue) fluence irradiation.

During our experiments, we noticed the existence of at least three stages of laser–matter irradiation induced effects, which are probably in competition for wide fluence intervals. At low fluences (below 5 J cm^{-2}) water remains limpid after the

irradiation, even though the ablation threshold has been overcome. Spectroscopic characterizations reveal that the ablation process produced specific molecular species whose distinct sharp features are observed between 190 and 300 nm, as shown in Figure 2-23(d) the red spectrum. These signals belong to hydrogen-terminated polyynes with relatively short length (113) (up to ten carbon atoms, Figure 2-23(a)). In a second stage, at fluences between 5 and 10 J cm^{-2}, the water solution is still quite limpid but the UV spectrum showed the formation of other species whose wide and intense absorption signal is observed around 260 nm and the relative spectrum is displayed in Figure 2-23(d) the blue spectrum. Noteworthy, this signal is superimposed on those coming from the linear carbon chains (polyynes) and that the production of the new band seems to be in competition with that of the formation of polyynes. As for the nature of the 260 nm absorption, we supposed it is related to the presence of sp^2 clusters of very small dimensions. In particular, we hypothesized that it can be attributed to the presence of GQDs (114) or graphene nano-sheets (115) as it arises from the excitation of a π- π resonance in the graphitic structure (116). A third stage has been revealed at fluences higher than 10 J cm^{-2}. At these values, the

turbidity of the liquid slightly increased and some fluctuating objects appeared. In particular, a layered material appeared randomly floating at the water–air interface at the end of the ablation, as displayed in Figure 2-23(c). The sheet has been collected from the water surface through a solid substrate and several investigations have been conducted either in the liquid phase or on the detached layer. Some optical images of a layer deposited on different substrates are reported in Figure 2-24.

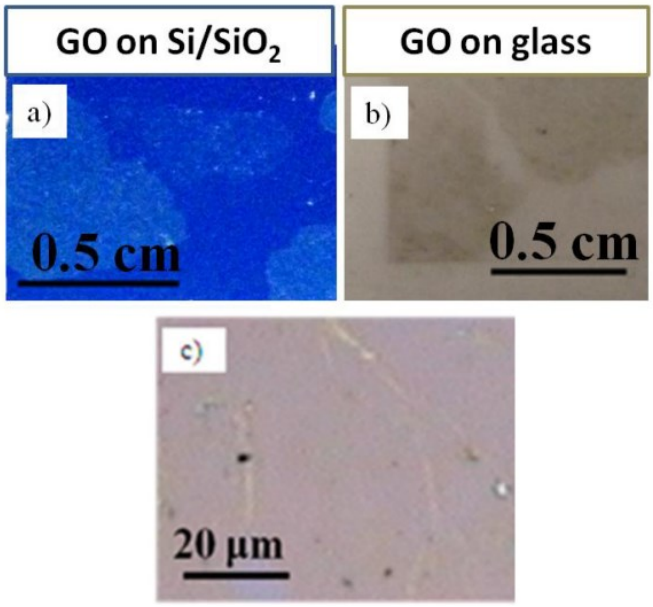

Figure 2-24: Detached layers deposited onto: a) Si/SiO2 substrate and b) glass substrate. In c) it is reported an optical image of the layer where some ripples can be observed on it.

The AFM and SEM results are reported in Figure 2-25. The layer is several tens of microns wide, has a corrugated surface (probably due to the rough collection) and a thickness of less than 1.6 nm, as found by measuring the layer–substrate step through AFM in the region where the sheet seems to adhere better. Each deposit is made of one or two layers, which have been detached from the graphite surface and partially oxidized because of the presence of reactive species in the surroundings during or immediately after the detachment.

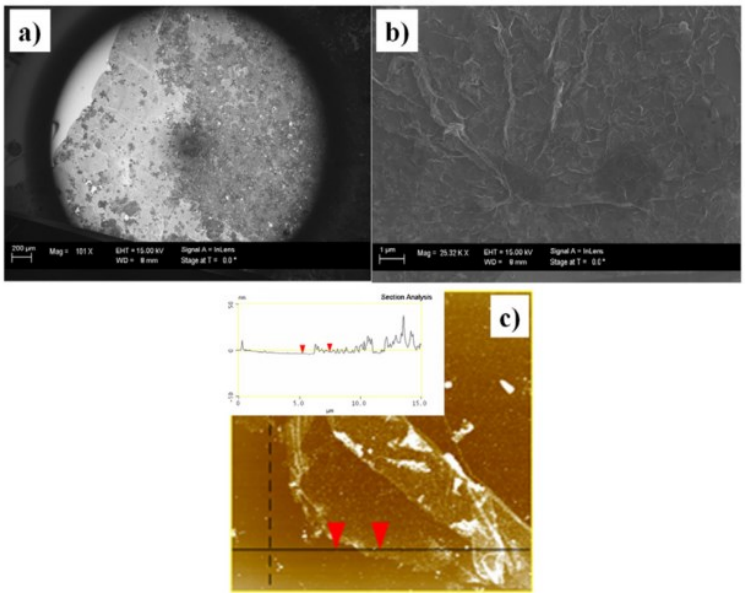

Figure 2-25: Low-magnification (a) and high-magnification (b) SEM images of layers detached from graphite upon laser irradiation and deposited onto a solid substrate. The figure also shows an AFM image (c) with a section analysis. Here a 1.6 nm step was observed.

The presence of some oxygen group was confirmed by XPS analysis reported in Figure 2-26. The compares the C 1s signal coming from a detached layer with that obtained for GO by using the Hummers method (117). Deconvolutions have been performed following the indications present in the literature (118) and reveal that the amount of oxygenated carbon species is below a few per cent in the laser-generated graphene, which could be labelled as reduced graphene oxide (rGO).

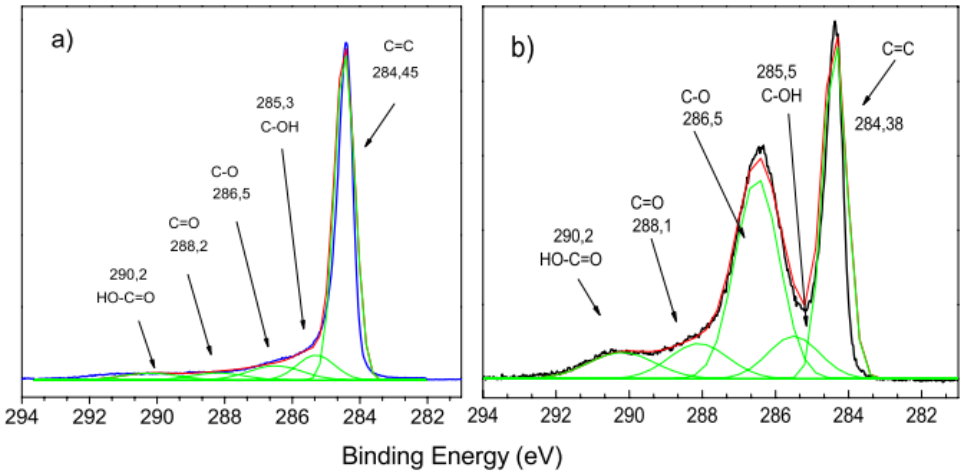

Figure 2-26: XPS analysis (C 1s) of the layer detached (a) compared with graphite oxide obtained by using the Hummers method (b). Deconvolutions and assignation have been done following ref. (118)

The moderate oxidation is also confirmed by Raman spectroscopy, as shown in Figure 2-27. Raman spectroscopy is

capable of detecting sp^2 domains isolated by the hydroxyl, carboxyl and carbonyl groups. These domains are generally difficult to detect by microscopic techniques.

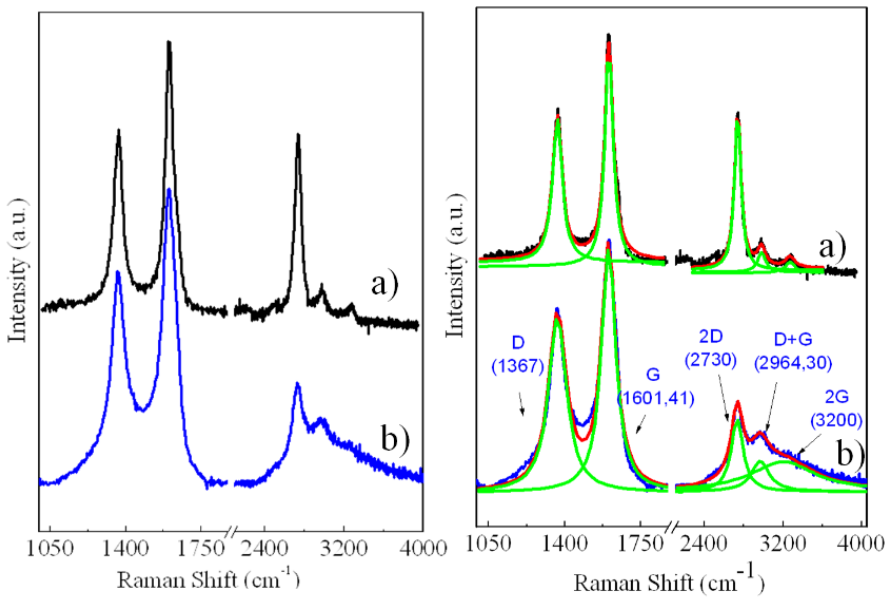

Figure 2-27: Left side: Raman spectra of the dried solution (a) and the layer collected from the air–water interface (b). Right side: Deconvolutions of the Raman spectra.

The two spectra presented in Figure 2-27(a) on the left refer to the material which remains in suspension (once the liquid has been removed by a drying process, and to the layer collected at the water–air interface (Figure 2-27(b)). It is possible to identify a G band at 1600 cm^{-1} and a defect-induced mode (D band) at

1367 cm^{-1}. Moreover, the so called 2D band at 2730 cm^{-1}, the combinational modes D^+ + G at 2964 cm^{-1} and the 2G signal at 3200 cm^{-1} can be detected as shown from the deconvolutions displayed in Figure 2-27 on the right. This work has been already published (93) and we demonstrated that exfoliation of graphite in water can be achieved using laser irradiation without the use of any reactant. The exfoliation produced highly reduced graphene oxide products, which form a freestanding membrane at the water–air interface. The repeatable process of the membrane formation indicates a scalable approach for rGO, which will provide high-quality macroscopic samples for the exploration of novel properties and the development of new applications.

2.6.3. Mechanical versus laser exfoliation

In the previous paragraphs, the mechanical and laser exfoliation of graphite have been presented. Generally, both techniques provide high quality graphene sheets made of one up to six layers. The laser exfoliation permits to obtain larger graphene domain than the mechanical exfoliation. Moreover, the graphene sheets are dispersed in the liquid and it can be centrifuged, drop casted onto a suitable substrate depending

on the next use of the samples, or the solution can be employed for the fabrication of other graphene-based nanomaterials. Both techniques are cheap, environmental friendly, since no by products are produced, and any dangerous reactants are employed. In particular, in the case of laser exfoliation the only reactants are water and graphite, while for mechanical exfoliation a scotch tape and graphite are employed. One of the disadvantages of the mechanical exfoliation is the lack of scalability, which on the contrary, can be achieved by laser exfoliation.

Chapter 3. Graphene-based Nanomaterials

3.1. Bottom-up and Top-down Approaches

Since the discovery of graphene, many efforts have been made in order to improve its properties for its use in various fields. For most of applications, it is required a modification of the structure of graphene that lead to the creation of new "graphene-based" nanomaterials. With this term researchers usually refers to a wide range of materials such as graphene nanowalls, porous graphene, graphene quantum dots, and composite materials made of graphene and different nanoparticles. These materials are usually obtained employing either bottom up or top down approaches. Generally, the basis of bottom-up approaches is the employment of atomic or molecular precursors (methane, hydrogen, polyynes) as building blocks materials for the construction of new nanostructures, while top-down methods consist of size reduction of larger structures such as graphite or graphite oxide. The second year of my PhD, as mentioned in the

introduction, my research group and me, we performed the synthesis of graphene nanowalls (GNWs) through a bottom up approach. In particular, we employed a solution of polyynes (see Chapter 1, paragraph 1.5) dispersed in water as molecular precursors for the fabrication of GNWs. The bottom up approach we developed represents a novel method for the synthesis of these nanostructures, which are usually synthesized with different techniques. Regarding the synthesis of graphene-based nanomaterials employing top down approaches, the third year of my PhD course, we successfully synthesized porous graphene (PG) and graphene quantum dots (GQDs). In particular, we develop a novel top-down approach in which a target of graphite was ablated with a femtosecond laser leading to a mass production of PG and GQDs. In the next paragraphs, GNWs, PG and GQDs will be introduced together with a brief description of the synthetic ways generally employed for the synthesis of each of these graphene-based nanomaterials. The novel methods we developed (bottom-up and top-down approaches) and the results obtained will be discussed as well.

3.2. Graphene Nanowalls (GNWs)

Generally, the term "graphene nanowalls" refers to a two-dimensional carbon nanostructures constituted of many graphene layers that are stacked, almost vertically, onto a substrate. A scheme of the structure of GNWs is displayed in Figure 3-1. It can be observed that, the arrangement of the layers forms a wall structure with a high aspect ratio with thickness of about 10 nanometers.

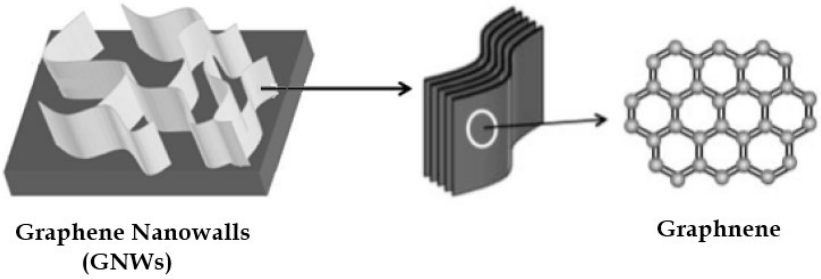

Figure 3-1: Schematic view of the structure of the graphene nanowalls.

Ando *et al.* (28) accidentally produced GNWs during an experiment for the fabrication of carbon nanotubes, in 1997. They were for the first time described as "petal-like sheets" that "form a sponge-like grain that appears flower-like" (28). The second report of the synthesis of the carbon nanowalls dates to 2002 by Wu (29), and they were again produced

accidentally. From the time when they were unintentional synthesized, GNWs, due to their high inertness, large surface area and the unique structure, appeared to be promising materials for many applications. In particular, the sharp edges and vertical orientation make GNWs potential field emission emitters (35), (36), (119), (120). Moreover, their high surface area could be ideal for catalyst support (121). For that reason, many efforts have been carried out in order to obtain reproducible methods for their production in order to exploit their outstanding properties.

3.3. Bottom-up approaches for GNWs production

The most common methods for the synthesis of GNWs are based on plasma-enhanced chemical vapor deposition technique. During the last decade, different types of methods have been developed and they are listed below.

- Microwave plasma-enhanced chemical vapor deposition (MWPECVD).
- Radio-frequency plasma-enhanced chemical vapor deposition (RFPECVD), (RF inductively coupled

plasma (ICP) and RF capacitively coupled plasma (CCP)).

- Hot filament chemical vapor deposition (HFCVD).
- Electron beam excited plasma-enhanced chemical vapor deposition (EBEPECVD).

Wu et al. using MWPECVD (29) accidentally produced Graphene nanowalls during the growth of carbon nanotubes.

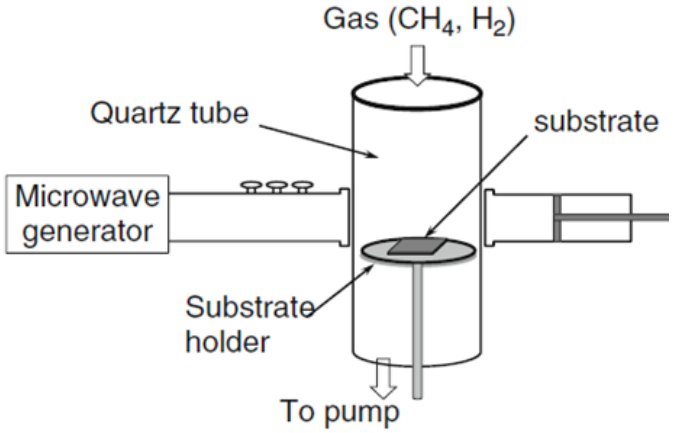

Figure 3-2: Schematic of a microwave plasma-enhanced chemical vapor deposition (122).

In the experiment, a NiFe-catalyzed substrate (Si, SiO_2/Si, sapphire) was preheated to about 650–700°C in hydrogen plasma, and a mixtures of CH_4 and H_2 were utilized as flow gases. In such a way, flower like nanostructures were obtained. The MWPECVD synthesis process induced further

studies investigating the mechanisms of the growth of the GNWs and searching a flexible control for their growth. In particular, one of the problems of this technique is the production of unwanted byproducts related to the usage of metal catalyst particles. Shiji and Hiramatsu succeeded to produce GNWs on a Si substrate without the use of a catalyst. They employed the RF inductively coupled plasma (ICP) (123) and a RF capacitively coupled plasma (CCP) (124) assisted by a hydrogen atom injection.

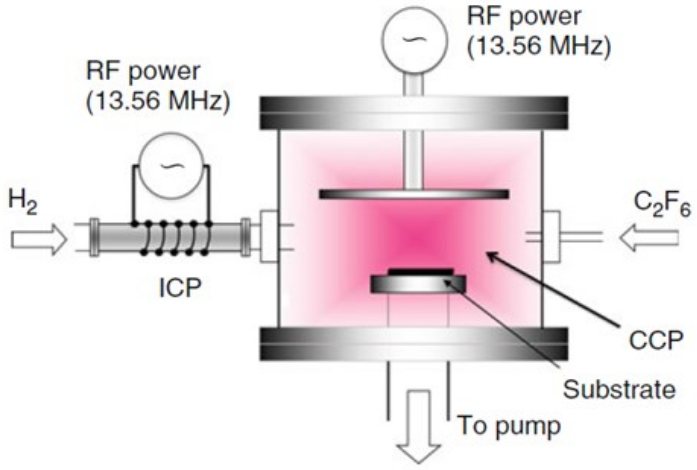

Figure 3-3: Schematic of the RF capacitively coupled plasma-enhanced CVD apparatus, assisted by a remote H radical source used for the growth of graphene nanowalls (122).

These techniques employ fluorocarbon/hydrogen mixtures as the carbon source gas. Generally, C_2F_6, CF_4, CH_4, and CHF_3 are used, and the substrate for the deposition of the GNWs is heated at temperatures of about 500°C. The high-density plasmas, such as the microwave plasma and inductively coupled plasma decompose H_2 molecules efficiently. This is very important, since a large number of H, atoms are required for the growth of the graphene nanowalls. The studies carried out by Shiji and Hiramatsu showed that the structure and growth rate of these nanostructures depend on the type of carbon source gases employed. However, even if for both the RF techniques (ICP and CCP) the catalyst is not necessary, they are not able to provide a large-scale production of GNWs. Consequently, scalable techniques should be investigated in order to employ the graphene nanowalls at the industrial level. A promising method is the hot filament chemical vapor deposition method (HFCVD), which enables to access the large scales easily compared with the above two methods. This technique can be applied to synthesize either carbon nanotubes or the nanowalls. A simplified schematic of HFCVD system is shown in Figure 3-4.

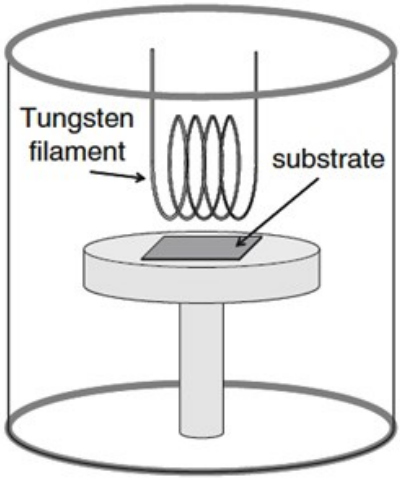

Figure 3-4: Schematic of GNWs synthesis with HFCVD method (122).

In this technique, single, or multiple tungsten (W) filaments, are heated to 2000-2200°Cand decompose a mixture of hydrocarbon and hydrogen gases. The substrate is placed within a small distance (typically 5 mm) from the filament. The deposition is carried out at pressure of 1-100 Torr and the substrate temperature is of 600-800°C. Shang et al. (125) have reported the synthesis of carbon nanoflakes using the HFCVD technique employing a mixture of C_2H_2 and H_2 gases without using catalysts or surface pretreatment. Moreover, Itoh et al. (126) reported that GNWs films have been successfully prepared using only CH_4as carbon source, temperature of the

substrate over 500°C, and with hydrogen (H_2) pressure of 133 Pa. Generally, the GNWs fabricated by HFCVD method seem less aligned compared with those fabricated by the techniques described before. This suggests that the electrical field and/or ionic species play an important role in the growth of the nanowalls.

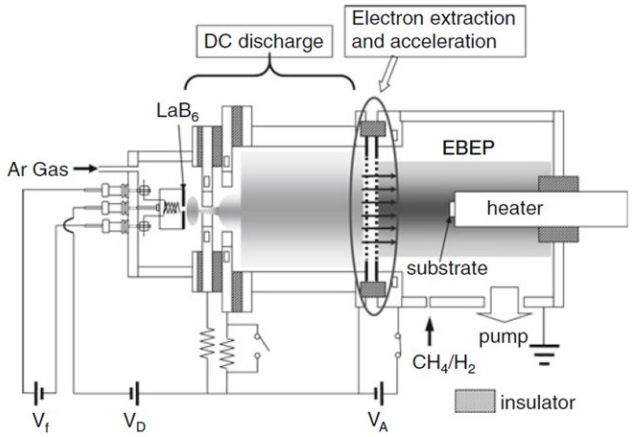

Figure 3-5: Schematic of GNWs fabrication system using electron beam excited plasma (127)

Mori et al. (128) studied the fabrication of vertically aligned and definite GNWs by an electron beam excited plasma-enhanced chemical vapor deposition (EBEPECVD) employing a mixture of CH_4 and H_2 at relatively low temperature of 570°C. Generally, an EBEP is a high-density plasma directly obtained by a high-current and low-energy electron beam. The electron-

beam energy and the electron current can be controlled independently by changing the accelerating voltage and discharge current, respectively.

By setting the electron-beam energy close to the energy corresponding to the maximum electron impact ionization cross-section of source gases, highly ionized and dissociated plasmas can be produced even at low pressures.

According to the recent reports (129), graphene nanowalls with large-surface areas and sharp edges were obtained on nickel-coated oxidized silicon substrates by PECVD in a radiofrequency Ar plasma beam injected with acetylene at temperature of 600°C. This study showed that the shape, surface distribution, and size of the nanostructures depend on the nature of the active gas and on the gas mass flow ratio in the $Ar/H_2/C_2H_2$ mixture.

Chuang et al. (127) developed a freestanding growth of GNWs by means of MWPECVD without metal catalyst and under a gas mixture of C2H2 and NH3. A growth stage facilitated the energy-intensive, localized plasma for the growth of graphene nanowalls. Due to the freestanding nature of their growth and the absence of catalyst, the synthesis process easily obtained a large scale of GNWs and processed for various applications.

There is a similar report (130) of freestanding graphite sheets with thickness less than 1 nm, in which “carbon nanosheets” were synthesized on a variety of substrates by RFPECVD without any catalyst or special substrate treatment.

3.4. Characterization of GNWs

The techniques employed for the characterization of the GNWs are the scanning electron microscopy (SEM), the transmission electron microscopy (TEM), and the Raman spectroscopy. Below are displayed some SEM, TEM and Raman images of GNWS taken from the literature.

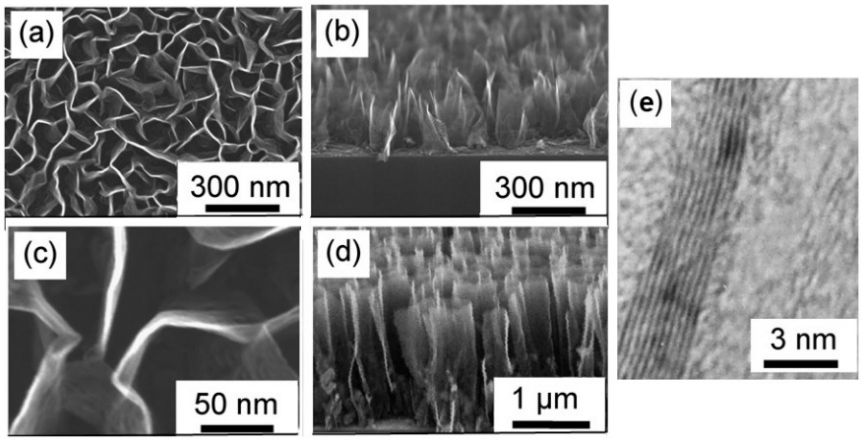

Figure 3-6: a-d) SEM images of GNWs; e) TEM image [adapted from ref. (128)].

From the SEM images it can be clearly seen the unique structure of these material. In particular, in Figure 3-6(b, d) it is possible to observe the vertical growth of the sheets on a substrate, while in Figure 3-6(a, c) the typical "wall" structure is clearly visible. In Figure 3-6(e), is shown the high resolution TEM image of the structure of the graphene nanowalls. It reveals the presence of graphene layers, indicating the graphitic structure of the material. The interlayer d spacing, between neighboring layers, was reported to be 0.34 nm as in graphite.

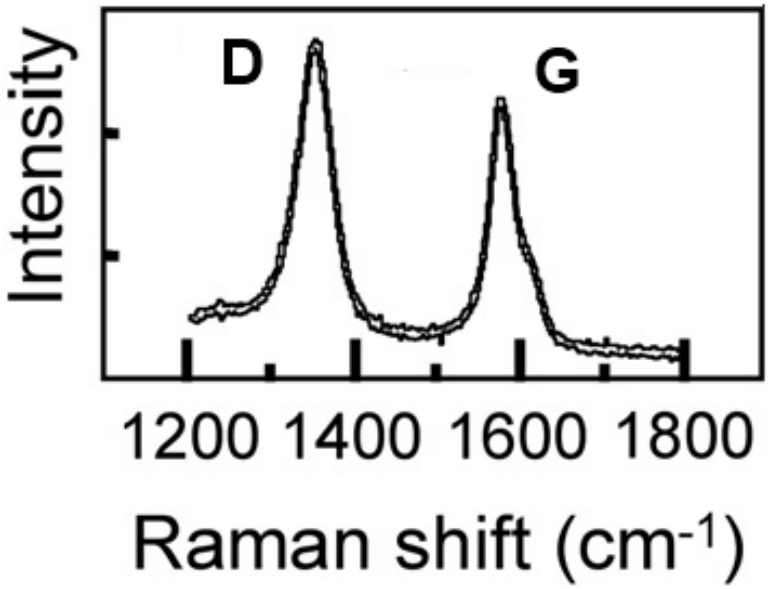

Figure 3-7: Raman spectrum of GNWs. [adapted from ref. (128)].

The Raman spectrum of GNWs in Figure 3-7, show a G peak at ~1590 cm^{-1}, indicating the presence of graphitized structure, and a D peak at 1350 cm^{-1}, which corresponds to the disorder-induced phonon mode. The presence of this peak can be mainly attributed to graphene edges with defects on the top of aligned graphene nanowalls. The comparable intensity of the D and G peaks, suggests that the GNWs are composed of nanographite, clearly visible in the TEM image in Figure 3-6(e).

3.5. Applications of Graphene Nanowalls

In paragraph 3.2, some of the potential applications of the GNWS, related to their unique structure, were cited. In particular, graphene nanowalls display sharp edges, which are potential sites for electron field emission [(35) - (120)]. While, for their high surface area could be ideal for catalyst support (121). Recently, GNWs have been also tested for use in Li-ion batteries (131) and electrochemical capacitors (132),and can also be used as a template for loading other nanomaterials and the resulting hybrid nanostructures are potentially useful for various applications (133), (134), (135).

3.6. Novel approach: Electric Field-Assisted Laser Ablation of Carbon in Water

All the techniques described for the synthesis of GNWs employ building blocks materials such as CH_4, C_2H_2, C_2F_6 for the growth of the graphene nanostructures. It is clear that any attempt to extend a building-block approach to the synthesis of GNWs must begin with the preparation of suitable molecular building blocks. With this in mind, we developed a new method (136) for the fabrication of the GNWs in which we employed the species generated by the carbon plasma generated by the laser ablation of graphite in water, the polyynes, as the starting material for the synthesis of the GNWs. In particular, the GNWs were grown at the electrodes surface during the pulsed laser ablation (PLA) of graphite target in water, under the presence of an electric field (136). Polyynes are usually produced by laser ablation of graphite in vacuum (137), but result to be unstable once they are exposed to air. They are easily oxidized and consequently destructed (21), (22), (23). Moreover, polyynes lean to undergo chain-chain cross-linking reaction towards sp^2 graphene structures as a final product (21), thus rendering the direct observation of

pure polyynes-assembled solid still a major challenge. It is clear that a method for the production of stable polyynes is needed in order to employ them as building block material for the growth of the desired carbon nanostructures. It is well accepted that, the laser ablation of carbon in a liquid medium (water, ethanol, methanol et.) has been established to be a method for the production of solutions of polyynes (138), (139), (140). Due to a well separation state in liquid, the polyynes produced in such a way result to be relatively stable, and they were reported to be degraded no less than 24 hours (141), nevertheless within the processable time they are stable. Consequently, the first step, of the method we developed was the PLA of graphite in water, for the synthesis of polyynes, e.g. the building blocks.

For what concern the second step, previously, it was reported that during the PLA, when the laser energy is high enough, the material ablated is typically converted to plasma. The produced plasma contains electrons and ions, which can be driven by external electric and magnetic fields. Therefore, the application of external electric and magnetic fields to the plasma plume can control 1) the kinetics of reactions at the plasma/liquid interface for the synthesis of product species, 2)

the clustering of these product species into various nanostructures of controlled sizes and shapes, and 3) the assembly of these nanoparticles into larger nanostructures. In addition, because the surfaces of the nanoparticles are charged, the application of an electric field during ablation and/or after their synthesis can affect their size, shape, and assembly. The use of an external electric field also assists in the fabrication of high-pressure nanophases, i.e., metastable phases of nanostructures that cannot be prepared under normal experimental conditions (142).

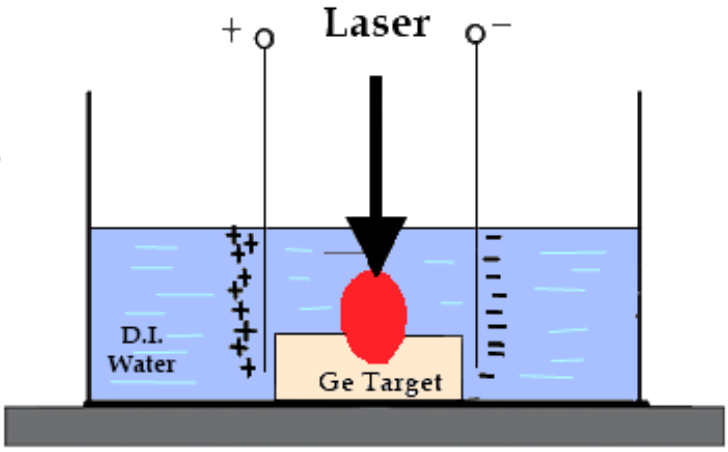

Figure 3-8: Experimental arrangement for electric-field-assisted pulsed laser ablation in liquid. Adapted from ref. (143).

For instance, P. Liu et al. (143) reported on the fabrication of GeO nanostructures with the electrical-field-assisted laser ablation in liquid of a target of Ge. In Figure 3-8, the experimental setup they employed it is displayed.

It was reported that the magnitude of the electric field drives the size and shape of the produced nanostructures. For example, in the absence of an external electric field almost all prepared particles were pure Ge spheres with the size of 300 to 400 nm. The application of ~ 14 V dc voltage resulted in nano- and micro-cubes with sizes ranging from 200 to 400 nm, while a higher voltage of ~ 30 V led to spindle-like GeO_2 nanostructures. This change in the composition and valence of Ge with the application of electric field makes it possible to conclude that electric field helps in the laser induced breakdown/decomposition of water molecules and generation of oxygen (143).

Therefore, taking into consideration the effect of an electric field on charged particles, after the laser ablation experiment, the second step of our method was the application of an electric field to two graphitic electrodes immersed in the solution containing the building blocks (polyynes). In such a way, the polyynes were transported towards one of the two

electrodes and this led to the growth of sp^2 carbon structures, which grow perpendicular to the electrode's surface, the GNWs. The technique we employed can be seen as a sort of electrophoretic deposition (EPD). Notably, EPD is commonly employed in processing of ceramics, coatings and composite materials. It is a simple, cheap high-level efficient process for production of films from colloidal suspensions, and can be applied to a great variety of materials. It is achieved via the motion of charged particles, dispersed in a suitable solvent, towards an electrode under an applied electric field. It consists of two-steps: 1) the particles suspended in a liquid are forced to move towards an electrode by applying an electric field (electrophoresis); 2) the particles are collected at the electrode and form a deposit (deposition). On the basis, of these mechanisms, we succeeded in the development of this new green and scalable approach for the synthesis of GNWs. The experimental results are reported in the next paragraph.

3.7. Experimental results

The synthesis of the building blocks was achieved performing the pulsed laser ablation of graphite in water (Millipore grade) using pulses from the second harmonic (532 nm radiation

wavelength, 5 nsec pulse duration) of a Nd:YAG laser beam (Continuum Surelite II) operating at 10 Hz repetition rate.

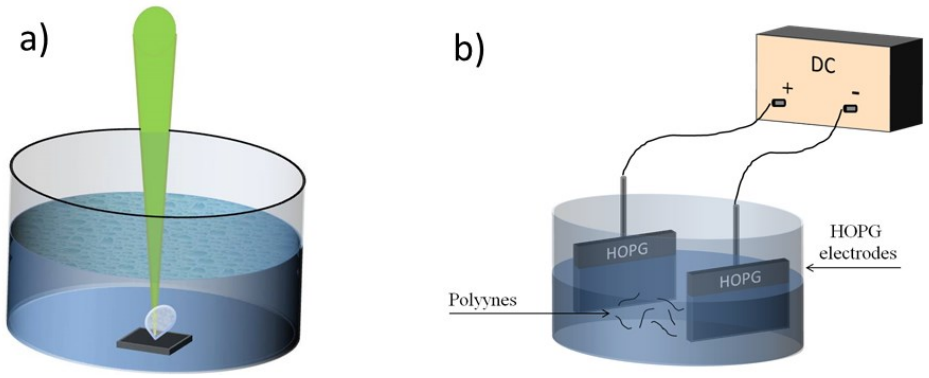

Figure 3-9: a)Setup for the experiment of Laser Ablation of graphite in water; b) Application of an electric field to two HOPG electrodes immersed in water after PLA.

The irradiation has been performed at room temperature with an optimized laser power density of 5 J/cm^2 and an irradiation time of 30 min. The target was fixed at the bottom of a Teflon flask and submerged by distilled water as shown in Figure 3-9. The deposition of polyynes and their growth into graphene nanowalls was achieved applying a 30 V DC potential to two graphitic electrodes submerged in the same Teflon flask where polyynes were produced, as shown in Figure 3-9.

The experimental results can be summarized as follows. When a graphite target is ablated in water at ~5 J/cm^2, polyynes are produced and their presence in water can be monitored by

performing UV extinction spectra in the range 190–300 nm. A typical UV spectrum obtained in such a way is reported in Figure 3-10.

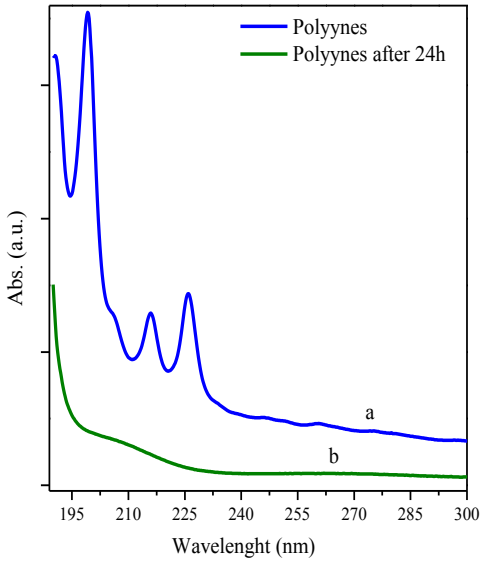

Figure 3-10: Absorption spectra of a) polyynes obtained by PLA in water; b) degradation of polyynes in water after 24 hours.

It shows a prominent absorption structure at 200 nm and two weaker signals at 216 and 226 nm. These latter have been identified as C_8H_2 species (144), while the strong signal at 200 nm and the shoulder at 207 nm are related to the presence of shorter polyynes identified as C_6H_2.

After 24 hours occurs the degradation of polyynes, Figure 3-10(b), however within the processable time, they are stable and

they can be employed as building blocks for the growth of nanostructured systems. As reported previously, polyynes produced by laser ablation in liquids are electronically charged and taking into consideration the effect of an electric field on charged particles, after the laser ablation experiment, an electric field to two graphitic electrodes immersed in water was applied. Thus, polyynes were transported at the electrodes surface and there they started to grow giving new carbon nanostructures. Different experiments were performed by varying the deposition time. In particular, in the first experiments, the electric field was applied for 20 minutes and the current was set at 30 V. After these experiments, we noticed that only on the positive electrode, there was a deposit and it was investigated by scanning electron microscopy (SEM) and the transmission electron microscopy (TEM). In Figure 3-11(a) is shown an overview of the graphene nanowalls obtained applying the electric field for 20 minutes, while (b) is a particular of the region circled in red in the overview. In Figure 3-11(c) has been reported for comparison a SEM image of GNWs obtained by RF-ICP (145). As it can be seen from the SEM images, the morphology of GNWs obtained by the technique we developed is similar to that of the graphene

nanowalls obtained by the RF-ICP technique. However, it should be noted that, the GNWs obtained did not grow much; it is as if they were still in the growth phase.

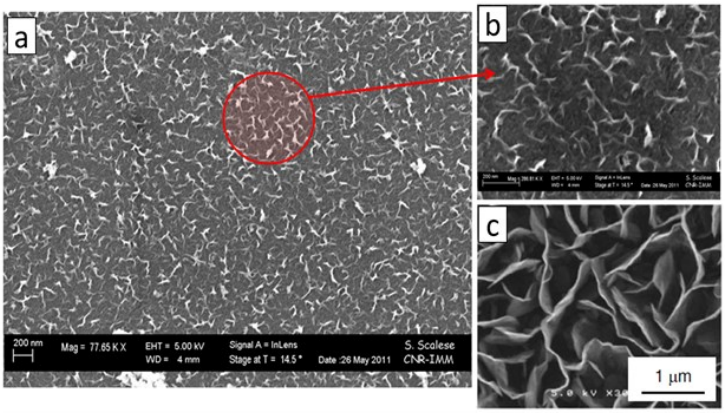

Figure 3-11: a) overview of GNWs obtained after 20 minutes of EF; b) particular of the GNWs obtained; c) GNWs synthesized by RF-ICP (145)

For such a reason the other experiments were performed by varying the time of deposition, namely the electric field was applied for 2 hours. At the end of the experiment, the nanostructures were grown on the positive electrode and SEM and TEM investigated it. Figure 3-12 shows the microscopy images (SEM and TEM) of GNWs grown on the electrode. We found that GNWs were grown only on the positive electrode surface as shown in Figure 3-12(a). This confirmed the fact that polyynes are generally negative charged and they can

migrate at the positive electrode surface under the force of the electric field, while on the negative electrode we found only amorphous carbon, as shown in Figure 3-12(c).

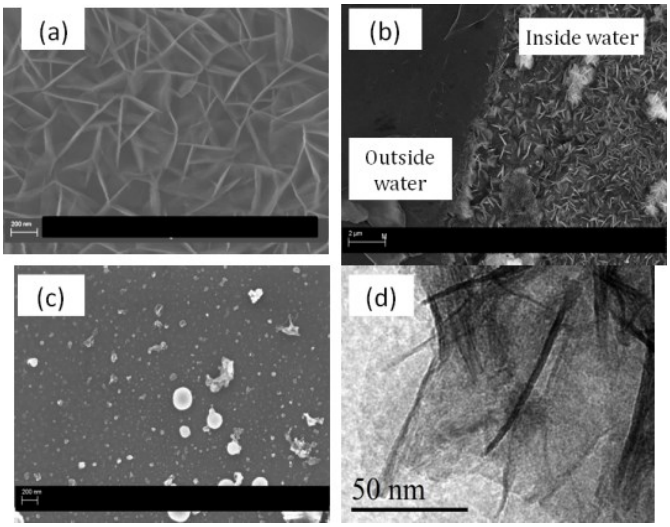

Figure 3-12: (a) SEM images of GNWs deposited after 2h ablation; (b) the deposit lay in the area submerged in water; (c) SEM image of negative electrode showing amorphous carbon; (d) HR TEM image of graphene nanowalls.

Furthermore, GNWs were grown only in the area submerged in water, Figure 3-12(b), covering uniformly the surface of the positive electrode. If we compare Figure 3-11(b) to Figure 3-12 (a), it can be noticed that by increasing the deposition time, a major quantity of graphene nanowalls could be obtained. Figure 3-12(d) shows a high resolution TEM of these systems

in which is possible to assess that these GNWs are made up of few graphene sheets (from 2 up to 6 layers). Thus, it confirms that the technique we developed leads to the synthesis of these carbon nanostructures and it represents a green and cheaper approach than the techniques employed so far.

3.7.1 GNWs growth: transport and growth mechanism of polyynes

For what concern the transport and growth mechanism of the polyynes induced by the electric field, in Figure 3-13 is reported a scheme proposed for their transport at the electrode surface.

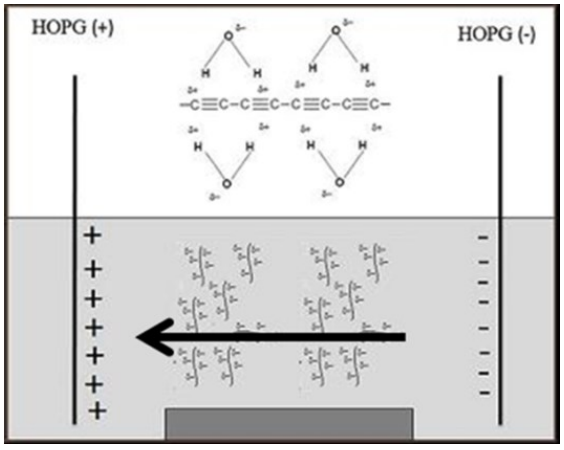

Figure 3-13: Mechanism proposed for the transport of polyynes at the positive electrode surface under the application of an electric field.

As mentioned before, polyynes produced by PLA in water are negative charged and the electric field transports them at the positive electrode. When these systems arrive on the electrode surface they produce interchain cross-linking (146), which leads to sp^2 carbon structures, which grow perpendicular to the electrode's surface. A scheme for the mechanism of growth of GNWs is reported in Figure 3-14. In order to clarify these mechanisms, various experiments have been performed. In particular, after the synthesis of polyynes by laser ablation in water, we added a salt containing sodium cations and then we have charged the two graphitic electrodes by applying a 30V DC potential for two hours.

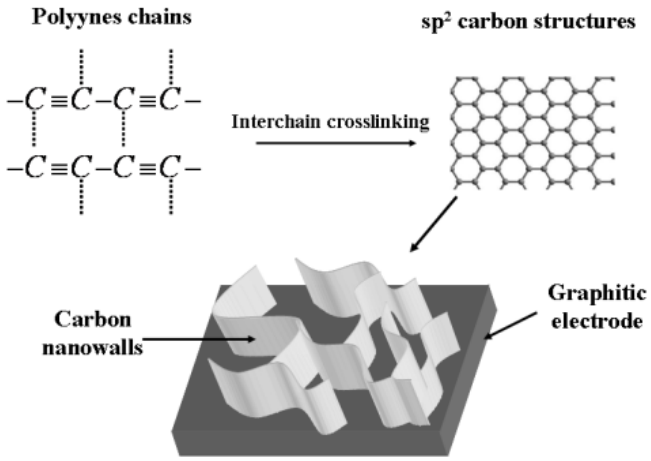

Figure 3-14: Mechanism proposed for the growth of graphene nanowalls

When we performed the SEM analysis on the two electrodes, we found that the GNWs were grown on the negative electrode and on the positive electrode, there was no trace of these systems. Hence, we have observed that when in solution there are some cations, the transport mechanism of polyynes changes, perhaps due to a change in the solvation process of polyynes, as shown in Figure 3-15.

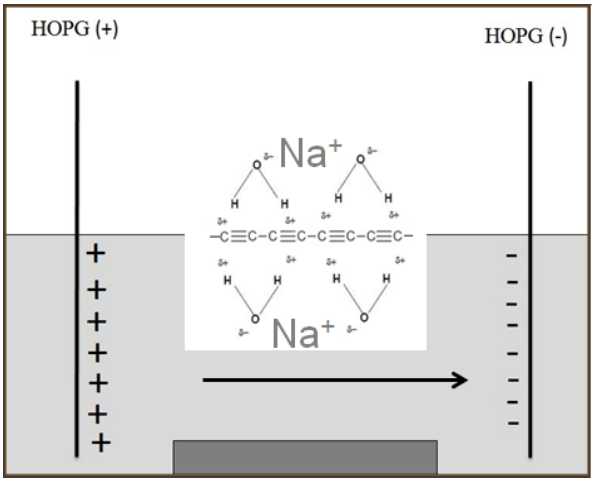

Figure 3-15: Mechanism proposed for the transport of polyynes when cations are added in water.

However, further experiments are in progress in order to clarify better the role of cations in the transport mechanism. For what concern the growth mechanism, we are certain that the species responsible for the growth of graphene nanowalls are

the polyynes, because we have monitored for two hours the variation of their concentration in water either in absence or in presence of the electric field. In particular, we have observed that the concentration of polyynes in water without the application of the electric field is almost unvaried and their degradation occurs after 5-6 hours after the laser ablation. While when the electric field is applied, the concentration of polyynes gets lower (there is a reduction of 50% of the initial concentration). Moreover, we observed that the electric field does not discriminate between the carbon chain lengths in fact we calculated that after the experiment the concentration of C_6H_2 is reduced of 50,6%, while that relative to C_8H_2 is reduced of 50%. These results are reported in Figure 3-16.

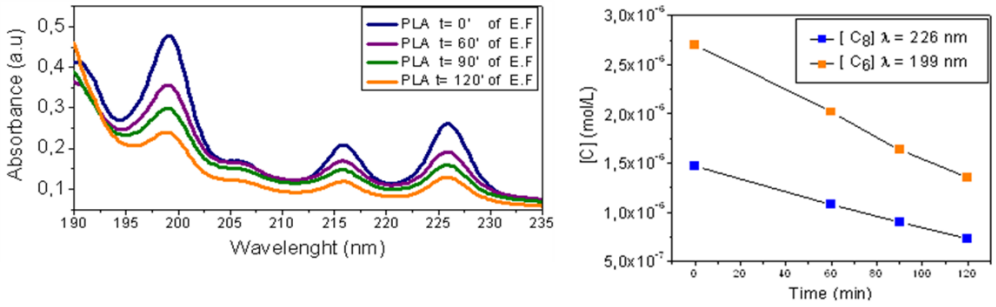

Figure 3-16: variation of polyynes concentration during the application of the electric field.

3.7.2 Growth of the GNWs on different substrates.

All the experiments described above were performed using pieces of HOPG as electrodes. However, this prevents the characterization of the nanowalls by Raman spectroscopy. In fact, this is a powerful technique for the characterization of carbon-based material. Unfortunately, when the graphene nanowalls grow on graphite, the signals of the GNWs and those of graphite overlap, preventing to have a characteristic spectrum of the GNWs. This led us to conduct experiments using different electrodes from graphite.

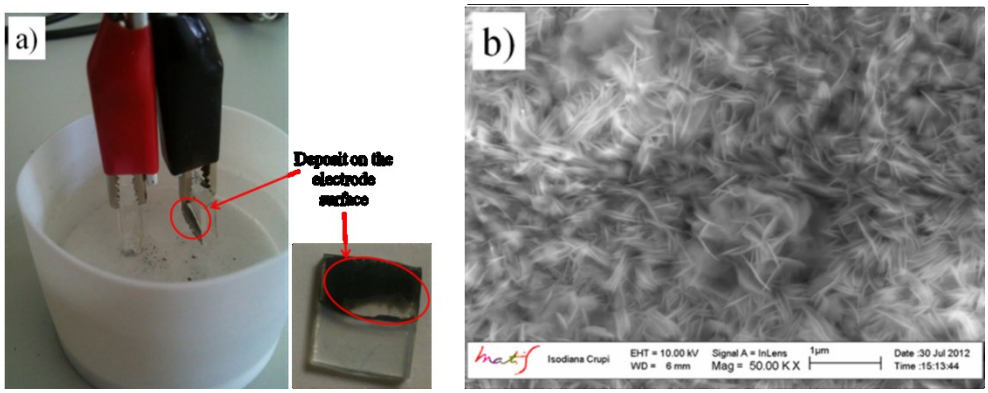

Figure 3-17: a) deposit of GNWs collected on a FTO electrode; b) SEM image of the GNWs obtained

We carried out an experiment keeping the entire parameters constant (deposition time (2h) and voltage), except for the type of electrodes. In particular, we used as electrodes the Fluorine-doped tin oxide (FTO) coated glass, which is electrically conductive and ideal for use in a wide range of devices, including applications such as opto-electronics, touch screen displays and many others. As expected, we succeeded in growing the GNWs on these electrodes. In the figure below a photo of the deposit on the electrode and the SEM images of the graphene nanowalls obtained are reported. The method we developed for the production of graphene nanowalls with an electrophoretic deposition (EPD), employing polyynes as starting materials, is a novel bottom up approach and these data have been already published (93).

3.8. Porous Graphene (PG)

Generally, porous materials contain holes either with random or high regularity. Depending on their diameters, the pores can be classified in micropores (diameters below 2 nm), mesopores in the range 2-50 nm, and for diameters above 50 nm, the pores are labeled macropores. Porous carbons are the most employed porous materials, for their high surface areas,

hydrophobic nature, and low cost manufacture. They are of great interest, due to their applications in water and air purification. In particular, the porous carbons with micropores are used as molecular sieves, and in catalysis. While, the ones displaying mesopores and macropores, are usually employed for the adsorption of large hydrophobic molecules, for chromatographic separations and electrochemical capacitors (147). Porous carbons are usually obtained *via* carbonization of precursors of natural or synthetic origin, followed by activation (148). Recently, the possibility of using graphene as membrane for gas purification, or for the gas storage, has been located at the spotlight of latest energy-related research (149; 150; 151). In particular, researchers are studying different approaches for the synthesis of the porous graphene (PG). This material can be described as a graphene sheet with nanopores originating from the removal of some sp^2 carbon atoms from the plane (152). Due to the porous structure of the layers, the properties of PG differ from those of graphene, leading to its application as a membrane in molecular sieves (37), gas separation (38), hydrogen storage (40), and as functional components in nanoelectronics. In the next paragraphs, the properties and the potential applications of PG will be

discussed. Moreover, a review of the techniques employed so far, for the synthesis of PG will be described together with the new top down method I developed during the third year of PhD.

3.9. Properties of PG

- Microstructure

Porous graphene is a modified graphene sheet, where the absence of carbon atoms within the plane creates some holes/pores. Recently, Bieri and coworkers (153) produced a form of porous graphene, with a regular distribution of the pores. Noteworthy, the authors fabricated a two-dimensional (2D) polyphenylene networks with single-atom wide pores and sub-nanometer periodicity by the aryl–aryl coupling on a metal surface (153). The pores in 2D polyphenylene are natural and uniformly distributed with the same width, however polyphenylene resembles graphene, with periodically missing phenyl rings, so the structure of porous graphene can be described employing the structure of the 2D polyphenylene. The unit cell of graphene contains two carbon atoms, while for a 2D polyphenylene layer in a 3x3 supercell, the unit cell is

composed of two C_6H_3 rings, which are linked by a C–C bond (154). As shown in, the optimized lattice parameter for 2D polyphenylene is a = b = 7.455 Å (which is also the distance between two pores), and agrees well with the experimental value (7.4 Å) (153; 154).

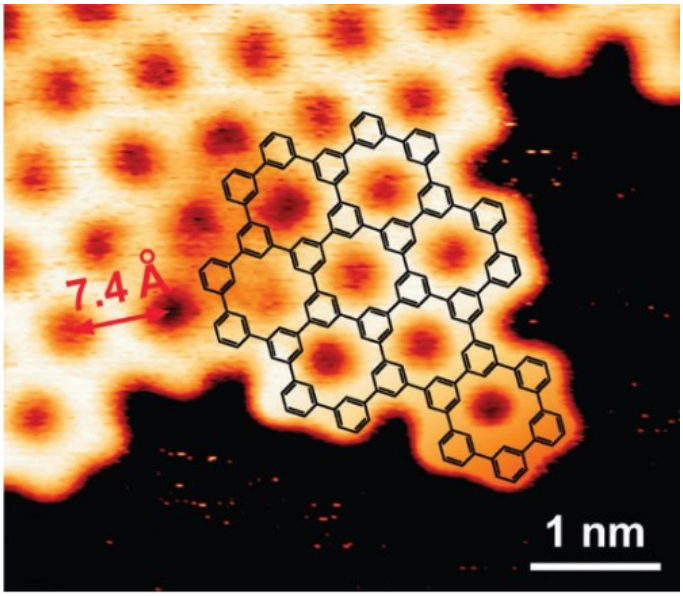

Figure 3-18: STM image of 2D polyphenylene, model for porous graphene. Taken from ref. (153)

The pores of 2D polyphenylene show electron-deficient character and the pore is hexagonal in shape and the width of pore is estimated to be almost 2.48 Å (154).

- Mechanical, Chemical, Physical Properties

Pure graphene, as aforementioned, displays outstanding properties. For instance, the value of the Young's modulus ranges from 0.5 TPa (155), measured using atomic force microscope (AFM), to 1.0 TPa calculated by Lee et al. (156), who measured the elastic properties and intrinsic breaking strength of free-standing monolayer graphene membranes by nanoindentation in an AFM, and their experiments established graphene as the strongest material ever measured. The in-plane thermal conductivity of graphene at room temperature is among the highest of any known material, about 2000–4000 $Wm^{-1}K^{-1}$ for freely suspended samples, even if some works report a value of K ranging from 600 to 5000 $Wm^{-1}K^{-1}$ (157; 158; 159). Porous graphene derives from graphene; therefore, it can take advantage of these properties. In particular, porous graphene can enhance graphene performances, since it was reported that the modification of graphene structure could improve its properties (31; 32; 33). Consequently, in the last years, many studies have conducted on the properties of porous graphene. As expected, it displays remarkable features such as low density (160), large specific surface area (up to 3100 $m^2\ g^{-1}$) (161), gas permeability (38), higher specific

capacitance (162), etc. Consequently, porous graphene has been proposed for various applications, such as gas separation (163; 164; 165), energy storage units in lithium batteries and supercapacitors (166; 167), and nanoelectronics (40; 41).

- Electronic Structure

One of the limitations of pure graphene in nanoelectronics is the lack of a band gap (40; 168). Therefore, for several years, researchers studied a way for induce a band gap opening of graphene by doping (40; 168), chemical functionalization (169), and introduction of defects and pores (170). Many computational studies (171; 172; 173) demonstrated that the presence of holes/pores within the graphene plane could induce a band opening in graphene. In Figure 3-19 is shown the band structure for graphene and hydrogenated porous graphene (HPG) (171). For pure graphene, the gap value is 0 eV, while for porous graphene, De La Pierre and coworkers, found a value of 3.95 eV (171).The reason why porous graphene has a larger band gap, is due to its peculiar aromatic structure. Resonant π bonds are present only inside the benzene-like rings; single C−C bonds that interconnect rings

isolate their aromatic units, hindering electron delocalization on the whole structure (contrary to case of graphene) (171).

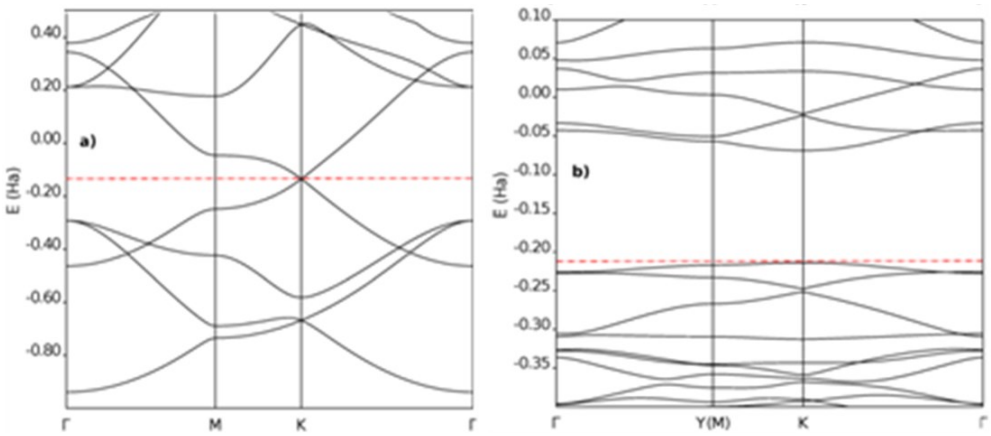

Figure 3-19: Computed electronic bands for (a) graphene, (b) HPG. Taken from ref (171)

Depending on the computational methods employed, the band gap values of porous graphene can widely vary. For instance, the density functional theory (DFT) study conducted by Brunetto et al (172) gave a value of 3.3 eV for HPG, which is about 20% smaller than the results reported by De La Pierre (171). The reason is due to the fact that, pure generalized gradient approximation (GGA) functionals underestimate experimental band gap values, while hybrid functionals are usually closer to experiments (173). Du et al. (40) predicted for porous graphene a band gap of 3.2 eV, for a calculation with

the HSE06 hybrid functional (a functional developed by Heyed, Scuseria, and Ernzerhf). This value get smaller, reaching the value of 2,34 eV, when local density approximation (LDA) calculations are employed. Despite these studies showed different values of the band gap of porous graphene, the most attractive thing is that the presence of pores induces a band gap opening. In light of these results, many studies have been conducted in order to use porous graphene in nanoelectronics (40; 41).

3.10. Potential Applications of PG

The interest toward porous graphene is related to its particular properties, which differ from those of pure graphene, due to the spongy structure. One of the potential applications is its use as membrane for gas separation and purification. The pure graphene, due to its densely packed honeycomb lattice, is impermeable to gas and cannot be employed. However, the presence of holes within the graphene plane is necessary to achieve the gas permeability (38), and for this reason, porous graphene has been extensively studied for its use as membrane for gas separation (163; 164; 165). In a theoretical study performed in 2008 by Sint et al. (174), the authors

designed functionalized nanopores in graphene sheets and showed that the resulting material could be employed as ionic sieve of high selectivity and transparency. The calculations were done on chemically modified graphene nanopores. The F-N-pores were terminated by negatively charged nitrogen and fluorine, favoring the passage of cations, while H-pores were terminated by positively charged hydrogen, favoring the passage of anions. Using molecular dynamics (MD), the authors modeled the passage of different hydrated ions through the nanopores. In the MD simulations, the sheet was placed in a periodic unit cell with ~10 Å of water on each side. One ion was placed in the cell and driven by an electric field *E* applied in the direction perpendicular to the graphene sheet. From the simulations, it was found that the Li+, Na+, and K+ ions only pass the F-N-pore, while the Cl- and Br- ions only pass the H-pore. This selectivity of the nanopores, even in the presence of a large driving field of *E* =0.1 V/nm, is caused by the Coulomb coupling between the ion and the functional groups attached to the nanopore rim. Therefore, the nanopores are also highly selective to the sizes of the ions. Another theoretical study was performed by Jiang and coworkers, in which they computationally demonstrated the possibility of

using the porous graphene as a membrane for the separation of molecular gases (38). In particular, by designing subnanometer-sized pores and modeling their selective diffusion of gas molecules with first principles methods, the authors found out the selectivity of the pores for H_2 over CH_4. Koenig (37) has demonstrated these theoretical studies, on the use of porous graphene as membrane for molecular sieving, in 2012. In this experiment, graphene sheets were prepared by mechanical exfoliation of graphite and deposited on a silicon substrate where an array of circles was previously defined. The pores were then introduced in the graphene sheets, by ultraviolet-induced oxidative etching. The molecular transport of different gases (H_2, CO_2, Ar, CH_4, N_2 and SF_6) through the pores was measured using a pressurized blister test and mechanical resonance. The measured gas leak rates resulted to be consistent with the theoretical models in the literature based on effusion through angstrom-sized pores (38; 164).

As regard the applications in nanoelectronics, pure graphene, as aforementioned, is a zero-gap semiconductor (151) and it cannot be employed for field-effect transistors (27), and many efforts have been done in order to open a band gap. However, cutting graphene sheets into nanoribbons and creating some

holes in the graphene plane can open a band gap, leading to the use of these modified sheets for the fabrication of transistors (175). Porous graphene, due to the presence of holes in the plane, has a band gap that vary from 2.3 up to 3,95 eV depending on the computational methods employed (171; 172; 173). For such reason, porous graphene has been considered a promising material for the fabrication of field-effect transistors, as demonstrated by Bai and coworkers (41). In particular, the authors produced “graphene nanomeshes”, which are single- and few-layers graphene sheets into which a high density of nanoscale holes has been created using block copolymer lithography. Moreover, controlling the etching during the fabrication process, the authors stated it was possible to control both the neck widths and the periodicities of the holes. To test the electronic properties of the prepared graphene nanomeshes (GNMs), Bai fabricated a graphene nanomesh-transistor (GNM-FET) and performed electrical transport studies. A scheme of the GNW-FET is reported in Figure 3-20.

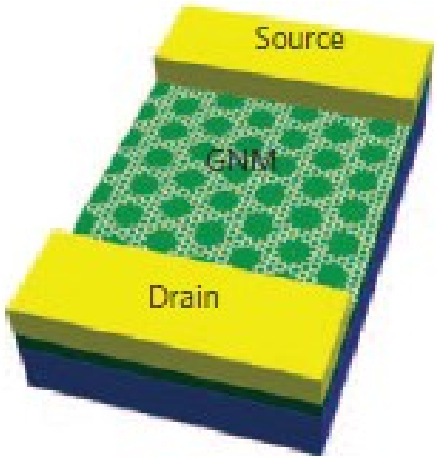

Figure 3-20: Scheme of GNM-FET. Taken from ref. (41)

The three-terminal device was made using the GNM as the semiconducting channel, electron-beam evaporated titanium/gold pads as the source–drain contacts, a highly doped p-type silicon substrate as the back gate, and a 300-nm thermal oxide as the gate dielectric. Employing this system, Bai and coworkers, demonstrated that the GNM-FET can supports currents nearly 100 times greater than that of an individual graphene nanoribbons device, but with a comparable on–off ratio that is tunable by varying the neck width.

3.11. Synthesis of PG

Porous graphene, as aforementioned, is a graphene sheet, where some carbon atoms in the plane are missing. Therefore, some holes (pores) could be created within the plane. The methods employed so far for the synthesis of porous graphene, are summarized below, and involve either physical or chemical approaches.

3.11.1 Modification of Suspended Graphene Sheets by Exposure to an Electron Beam

Fischbein et al. (176) demonstrated the formation of nanopores in suspended graphene sheets by controlled exposure of the sheets to a focused electron beam of a transmission electron microscope (TEM) apparatus. In that experiment, the graphene samples were prepared by mechanical exfoliation of graphite and then transferred to a ~50-nm-thick suspended SiNx membrane substrate.

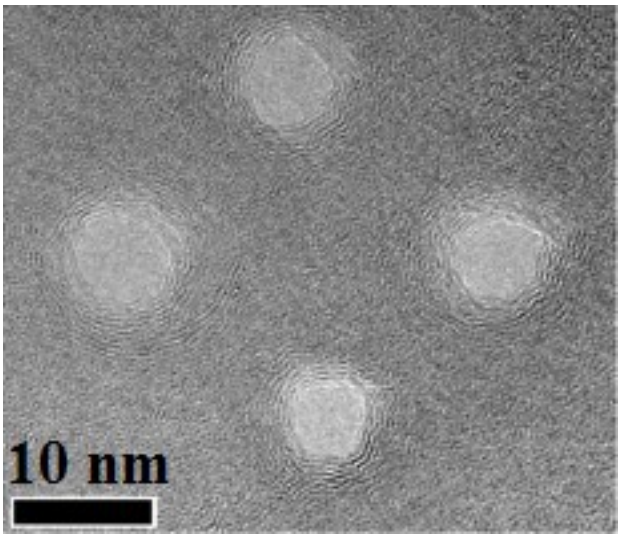

Figure 3-21: TEM images of pores created on suspended graphene sheets electron beam ablation. [Taken from ref. (176)]

Before the transfer, the SiNx membrane was patterned with arrays of ~1-um^2 holes. By increasing the TEM magnification and condensing the imaging electron beam to its minimum diameter, ~1 nm, and moving the beam position with the condenser deflectors, the pores were created, as shown in the Figure 3-21. The authors also demonstrated that the porous graphene obtained in such way resulted to be very stable. Moreover, the removal of carbon did not introduce distortions of the graphene sheet, such as folds or wrinkles.

3.11.2 Graphene Sheets Etched with Nitrogen in a Scanning Electron Microscope (SEM)

A low-energy focused electron beam in a SEM apparatus with nitrogen gas, successfully produced nanopores of < 10 nm in size in graphene sheets (177), as shown in Figure 3-22.

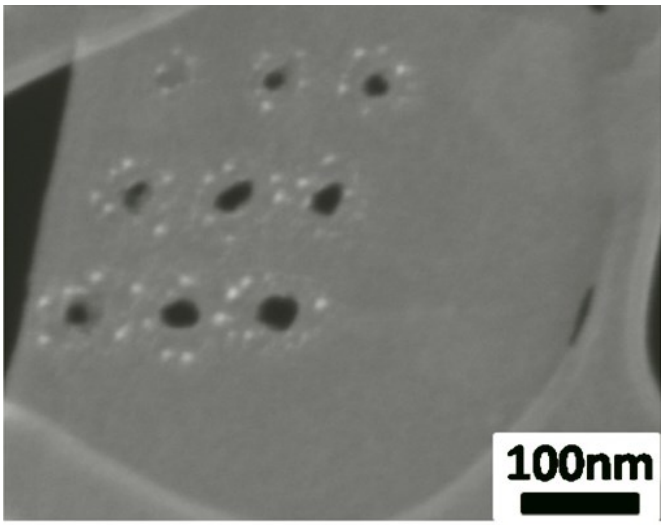

Figure 3-22: Nanopores formed in a graphene sheet after nitrogen etching in a SEM apparatus. [Adapted from ref. (177)]

For the preparation of the graphene sheets, graphite was sonicated in isopropanol for 48h, and after centrifugation, the dispersion was dropped onto a lacey carbon grid and dried naturally. The obtained sample was then placed in a SEM

chamber and the electron beam was focused onto the surface of the graphene sheet. The authors found out that, the graphene etching occurred when the electron was focused in the presence of a flux of nitrogen gas, delivered through a nozzle inside the SEM chamber. As a consequence, nanopores with a diameter of <10nm were introduced within the graphene plane, and a degradation of the graphene structure occurred leading the introduction of lattice damage and amorphization.

3.11.3 Etching of Graphene Sheets by MnO_2

The chemical synthesis of porous graphene is the method reported by Fan et al. (162). The authors succeeded in the production of porous graphene nanosheets (PGNs) by the etching of carbon atoms on the graphene sheets by MnO_2.

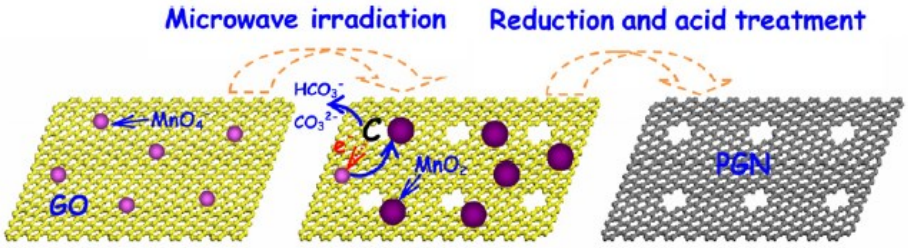

Figure 3-23: Scheme for the formation of PG. Adapted from ref. (162).

A scheme of the process developed by Fan is reported in Figure 3-23. The starting material was the graphene oxide, synthesized from graphite by a modified Hummers method. In order to obtain the porous graphene, the GO was firstly dispersed in deionized water and the obtained solution was ultrasonicated. The resulting solution was mixed with $KMnO_4$, and then the suspension was heated using a microwave oven. The product obtained was mixed with water and hydrazine solution. In the last step of the reaction, the product was washed with oxalic acid and hydrochloric acid, water and ethanol. The reaction that takes place is:

$$4(MnO_4)^- + 3C + H_2O \rightleftharpoons 4MnO_2 + (CO_3)^{2-} + 2(HCO_3)^- \qquad (162)$$

According to this equation, the carbon atoms serve as a sacrificial reductant and convert the aqueous permanganate (MnO_4^-) to insoluble MnO_2, which remain on the surface of the sheet. After MnO_2 removal, the resulting sheets possess a wrinkled structure and numerous mesopores, with the sizes of about 2.4 nm.

3.11.4 Photoreaction of Graphene Oxide in O_2 under UV Irradiation

Koinuma et al. (178) reported a simple approach for the production of nanopores in graphene oxide (GO) *via* photoreaction in O_2 under UV irradiation. In this experiment, a solution of graphene oxide was prepared using the Hummers method. The obtained solution was then diluted with pure water, placed on mica and dried under a vacuum. Afterward, a mercury lamp in O_2 was employed for the irradiation of the samples.

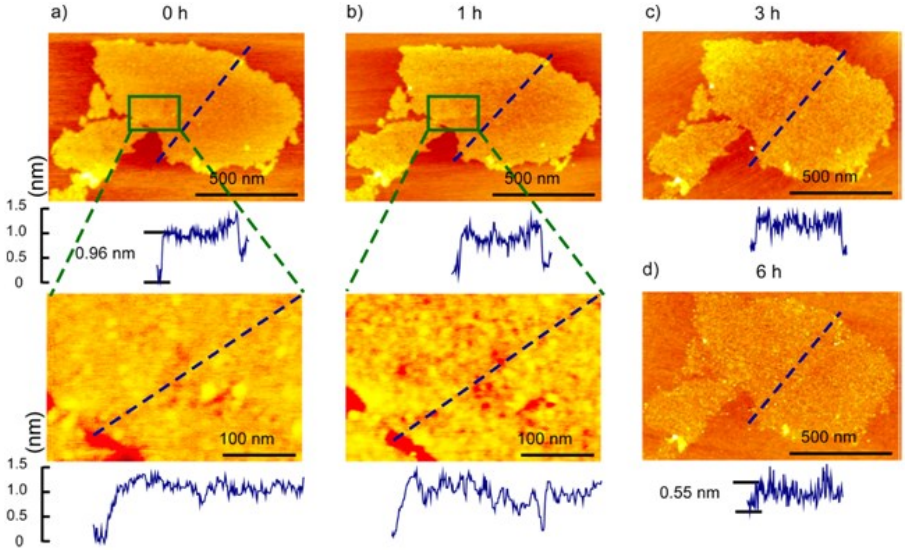

Figure 3-24: AFM images of graphene oxide after UV irradiation in O2 at different irradiation times. Adapted from ref. (178).

Atomic force microscopy (AFM) and X-ray photoelectron spectroscopy (XPS) were used for the characterization of the samples. AFM images of the samples obtained are displayed in Figure 3-24. It was found that nanopores together with reduced graphene oxide (rGO) and CO_2 were produced after 1h of irradiation in O_2. In particular, the graphene oxide consists not only of sp^2 carbon atoms, but also of oxygenated sp^3 carbon bonding domains, which are oxidized by UV irradiation in O_2. This evidence, can be explained by a mechanism similar to the coal gasification. In particular the GO contains C=C, C-C, CH, epoxide (COC), hydroxide (COH), carbonyl (C=O), and carboxide (COOH) groups, and the authors reported that the oxygen content decreased from 34 to 24 at % after the photoreaction in O_2. The reactions that take place are written below:

$$2C{=}O + H_2O(ad) \rightarrow COH + COOH \text{ (in } O_2) \quad (1)$$

$$C{=}O + COOH \rightarrow CO_2 + COH \text{ (in } O_2) \quad (2)$$

$$COC + H_2O(ad) \rightarrow 2COH \text{ (in } O_2) \quad (3)$$

$$4COH + O_2 \rightarrow 4C{=}O + 2H_2O \text{ (in } O_2) \quad (4)$$

According to the authors, the reaction 1 is the trigger reaction for the production of nanopores. In particular, some of the COOH groups could react with C=O to evolve CO_2 (reaction 2), which may produce very small size nanopores. In O_2, many C=O will be produced by reaction 4, leading to promote the reaction 2 increasing the sizes and/or number of the nanopores. The water generated by reaction 4 will promote the production of COOH (reaction 1) and COH (reactions 1 and 3) in O_2. This mechanism was confirmed by the experiments performed employing graphene sheets instead of graphene oxide. The graphene sheets contain only sp^2 π-conjugated domains, and it was found that after their UV irradiation in O_2, no pores were formed, confirming that that O_2 selectively oxidizes the sp^3 oxygenated groups of GO to produce the nanopores.

3.11.5 Novel Method for the Production of PG

The techniques described before, do not permit bulk scale fabrication of porous graphene and most of them are expensive and time consuming, involving many reaction steps. The third year of my PhD, during my research period as visiting student

at the University of Waterloo in Canada, I developed a new method for the synthesis of porous graphene and graphene quantum dots (179). This new approach represents a green and easy way for a large-scale production of these nanomaterials. In this new approach, PG and GQDs were obtained by the laser ablation of a target of HOPG in water with a femtosecond laser. In the coming paragraphs, a brief description of GQDs will be given and then the new top down approach developed for the PG and GQDs synthesis will be described in detail.

3.12. Graphene Quantum Dots (GQDs)

GQDs are zero-dimensional (0D) carbon-based nanomaterials and in the past few years, they have attracted tremendous research interest. The increasing interest towards these materials is correlated to their unique optical and electronic properties, which differ from those of graphene, due to quantum confinement and edge effects (8). Due to their extraordinary properties, GQDs are considered promising materials in the fields of chemistry, physics, materials, biology, etc. In particular, GQDs are biocompatible, strongly luminescent and can be dispersed in various solvents, showing

bright promise for integration into devices of photovoltaic (180), bio-related applications such as fluorescence labeling and bio-imaging (181), water treatment (42) and light emitting applications.

3.13. Properties of GQDs

- Morphology and Crystalline Structure

The GQDs obtained by the methods described above, show different sizes and heights according to the preparation methods. For example, Pan et al. (182; 183) were able to produce GQDs with sizes of 9.6 nm and ~3 nm, by the hydrothermal method but employing different thermal reduction temperatures and alkalinity. The heights of GQDs also depend on the preparation methods. However, the heights of GQDs prepared through the same methods increase upon the increasing sizes. This is not valid for GQDs obtained through different methods, since GQDs with larger sizes can be thinner than the smaller one (184).

As regard the crystalline structure, GQDs display an interlayer spacing that also depends on the synthetic routes adopted. For example, the GQDs prepared by the hydrothermal and

precursor pyrolysis methods possess an interlayer spacing of ~ 0.34 nm, while GQDS produced by the MAH method developed by Tang (185), showed an interlayer spacing of 0.343-0.481 nm. The increase of the interlayer spacing is mainly associated with the presence of oxygen-containing groups (O-H, C-H, and C-O-R) at the edges of the GQDs (5).

- Absorption

GQDs show two absorption peaks in the UV region: a peak at a wavelength between 200 and 270 nm due to π–π* transition of aromatic C=C bonds and a peak at wavelength longer than 260 nm assigned to n–π* transition of C=O bonds.

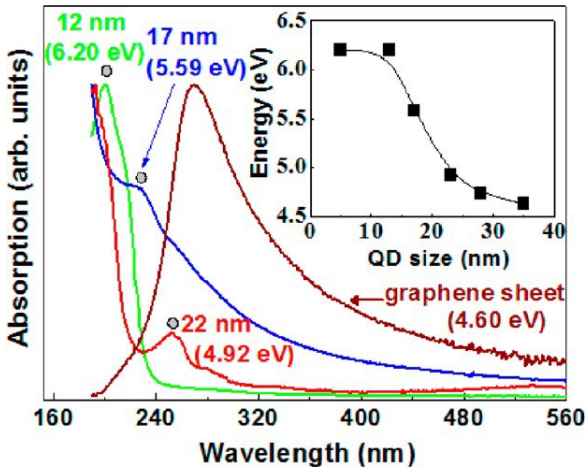

Figure 3-25: UV spectra of GQDs with different sizes. Inset: absorption peak energy as a function of average GQD size. [Taken from ref. (42)].

These peaks are usually observed in the UV-Vis spectra of GO and graphene samples, however the positions of the latter are slightly different. In particular, the π–π* transition is at 230 nm and 270 nm for GO and graphene, respectively, while the n–π* transition is at 300 nm for GO and absent in the graphene spectrum (184).
Kim et al. (186) reported the shift of the absorption peak of GQDs, with respect to that of a graphene sheet, at high energy, which further shifts to higher energy when the GQDs sizes get smaller, and this is due to the quantum confinement effect (187).

- Photoluminescence (PL)

One of the most intriguing properties of GQDs is their photoluminescence (182; 180; 186; 188; 42). In the previous paragraph, it was reported that most of the properties of GQDs are size dependent, and this is valid for the photoluminescence ones. The mechanisms of PL of GQDs are still unclear and they should be clarified (189). However, some aspects are established, for example the PL mechanism derives from intrinsic state emission induced by quantum size effect (188) and defect state emission, which arises from energy traps

(defect effect) (190; 188; 189). Since GQDs exhibit quantum confinement effect, they are luminescent. In particular, the PL emission of the GQDs varies with different sized GQDs, precisely some works demonstrated that these systems can emit blue (182; 191; 192; 186), green (183; 188; 191), and white (191) PL, as shown in Figure 3-26(a). This happens because the band gap depends on the size of the graphene fragments and generally, it decreases with the increase of the size. Consequently, size effect can result in varying PL emission with different sized GQDs.

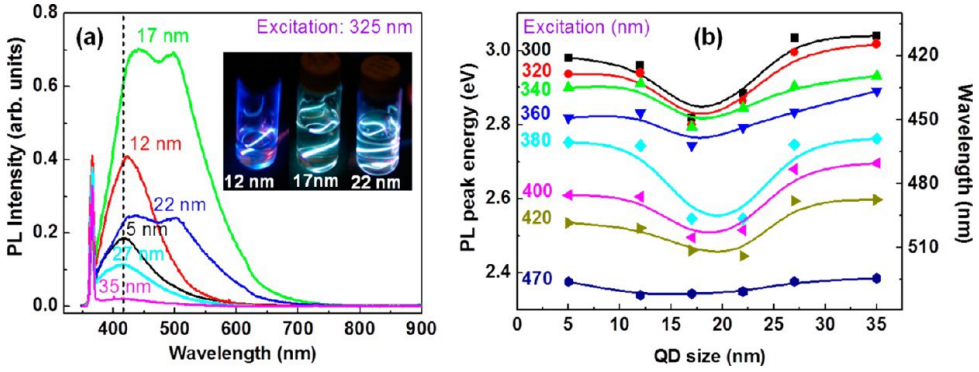

Figure 3-26: (a) Size-dependent PL spectra excited at 325 nm for GQDs of 5-35 nm average sizes. Inset: different colors of luminescence from GQDs depending on their average size for three typical GQDs of 12, 17, and 22 nm average sizes. (b) Dependence of PL peak shifts on the excitation wavelength from 300 to 470 nm for GQDs of 5-35 nm average sizes. [Taken from ref. (186)].

The PL emission wavelength and intensity depend also on the excitation wavelength, as displayed in Figure 3-26(b). For instance, Kim et al. (186) reported that, when the excitation wavelength is changed from 300 to 470 nm the PL peak shits from 420 to 520 nm. A similar behavior was reported as well by Zhu et al. (188) and this excitation dependence is due to the presence of GQDs with different sizes and/or different emissive sites (188). Therefore, when the GQDs display uniform size and emissive sites the PL spectra by varying the excitation wavelength should be almost invariable. Actually, this excitation-independent PL was demonstrated by the PL experiments carried out by Dong (192), employing the GQDs synthesized by the pyrolysis of citric acid. In particular, the GQDs possessed the maximum excitation wavelength at 362 nm and the maximum emission wavelength at 460 nm, and the changing of the excitation wavelength from 300 to 440 nm did not shift the PL peak.

3.14. Applications of GQDs

Due to their particular properties, GQDs have been proposed as materials that could be employed in photovoltaics (180), light emitting diodes (185), in environment-oriented (42) fields

and beyond. As regard the application in photovoltaics, Gupta and co-workers demonstrated that graphene quantum dots blended with regioregular poly(3-hexylthiophene-2,5-diyl) or poly(2-methoxy-5-(2-ethylhexyloxy)-1,4phenylenevinylene) polymer showed an improvement of the organic photovoltaic characteristics compared to the graphene sheets (GSs) blended conjugated polymers (180), due to improved morphological and optical characteristics. Moreover, the authors stated that by choosing different polymers or changing the types of functionalization, the performance of GQD-based devices could be improved.

The water treatment for the elimination of contaminants such as dyes, pharmaceuticals, pesticides is a topic that is in the center of many studies. Various types of physical, chemical and biological processes have been developed in order to remove these contaminants. The most employed method for the removal of dyes and organic compounds form water is the photocatalytic method with TiO_2 (193).

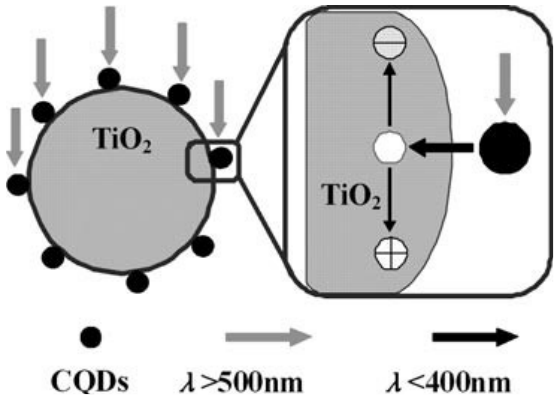

Figure 3-27: catalytic mechanism for TiO_2/GQDs under visible light proposed by Li et al (194).

In particular, the UV irradiation of TiO_2 generates charge carriers, which can destroy various organic substances (195). However, one limitation of TiO_2 for water treatment is the weak degradation under visible light due to the large band gap (about 3.2 eV) of TiO_2 (196; 197; 198). In order to improve the photocatalytic performance of TiO_2, many studies have been conducted on the doping of TiO_2 with C, N, Sn, Sr, Nb (198). Recently, the use of the new composites made with TiO_2 nanoparticles and graphene sheets has revealed an improvement of the visible light photocatalytic activity on the decomposition of the model dye methylene blue (199; 200). Two groups, Li (194) and Zhuo (42), have demonstrated that

GQDs possess excellent upconversion luminescence properties and they can be used for the design of photocatalysts (TiO_2/graphene quantum dots) to harness the use if the full spectrum of sunlight improving the phocatalytic activity of TiO_2 under visible light. The mechanism proposed by Li et al. is displayed in Figure 3-27. When the TiO_2/quantum dots nanocomposite photocatalyst is illuminated, the GQDs absorb visible light, and then emit shorter wavelength light (325 to 425 nm) as a result of upconversion, which in turn excites TiO_2 to form electron/hole (e^-/h+) pairs. The electron/hole pairs then react with the adsorbed oxidants/reducers (usually O_2/OH^-) to produce active oxygen radicals (e.g. $\bullet O^{2-}$, $\bullet OH$), which cause degradation of the model dye methylene blue (194). Moreover, Zhou in his work demonstrated that the photocatalytic activity of the system made with rutile TiO_2/GQDS was superior to the complex made with anatase TiO_2/GQDs. This evidence is due to the different bandgap values of rutile (3.0 eV) and anatase (3.2 eV) as shown in Figure 3-28.

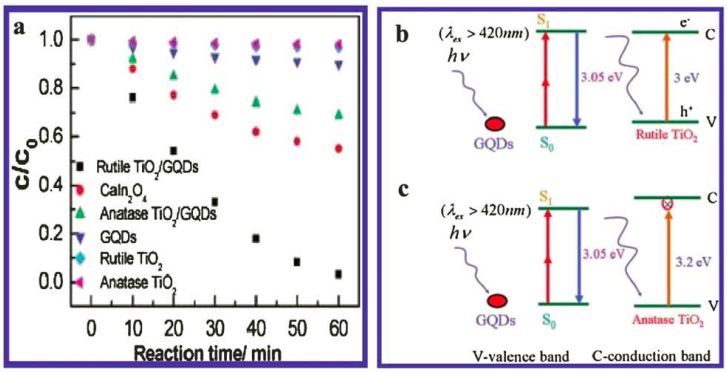

Figure 3-28: Relationship between MB concentration and reaction time for different catalysts: rutile TiO2/GQDs, CaIn2O4, anatase TiO2/GQDs, GQDs, rutile TiO2 NPs, and anatase TiO2 NPs. Schematic of photocatalytic process for (b) rutile TiO2/GQD and (c) anatase TiO2/GQD under visible light (l > 420 nm) irradiation. [From ref. (42)].

The proposed mechanism is that the upconverted PL peak of GQDs is at 407 nm (3.05 eV), which is larger in energy than the band gap of rutile TiO2 at 3.0 eV (414 nm), but smaller than that of anatase TiO2 at 3.2 eV (388 nm). Therefore, the upconversion PL emission of GQDs is capable of exciting the rutile TiO_2 but not the anatase TiO_2 to form electron/hole (e^-/h+) pairs to degrade MB (42).

3.15. Synthesis of GQDs

Generally, the methods employed for the synthesis of GQDs can be classified in two groups: top down and bottom up

methods. As regard the top down ones, since GQDs can be regarded as small fragments of graphene sheets, one of the strategies utilized for their synthesis, is to cut graphene sheets into small pieces. In particular, the common employed techniques are the hydrothermal and solvothermal breaking of graphene sheets (182), acidic oxidation (201) and the photo-Fenton reaction of graphene oxide (202).

GQDs, as mentioned before, can also be prepared trough bottom up approaches such as cyclodehydrogenation of polyphenylene precursors (203), carbonizing some special organic precursors (185; 192), etc. Some of these methods will described in the next subparagraphs.

3.15.1 Hydrothermal and Solvothermal Method

Pan and coworkers (182) produced the GQDs, with an average diameter of 9.6 nm, in 2010 by hydrothermal cutting of graphene sheets (GSs). As starting material, the authors employed GSs obtained by thermal reduction of graphene oxide sheets (GOs). Prior to the hydrothermal treatment, GSs were pretreated in concentrated H_2SO_4 and HNO_3 in order to reduce their sizes down to 50nm-2μm and to introduce

oxygen-containing functional groups at the edges, thus facilitating the solubility in water of the GSs.

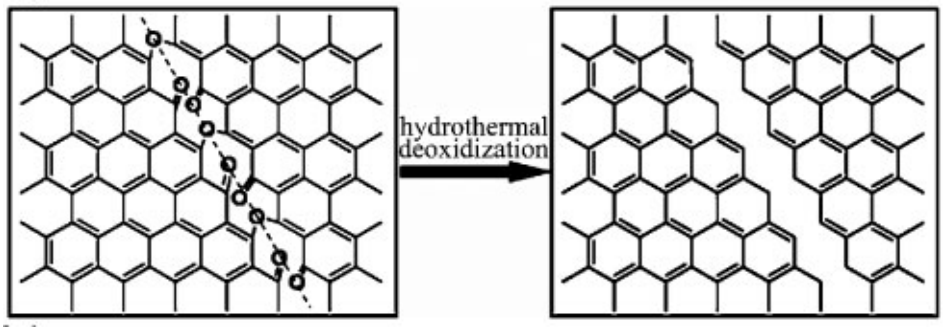

Figure 3-29: Mechanism for the hydrothermal cutting of oxidized GSs into GQDs: a mixed epoxy chain composed of epoxy and carbonyl pair groups (left) is converted into a complete cut (right) under the hydrothermal treatment. [Taken from ref. (182)].

The GQDs were obtained after the hydrothermal deoxidization of oxidized GSs under alkaline conditions (pH=8) at 200°C for 10h. The GQDs synthesized showed diameters in the range of 5-13 nm and, from the AFM results, their topographic heights were between 1-2 nm indicating that the GQDs consisted of 1-3 graphene layers. Well-crystallized GQDs were obtained, later in 2012, by the same group of Pan (183). The authors improved their hydrothermal approach employing higher temperatures (600°C) and strong alkaline conditions (pH>12) to produce GQDs with a lateral size in the range of 1.5-5 nm and a height distribution from 1.5-1.9 nm, which indicates

that the GQDs consisted of 2-3 graphene layers (183). Zhu et al. (188) in 2011 developed a new method for the synthesis of GQDs by one-step solvothermal route. In this method, the starting material was the graphene oxide (GO). It was dissolved in dimethyl formamide (DMF), sonicated for 30 minutes and heated in an autoclave at 200°C for 5 hours.

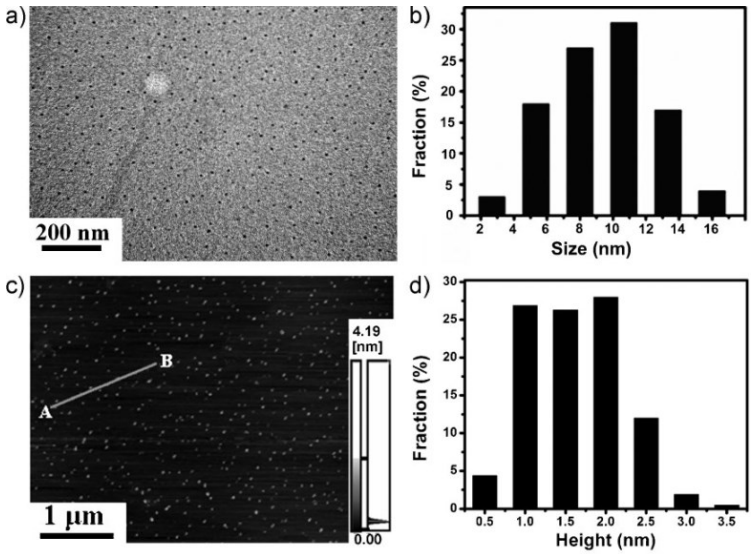

Figure 3-30: a) TEM image of the GQDs. b) Diameter distribution of the dots. c) AFM image of the dots deposited on freshly cleaved mica substrates. d) Height distribution of the dots. [Taken from ref. (182)].

The black precipitates were removed from the and after the evaporation of the solvent, GQDs were obtained with an

average diameter of 5.3 nm and an average height of 1.2 nm (1-2 graphene layers) (188).

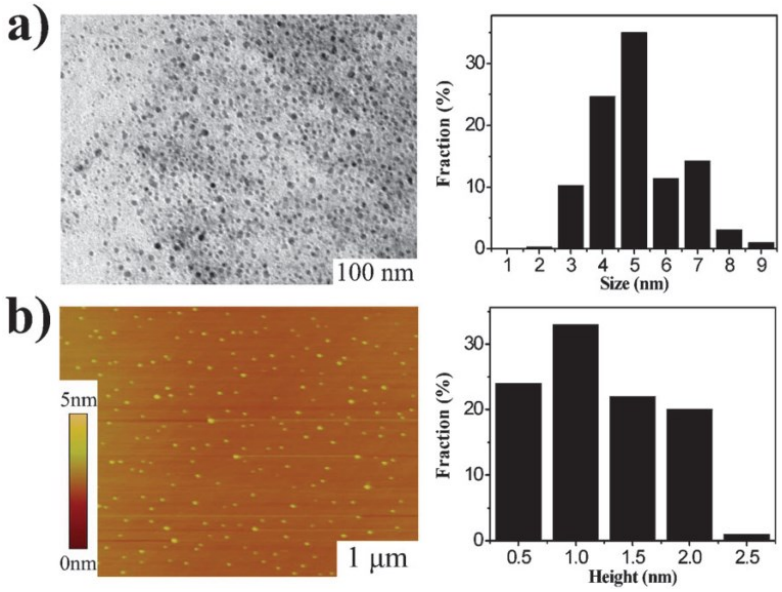

Figure 3-31: Morphology of GQDs. (a) TEM image of the GQDs (average size 5.3 nm) and their size distributions. (b) AFM image of the GQDs and their height distributions. [Taken from ref. (188)]

3.15.2 Photo-Fenton Reaction of Graphene Oxide

The Fenton reaction established in 1894 (204), has found application in many fields, especially, in the decomposition of aromatic organic pollutants in water (205; 206). It has also been demonstrated that the Fenton reaction rate could be accelerated with external irradiations, such as ultraviolet (UV)

light, that is called a photo-Fenton reaction (207). Since graphene sheets and their derivatives, such as GO sheets, could be considered as superb aromatic molecules (208) they should react with the Fenton reagent ($Fe^{2+}/Fe^{3+}/H_2O_2$). With this in mind Zhou et al., in 2012, demonstrated the production of GQDs employing the photo-Fenton reaction of GO (202). In particular, the authors demonstrated that H_2O_2 could be dissociated into hydroxyl radicals (•OH) under the photo-assisted catalysis of Fe^{2+} /Fe^{3+} in water. Under the UV irradiation, the produced hydroxyl radical attack carbon atoms connected with the hydroxyl and epoxide groups to break the C-C/C=C bonds. This reaction lead to the cutting of GO into small fragments producing the GQDs, which sizes can be controlled by varying the UV light power and photo-Fenton reaction. For example, the authors reported that 15 minutes were necessary to cut all GO sheets into GQDs, which showed an average lateral size of 40 nm and thickness of ~1.2 nm (202).

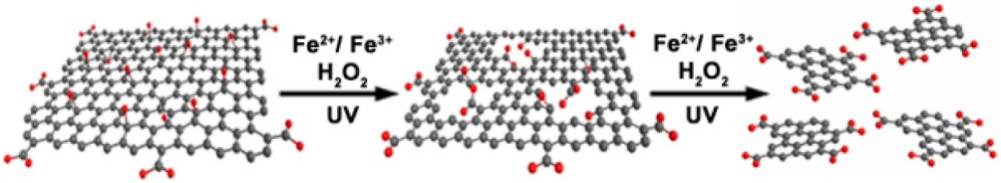

Figure 3-32: Scheme of the formation of GQDs. [taken from ref. (202)

3.15.3 Precursor Pyrolysis

The methods described previously, the hydrothermal and solvothermal cutting of GO and the photo-Fenton reaction of GO, are top down approaches. On the contrary, the precursor pyrolysis is a bottom up technique for the synthesis of GQDs. Tang et al. reported a microwave-assisted hydrothermal (MAH) method to pyrolyze the glucose (185).

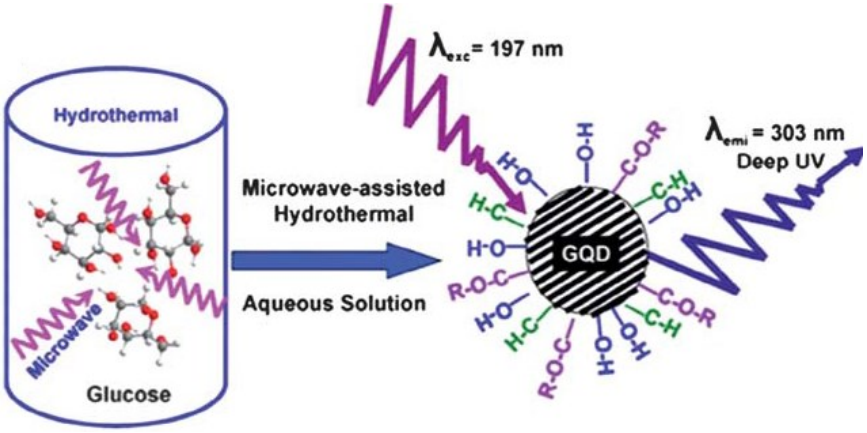

Figure 3-33: Synthesis of GQDs by pyrolysis of glucose by MAH method. [Taken from ref. (185)].

In that paper, glucose (sucrose or fructose) was pyrolyzed with microwave heating for 5 min at 595 W and then converted to GQDs, as displayed in Figure 3-33. The average diameter of the GQDs was 3.4 ±0.5 nm and the full width at half

maximum (FWHM) of the fitted size distribution was 0.55 nm, indicating the narrow distribution nature of the GQDs. The average height was 3.2 nm. The diameter of the GQDs could be tuned from 1.65 to 21 nm by simply controlling the microwave heating time from 1–9 min, and few-layer (≤10) GQDs can be obtained if the heating time was less than 5 min. By following a different approach, Dong et al. prepared GQDs by directly pyrolyzing the citric acid (192).

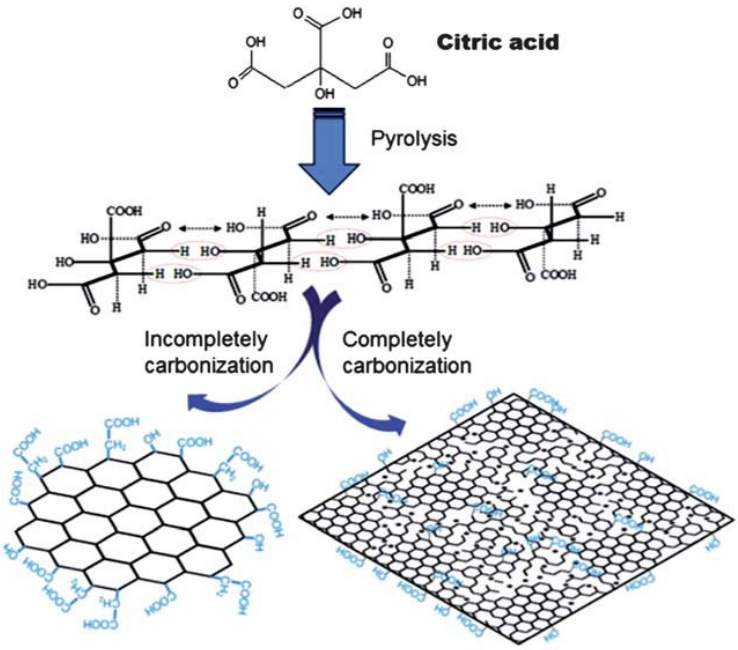

Figure 3-34: Synthesis of GQDs and GO by incomplete and complete pyrolysis of citric acid respectively. [Taken from ref. (192)]

In particular, by tuning the carbonization degree of citric acid and dispersing the carbonized products into alkaline solutions the authors obtained GQDs ~15 nm in width and 0.5–2.0 nm in thickness, as shown in Figure 3-34. Dong et al. claimed that by the incomplete pyrolysis of citric acid well surface-passivated GQDs can be obtained, while a complete carbonization of the precursor under prolonged heating lead to the formation of GO nanostructures consisting of sheets that were hundreds of nanometers in width and ~1 nm in height (192) .

3.15.4 Novel Method for the Synthesis of GQDs

As mentioned before, a novel top down approach for the synthesis of GQDs was developed during the last year of my PhD course. This method is described in the next paragraph.

3.16. Experimental results: Femtosecond Laser for the Synthesis of PG and GQDs

The third year of my PhD, I joined the group of Prof. Zhou at the University of Waterloo. During that period, I investigated the effect of femtosecond laser on the synthesis of carbon-

based materials compared to the nanosecond laser. The use of shorter pulses for the ablation of graphite produced different types of material compared to the nanosecond laser. Precisely, we succeeded in the development of a novel, green, scalable and one-pot approach for the synthesis of either PG or GQDs using the femtosecond laser ablation of graphite in water.

3.16.1 Formation of porous graphene (PG).

Solutions obtained after the laser ablation experiments performed at 25 J/cm^2 showed the presence of large layers floating at the water-air interface. These layers, recovered onto suitable substrates, were first characterized by optical microscopy imaging, which permits the distinction of a single layer graphene sheet (SLG) from bi- or multi-layers of graphene because of different contrasts. However, for a firm identification of these layers, this technique requires graphene layers to be deposited onto a silicon wafer with a certain thickness of silicon dioxide (~300 nm in thickness). The single layer usually appears as a light blue sheet, and the color becomes darker as the number of layers increases; thicker samples and graphite instead appear yellow (209). Therefore,

the layers have been collected onto a silicon substrate with a 285 nm silicon dioxide. Optical images of the sheets, shown in Figure 3-35(a, b), clearly demonstrate that the fs laser ablation of HOPG, compared to the case of the nanosecond laser (93), induced the exfoliation of graphite and yielded large graphene sheets located at the water-air interface.

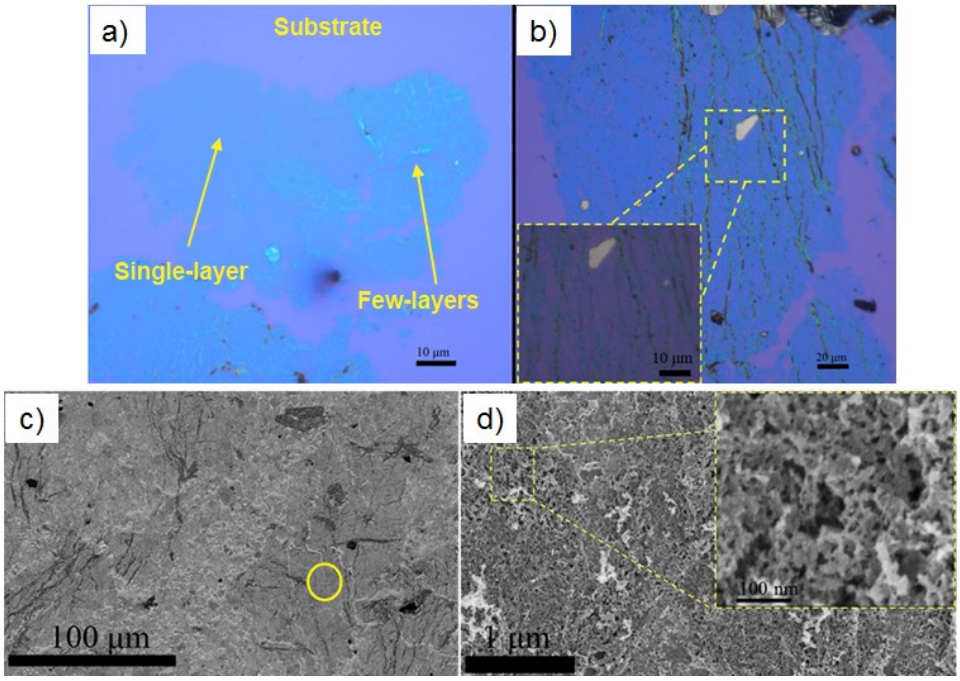

Figure 3-35: a), b) Optical images of graphene layers. a) Single and a few - layers are indicated with yellow arrows. b) A layer displaying ripples is shown. c), d) field emission SEM imaging (FEI). c) Overview of layers deposited on the substrate. d) High magnification of the area marked with a circle in figure 1c, showing the porous structure of the layers.

The average dimensions of the floating layers were found to be the range of ~100-200 μm, and once they have been collected onto the substrate, they appeared as a uniform veil. However, the fs-laser exfoliation did not provide only single layer graphene sheets. Multi-layers and some pieces of graphite were also produced, as indicated by contrast difference in Figure 3-35(a). Layers detached by the laser process, displayed a corrugated surface and some folds were also visible, as shown in Figure 3-35(b). The presence of these bends are likely related to the deposition procedure of these ultrathin layers onto the silicon substrate. Layers floating at the water-air interface were picked up using the silicon substrate at the end of the laser process. This rough collection method is expected to lead to the corrugation of the surface of the resulting layers. Moreover, the layers also exhibited a discontinuous surface where some holes were detected as clearly seen in the higher magnification inset of Figure 3-35(b). The atomic force microscopy (AFM) analysis was carried out in order to determine the morphology and the number of these layers. In Figure 3-36, a topographic image of a layer and its relative height profile are displayed. We can define the edges of the analyzed layer from AFM images, proving that the collected

materials consisted of layers with well-defined borders and that they were not agglomerated nanoparticles. This point is further supported by a post-treatment with ultra-sonication, which did not break these sheets into individual particles. Here AFM data confirm the irregular nature of the sheet, even though it is not able to give the exact number of layers involved, because of the high roughness and a limited lateral resolution.

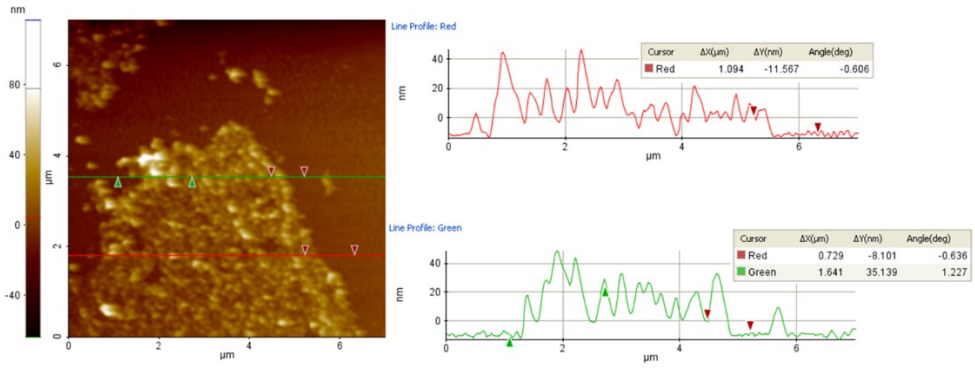

Figure 3-36: AFM image of the layer recovered from the water-air interface. The topographic image, on the left, clearly shows the roughness of the layer. The height profile is displayed on the right.

Looking at the height profile (on the right of Figure 3-36), the step between the substrate and the layer is ~ 10 nm corresponding to ~ 30 layers, as the interlayer distance in graphite is 0.34 nm. It is clear that this number of layers is

over estimated from the sheet roughness. To further elucidate layer structure, field emission scanning electron microscopy imaging (FEI) analysis was performed on the samples as shown in Figure 3-35(c, d). In particular, Figure 3-35(c) shows an overview of the suspended layers collected on the silicon substrate. It is easy to identify either layers with dimensions of ~ 100 μm covering a large area of substrate or smaller pieces about 10-20 μm in size that appear very close together so that they almost form a continuous layer. The bigger sheets possessed many ripples on the surface, while the smaller ones appear almost flat at the same magnification. The area inside the yellow circle was then examined at increased magnification, as shown in Figure 3-35(d). The irregular composition of these layers indicates that they have a three-dimensional (3D) porous structure. The pores are ~ 10-20 nm in size as shown in the inset. This porosity may be the cause of the overestimation of the height of these layers as determined from AFM analysis. All the layers collected exhibited this spongy structure independent of the size or thickness of the layer. Figure 3-37, shows an FEI image of a single layer of graphene, where many ~20nm holes are visible. Thus, porous graphene can be described as a graphene sheet

with nanopores created by the removal of carbon atoms from the plane. From FEI analysis, it is evident that all sheets detached by the laser ablation process exhibit a homogeneously porous structure. This suggests that shorter pulses not only induce either the exfoliation of the graphite as seen with longer laser pulses (93) or a modification of the detached layers.

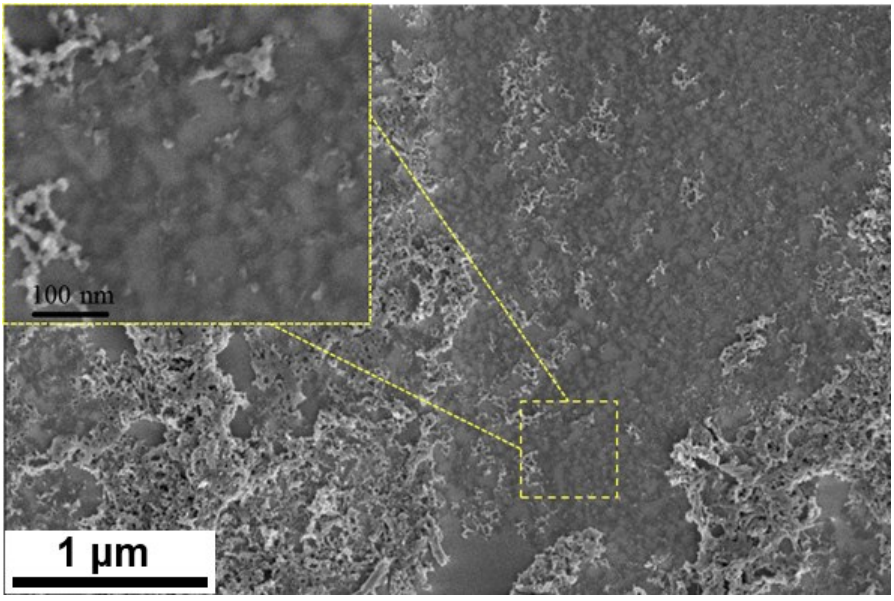

Figure 3-37: FEI image of a single layer of porous graphene. The high magnification image of the area indicated with a dashed box is displayed in the inset. Nanoholes of ~20 nm are clearly visible.

Transmission electron microscopy (TEM) images of these layers are shown in Figure 3-38. TEM samples were collected

by a lacey carbon coated copper grid, and subsequently dried naturally. Figure 3-38(a) indicates the presence of structures with different number of folded layers (between one and five) and the presence of ripples, as seen by FEI and optical microscopy. The interlayer d spacing of 0.34 nm was found to be the same as reported for graphite (210). Figure 3-38(b) shows a TEM image of a single layer of porous graphene, where the d spacing was calculated to be 0.21 nm, corresponding to the distance of the zigzag (C–C–C) chains in graphite (210).

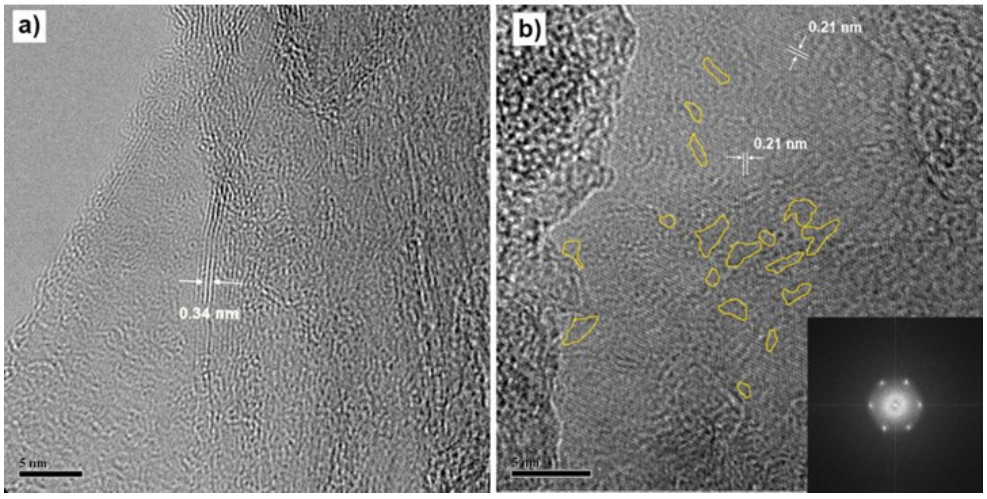

Figure 3-38: TEM images of the folded graphene layers (a) floating at the water-air interface. b) TEM image of a single layer of porous graphene. A 2D FFT of this image is reported in the inset, and the pores on the graphene sheet have been highlighted by yellow loops.

A 2D fast Fourier transform (FFT) was performed on this image and the results are shown in the inset in Figure 3-38(b). The FFT showed only six spots in a hexagonal pattern with 0.21 nm spacing, confirming the monolayer structure of graphene, consistent with prior reports (211; 212). Previous TEM studies have demonstrated the possibility of identifying the presence of defects in terms of mono-or multi- vacancies on the graphene plane (211; 213; 214; 215). Figure 3-38(b) highlights some areas where missing rows of carbon atoms can be observed. This confirms the presence of nanoholes or nanopores within the graphene network, and provides supporting evidence for the formation of porous graphene by fs ablation.

Noteworthy, all the layers recovered from solution have this porous structure, thus confirming the fact that the present technique is a simple, green, and scalable method for the exfoliation of graphite and the production of porous graphene.

3.16.2 Formation of Graphene Quantum Dots.

Following the fs ablation and after removal of the floating sheets, the solutions were analyzed by means of absorption spectroscopy. The main results are shown in Figure 3-39. The

absorption spectrum of the solution obtained after laser ablation at 25 J/cm^2 revealed the presence of an absorption peak centered at 270 nm. This peak can be attributed to the presence of GQDs (216) or graphene nanosheets (217) as it arises from the excitation of a π-plasmon resonance in the graphitic structure (218).

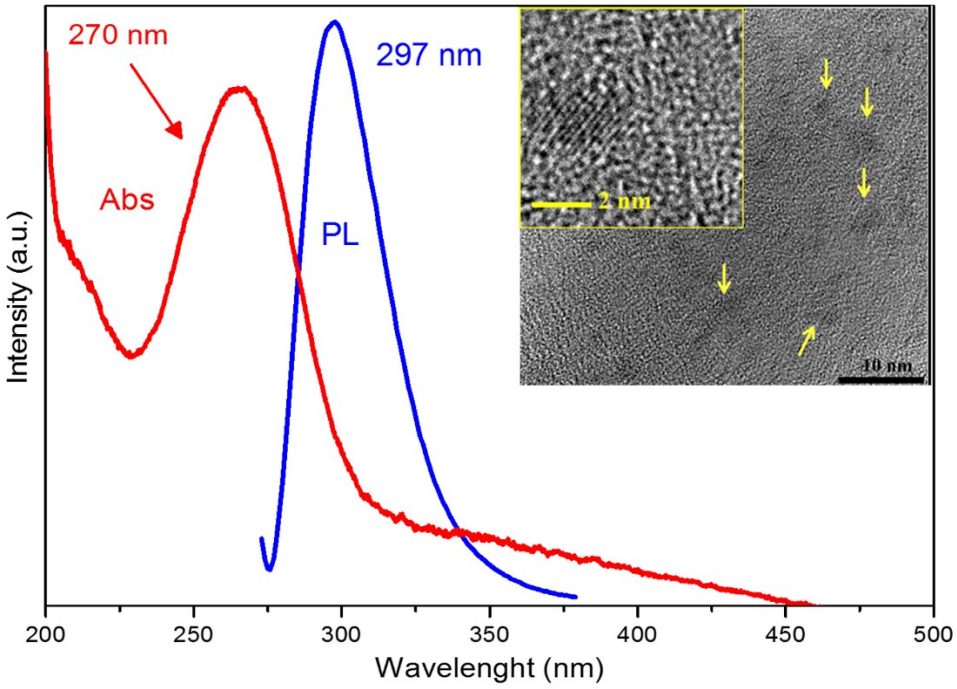

Figure 3-39: Absorption spectrum (left), and TEM images (right) of the solid component in the solution after fs ablation at 25 J/cm^2.

Recently, several groups reported that GQDs produced with different methods display photoluminescence properties (219). The luminescence mechanism of GQDs is not fully understood and it may derive from intrinsic state emission and defect state emission. In order to investigate the photoluminescence properties of our GQDs, we performed the PL analysis of the solution and the obtained spectrum is reported in Figure 3-39 (blue line). Excitation has been performed at 270 nm (absorption maximum) and PL show a single signal at 297 nm, which is blue shifted with respect to the emission of the GQDs produced with other methods. In general, depending on the synthetic path, GQDs can show blue, green, yellow and red luminescence, and it was reported that the PL emission in GQDs could be size-, excitation-, solvent- dependent. In particular, a decrease of the GQDs size leads to a blue shift of the luminescence emission. In our case, it seems that we were able to produce smaller GQDs.

For TEM characterization, some drops of the solution were deposited onto a copper grid. The results are shown on the right side of Figure 3-39. The presence of graphene quantum dots with dimensions in the order of 2-5 nm is clearly seen in this image (see the inset). The measured d spacing was 0.23

nm, which agrees well with that reported in the literature for graphene (211; 212; 220). The GQDs are embedded within an amorphous matrix, and some wrapped graphene sheets were also detected, suggesting that some graphene sheets remain dispersed in the liquid. Based on these TEM results, we conclude that the GQDs dispersed in water gave rise to the absorption band at 270 nm. Zhou et al (216) reported a similar conclusion.

The fs laser ablation experiments were also performed using lower fluence. In particular, the graphite target was ablated with a fluence of ~ 10 J/cm^2, and neither the PG layers nor the GQDs were subsequently detected in the aqueous solution. Under these conditions, the absorption spectrum of the solution showed the presence of hydrogen-terminated polyynes containing six and eight carbon atoms per chain. This suggests that the formation of both PG and GQDs depends on the laser energy during the ablation experiments. In particular, we found that in the range of 5-12 J/cm^2, polyynes (C_6 and C_8) are produced, while for fluences > 20 J/cm^2, porous graphene, and GQDs are obtained, without detectable quantities of polyynes.

3.16.3 Mechanisms proposed for the production of PG and GQDs.

In order to explain the formation of either PG or GQDs, two primary related mechanisms, should be considered. These involve laser-induced water breakdown and a laser-induced mechanism similar to that occurring in the coal gasification process.

When a fs-laser is focused into water, laser ionization and photo dissociation of water molecules leads to the formation of H, O and OH radicals as indicated in reaction (1) (221). Subsequent reactions result in the formation and evolution of H_2 and O_2 as well as H_2O_2, which acts as a strong oxidizer.

$$6H_2O \xrightarrow{Femtosecond\ laser} 8H^{\cdot} + 2O^{\cdot} + 4HO^{\cdot} \qquad (1)$$

$$\rightarrow 4H_2 + O_2 + 2H_2O_2 \qquad (2)$$

A second mechanism, related to the decomposition of water, is similar to that involved in the gasification of coal. This is a process that occurs when solid carbon-based materials react with oxygen, steam, carbon dioxide, and hydrogen to produce fuel-rich products, such as hydrogen, carbon monoxide and

methane (222). The reactions that take place can be expressed as:

$$2C(s) + O_2 \rightarrow 2CO \qquad (1)$$

Any free oxygen rapidly reacts with CO in the gas phase to produce CO_2, according to reaction (2):

$$CO + \frac{1}{2}O_2 \rightarrow CO_2 \qquad (2)$$

$$C(s) + CO_2 \rightarrow 2CO \qquad (3)$$

$$C(s) + H_2O(g) \rightarrow CO + H_2 \qquad (4)$$

$$CO + H_2O(g) \rightarrow CO_2 + H_2 \qquad (5)$$

These reactions, acting collectively, are suggested as the mechanism leading to the formation of porous graphene in the present experiments and are initiated by the decomposition of water accompanying during the femtosecond laser ablation of graphite. This results in the formation of a variety of reactive species including O_2, H_2, and H_2O_2. These species are produced throughout the ablation process, which lasts for up to 20 minutes. During ablation, the laser pulses exfoliate the graphite, leading to the detachment of graphene sheets

containing one or more layers. Subsequently, O_2 and the H_2O_2 molecules in the solution oxidize the exfoliated graphene sheets leading to the formation of up to several layers of graphene oxide (GO). This material is a graphene sheet in which carbon atoms possess sp^3 hybridization, due to their bonds with oxygen atoms, forming carbonyl (C=O), epoxide (COC), hydroxide (COH) and carboxide (COOH) groups. Finally, the sp^3 carbon atoms of the GO sheet react with O_2, in a way similar to the coal gasification mechanism, forming CO and CO_2 molecules and leaving behind a distribution of carbon vacancies in the sheet: creating nanopores. As a result, porous graphene is produced and it floats toward the water-air interface where it can be easily collected and characterized. Recently, Koinuma and coworkers have reported (178) the production of nanopores in GO sheets, *via* photoreaction in O_2 under UV irradiation. In their work, they demonstrated that, for the formation of pores carbon atoms with sp^3 hybridization must be present, as no pores were produced when sp^2 hybridized graphene sheets were subjected to the same photoreaction in O_2. The mechanisms proposed here show that the first crucial step for the synthesis of porous graphene is the breakdown of water, since it produces O_2 and H_2O_2 that

leads to the formation of GO, without which porous graphene cannot be formed. This step is confirmed by the observation of laser filamentation formation in water during fs laser exfoliation.

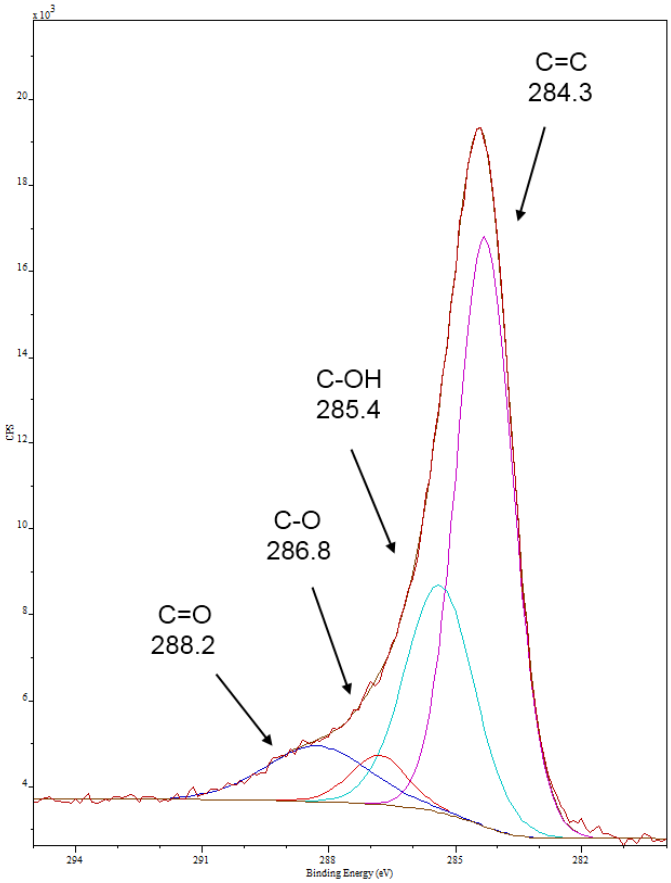

Figure 3-40: X-ray photoelectron spectra (XPS) of the layer recovered at the water air interface. The spectrum is similar to the one reported for a reduced graphene oxide, in which the content of oxygen bonded to carbon is much lower than a pure layer of graphene oxide.

The second important step is the reaction between sp^3 carbon atoms in the GO sheets with O_2, which leads to the formation of the pores. X-ray photoelectron spectroscopy (XPS) analysis of the recovered layers is shown in Figure 3-40. The spectrum is similar to that reported for graphene sheets having a very low content of oxygen (93). This indicates that GO sheets formed during the experiments are completely converted into PG as an intermediate step by the coal gasification mechanism. Previously, we stated that the nature of the layers obtained using longer laser pulses differed from those produced with shorter pulses and the sheets appeared to be almost flat without any evidence for pores. These different results can be attributed to the absence of the hydrogen peroxide in the water solution and a relatively low lattice temperature during the nanosecond laser ablation. Chin S.L. reported that when a nanosecond laser is focused into water producing breakdown only O_2 and H_2 are detected, since H_2O_2 molecules are dissociated by the shock waves of the plasma (221). Therefore, in the absence of hydrogen peroxide, graphene sheets exfoliated by ns laser pulses are subject to a lower oxidation rate than is the case with fs laser irradiation. Indeed, we demonstrated that the sheets obtained were

reduced GO sheets and that sp^2 domains were still detectable. This suggests that the concentration of sp^3 carbon atoms was small so that the coal gasification process was inhibited. In addition, as mentioned previously, the T and P generally reached during ns laser irradiation are ~ 4,000–5,000 K and several GPa (223), respectively, while T ~ 20000 K and P ~28 GPa are generated in the fs laser irradiation. With a focused fs beam, the intensity is ~ 10^{14} W/cm^2so that liquid molecules are readily ionized (224). For the coal gasification, operating temperature, operating pressure, coal particle size, and O_2/coal ratio are key process variables. In particular, a decrease in the coal size requires a higher O_2/coal ratio and very high operating temperatures (222) (up to 2200 K in oxygen-blown gasifiers). Considering these factors, *e.g.* the liquid environment, the small quantity of material produced, and quantity of ~$3x10^{-7}$ mol (221) of O_2 present, it seems that the temperature reached during the ns laser ablation experiments (~4000-5000 K) is not high enough to obtain the gasification reaction of the sp^3 carbon atoms in the graphene layers. Instead, when ultrashort pulses are used, not only hydrogen peroxide is produced, which leads to stronger oxidation of the layers, but the possibility of reaching ~ 20000

K permits the coal gasification reaction of the graphene oxide sheets and the formation of PG. The formation of GQDs is then a natural consequence of the continuing gasification of PG. During fs ablation, many layers are detached from the HOPG target. These sheets are then processed *via* the reactions described above, and some of these sheets are more easily oxidized than others. As a result, these layers contain a greater concentration of sp^3 carbon atoms so that, when they react with O_2 (coal gasification process), many holes are formed causing the destruction of the layers. After destruction of these layers, very small GQD fragments are formed and further dispersed in water. It should be noted that, as afore mentioned, the approaches reported to date in the literature for the synthesis of GQDs, consists of cutting GO layers with suitable reactants (182; 202).

3.16.4 Experiments in liquid nitrogen (N_2).

In order to prove the validity of these mechanisms, femtosecond laser ablation of HOPG was carried out in liquid nitrogen (N_2). The experiments were set at the same fluence (25 J/cm^2) and time (20 minutes) employed for the

experiments in water. The products of the ablation were collected at the end of the laser ablation by submerging a substrate of Si/SiO_2 in the remaining liquid nitrogen and waiting for its evaporation. In this way, the materials produced were allowed to deposit on the top of the substrate and then characterized by means of optical microscopy, FEI, and Raman spectroscopy. Figure 3-41 shows the results of the FEI analysis.

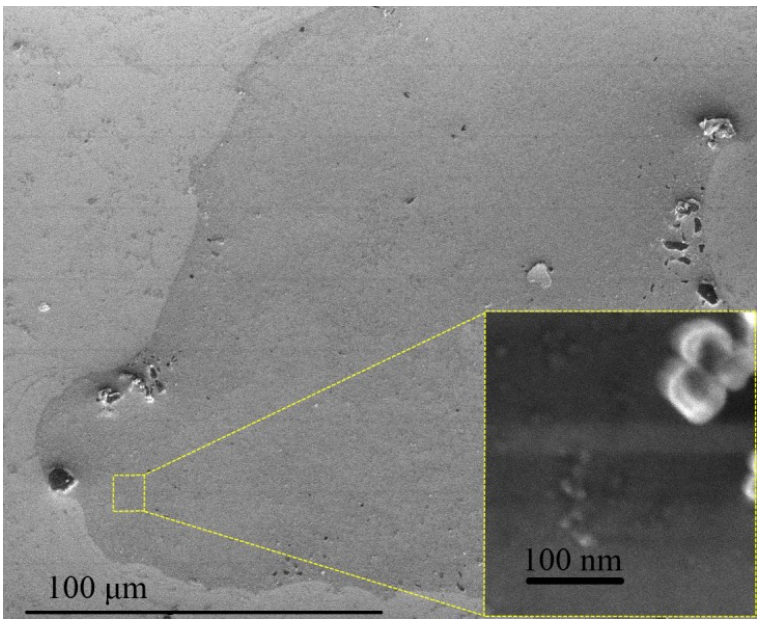

Figure 3-41: FEI image of a layer obtained after fs laser ablation of HOPG in liquid N_2. The inset shows a magnification of the area inside the yellow dashed box.

The analysis of the samples using the optical microscope (Figure 3-42) showed that exfoliation of HOPG is possible in liquid N_2. Most of the layers detached were thicker than the ones obtained in water and a large quantity of graphitic material covered the layers. However, the dimensions of the detached layers (~100 μm) were found to be comparable to those obtained after fs ablation in water (see Figure 3-42). Fs ablation of HOPG in liquid N_2 seems to be accompanied by higher ablation of the graphite target together with less efficient exfoliation. Despite this limitation, multi-layer and a few thin layers were found and they were characterized by FEI. Figure 3-41 shows the FEI image of a thin sheet, where the edges are clearly visible together with superimposed graphitic material. The absence of ripples suggests that the best way to deposit the layers is to place the substrate at the bottom of the quartz cell and let the solvent evaporate. The inset of Figure 3-41 is a high magnification FEI image of the area indicated with a dashed yellow box. It is obvious that the layer did not show the presence of pores, proving the validity of the mechanisms proposed above. Hence, for the synthesis of porous graphene both O_2 and H_2O_2 are necessary.

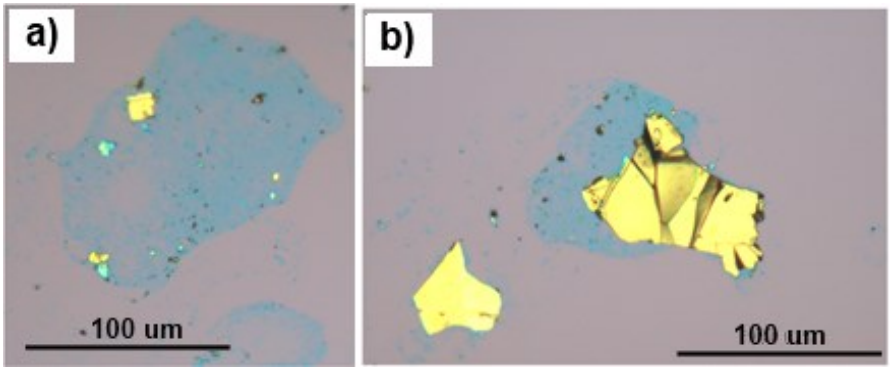

Figure 3-42: Optical images of the layers detached after fs laser ablation in N_2 and deposited onto a Si/SiO_2 substrate.

After the evaporation of the liquid nitrogen, and the removal of the substrates with the graphene layers, we observed some material attached to the walls of the beaker. These materials were recovered with water and analyzed by means of absorption spectroscopy. The results are shown in Figure 3-43(a). The absorption spectrum shows the presence of four absorption bands at 223, 235, 247, 260 nm respectively, which can be attributed to cyanopolyynes. These systems are polyyne chains ending with a cyanide functional group, and generally, they are produced by arc discharge in liquid nitrogen (225), or found in the interstellar medium (226; 227; 228). Comparing the absorption bands reported in literature (225) with that for our solutions, it is apparent that the fs-

ablation of HOPG in liquid N_2 results in the synthesis of cyanopolyynes containing eight carbon atoms per chain (C_8N_2). It was also found that the synthesis of the cyanopolyynes depended on fluence. In particular, large quantities of these molecules can be produced with fluences in the range between 20 and 30 J/cm^2, while for lower values (10-15 J/cm^2) no cyanopolyynes were detected. The fs laser ablation in liquid nitrogen has not yet been reported as a technique for the synthesis of cyanopolyynes, suggesting this is a novel and facile route for their production.

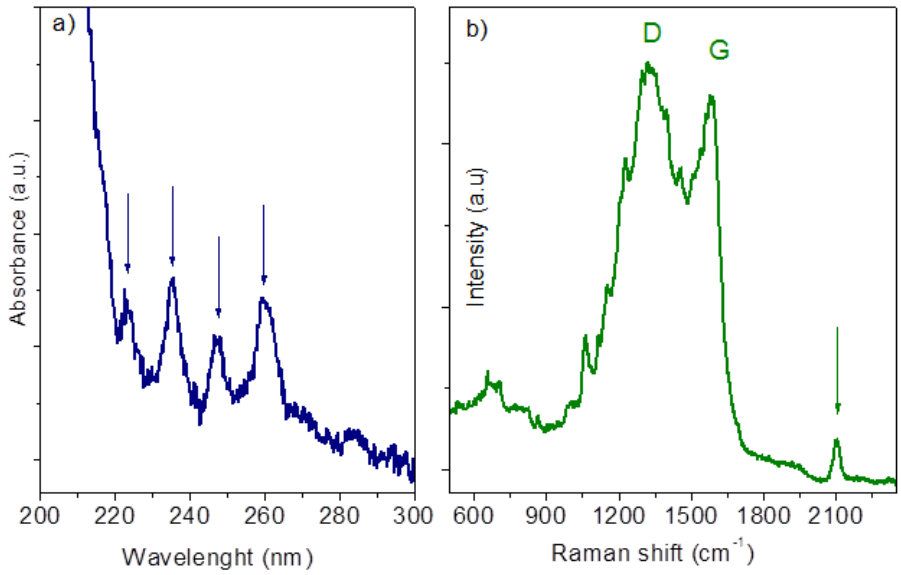

Figure 3-43: a) Absorption spectrum of the solution obtained after fs-ablation of HOPG in N_2; b) SERS of the solution.

The samples were then characterized by means of a Raman spectroscopy. Generally, the Raman signals of polyynes are very weak, therefore we employed the surface enhanced Raman spectroscopy (SERS) technique (229; 230). This is known to increase the Raman signals from molecules that are attached to metallic nanostructures. In the present work, for the SERS characterization, some drops of a silver nanoparticles solution were first deposited onto a glass substrate. The Raman spectrum shown in Figure 3-43(b) was then collected after dripping a drop of solution onto silver colloid film. The spectrum displayed in Figure 3-43(b), shows the presence of a band at 2100 cm^{-1}, that can be attributed to the presence of polyynes. Indeed, Raman bands located around 1800-2100 $cm^{-1}$are related to sp-hybridized linear carbon chains of different lengths (231; 232). The band found at 2100 cm^{-1} suggests the presence of polyynes with eight carbon atoms per chain (229), in accordance with the UV-VIS results. Between 1200-1600 cm^{-1} the D and G peaks, rising from the vibrations of sp^2 carbon atoms, are visible. The shape of these peaks suggests that the material analyzed consisted of disordered graphite and other carbon nanostructures (233; 234). It should be noted that, even if the fs-laser ablation is

performed in N_2, some water molecules could be still present due to the adsorbed water so that some hydrogen is always present. Spectral peaks at frequencies of ~ 657, 707, and 866 cm^{-1} can be attributed to the out- of-plane (oop) bending modes of CH groups in polycyclic aromatic hydrocarbon (PAH) molecules (235; 236). It has been reported that the energies of these oop vibrations depends on the number of adjacent CH groups (235). In particular, the observed signals at 707 and 866 cm^{-1} can be attributed to quintet and duo groups (237) respectively, while the peak at ~650 cm^{-1} can be assigned to the oop vibrations of benzene (237). The presence of these molecules can attributed to the crosslinking of the polyynes into PAHs (238), as it is known and accepted that polyynes can be precursors to PAH formation (239).

Conclusions

During my PhD course, my research topic was the synthesis and characterization of carbon-based nanomaterials. The first year I focused my attention on the synthesis of graphene employing the mechanical exfoliation of graphite. Moreover, the strain effects induced by the deposition process of the graphene sheets onto suitable substrates were studied. The second year, it was developed a new bottom up approach for the synthesis of graphene-like nanostructures: the graphene nanowalls (GNWs). These systems are commonly obtained employing expensive techniques such as CVD, but here it has been demonstrated that GNWs can be obtained in a cheaper and environmental friendly way just using laser ablation of a graphite target in water and by applying an electric field. In particular, the laser ablation leads to the synthesis of stable solutions of polyynes, which are the responsible for the growth of carbon nanowalls once the electric field is applied. During the third and last year of my PhD, I studied the effects of ablation of a graphite target either with a nanosecond or a femtosecond laser, in liquids. In particular, I carried out my studies and experiments at the University of Catania and at

the University of Waterloo (Canada) at the Department of Mechanical and Mechatronics Engineering, in the Centre for Advanced Materials Joining (CAMJ). It was found that the laser ablation of graphite can lead to the synthesis of large graphene domains employing the nanosecond laser, while the use of a femtosecond laser produces large amounts of porous graphene sheets, that are recovered at the water-air interface and the graphene quantum dots that are dispersed in the liquid. These materials, the porous graphene and graphene quantum dots, are attracting the interest of all the scientific community due to their potential applications in many fields such as energy storage and water treatment, respectively.

Bibliography

1. **T.D. Burchell.** *Carbon Materials for Advanced Technologies.* s.l. : Amsterdam; Ney York: Pergamon/Elsevier Science, 1999. p. 540.

2. *C60: Buckminsterfullerene.* **H.W. Kroto, J.R. Heath, S.C. O' Brien, R.F. Curl, R.E. Smalley.** 1985, Nature, Vol. 318, pp. 162-163.

3. *Solid C60: a new form of carbon.* **W. Kratschmer, L.D. Lamb, K. Fostiropoulos, and D.R. Huffman,.** 1990, Nature, Vol. 347, pp. 354-358.

4. *Fullerenes, nanotubes, onions and related carbon structures.* **C.N.R. Rao, R. Seshadri, A. Govindaraj, R. Sen.** 6, 1995, Materials Science and Engineering: R: Reports, Vol. 15, pp. 209-262.

5. *Graphene quantum dots: an emerging material for energy-related applications and beyond.* **Z. Zhang, J. Zhang, N. Chen and L. Qu.** 2012, Energy Environ. Sci, Vol. 5, pp. 8869-8890.

6. *Luminscent Graphene Quantum Dots for Organic Photovoltaic Devices.* **G. Vinay, C. Neeraj, S. Ritu, D. S. Gauri, B. Ramil and C. Suresh.** 26, 2011, J. Am. Chem. Soc, Vol. 133, pp. 9960-9963.

7. *Quantum Dots for Live Cells, in Vivo Imaging, and Diagnostics.* **X. Michalet, F.F. Pinaud, L.A. Bentolila, J.M. Tsay, S. Doose, J.J. Li, G. Sundaresan, A.M. Wu, S.S. Gambhir and S. Weiss.** 5709, 2005, Science, Vol. 307, pp. 538-544.

8. *Chaotic Dirac Billiard in Graphene Quantum Dots.* **L.A. Ponomarenko, F. Schedin, M.I. Katsnelson, R. Yang, E.W. Hill, K.S. Novoselov and A.K. Geim.** 5874, 2008, Science, Vol. 320, pp. 356-358.

9. *Helical microtubules of graphitic carbon.* **S. Iijima.** 1991, Nature, Vol. 354, pp. 56-58.

10. *Carbon nanotubes and their emission properties.* **A.V. Eletskii.** 2002, Physics-Uspekhi, Vol. 45, pp. 369-402.

11. *Atomic structure and electronic properties of single-walled carbon nanotubes.* **T.W. Odom, J.-L. Huang, P. Kim, C.M. Lieber.** 1998, Nature, Vol. 391, pp. 62-64.

12. *Decoration of carbon nanotubes.* **T.W. Ebbesen, H. Hiura, M.E. Bisher, M.M.J. Treacy, J.L. Shreeve-Keyer, R.C. Haushalter.** 1996, Advanced Materials, Vol. 8, pp. 155-157.

13. *Functionalization of carbon nanotubes.* **H. Kuzmany, A. Kukovecz, F. Simona, M. Holzweber, Ch. Kramberger, T. Pichler.** 2004, Synthetic Metals, Vol. 141, pp. 113-122.

14. **S. Yahachi.** *Carbon Nanotube and Related Field Emitters.* s.l. : Wiley-VCH, 2010. p. 479. ISBN: 978-3-527-32734-8.

15. *Density of states reflects diameter in nanotubes.* **C.T White, and J.W. Mintmire,.** 1998, Nature, Vol. 394, p. 29.

16. *A new form of carbon from the Ries crater.* **A.E. Goresy, and G.T. Donnay.** 1968, Science, Vol. 161, pp. 363-364.

17. *Carbon: observations on the new allotropic form.* **G.A. Whittaker, and P.L. Kintner,.** 1969, Science, Vol. 165, pp. 589-591.

18. *Carbon: A suggested new hexagonal crystal form.* **G.A. Whittaker, and G.M. Wolten,.** 1972, Vol. 178, pp. 54-54-56.

19. *Crystalline forms of a linear modification of carbon.* **V.I. Kasatochkin, A.M. Sladkov, Y.P. Kudryatsev, N.M. Popov, and V.V Korshak,.** 1967, Dokl. Chem (Engl Transl), Vol. 177, p. 1031.

20. *On crystalline structure of carbyne.* **V.I. Kasatochkin, V.V Korshak, Y.P. Kudryatsev, A.M. Sladkov, and L.E. Sterenberg,.** 1973, Vol. 11, pp. 70-72.

21. **R.B. Heimann, S.E. Evsyukov, L. Kavan.** *Carbyne and Cabynoid Structures.* [ed.] Robert B. Heimann, Sergey E. Evsyukov and Ladislav Kavan. s.l. : Kluwer Academic Publishers, 1999. p. 444. ISBN:0-7923-5323-4.

22. *Electrochemical Carbon.* **L. Kavan.** 1997, Chem. Rev., Vol. 97, pp. 3061-3082.

23. *Carbon in the Universe.* **T. Henning, F. Salama.** 1998, Science, Vol. 282, pp. 2204-2210.

24. *Synthesis of Linear Acetylenic Carbon: The "sp" Carbon Allotrope.* **R.J. Lagow, J.J. Kampa, H.C. Wei, S.L. Battle, J.W. Genge, D.A. Laude, C.J. Harper, R. Bau, R.C. Stevens, J.F. Haw, E. Munson.** 1995, Science, Vol. 267, pp. 362-367.

25. *Microwave and laser spectroscopy of carbon chains and rings.* **M.C. McCarthy, P. Thaddeus.** 2001, Chem. Soc. Rev., Vol. 30, pp. 177-185.

26. **Y.P. Kudryavtsev, S. Evysyukov, M. Guseva, V. Babaev, and V. Khvostov,.** Carbyne- A linear chainlike carbon allotrope. [book auth.] Peter A. Thrower. *Chemistry and Physics of Carbon.* s.l. : Marcel Dekker, Inc., 1965-, Vol. 25, 1.

27. *Electric Field Effect in Atomically Thin Carbon Films.* **A.K. Geim, K. Novoselov, S.V. Morozov, D. Jiang, Y. Zhang, S.V. Dubonos, I.V. Grigorieva and A.A. Firsov.** 2004, Science, Vol. 306, pp. 666-669.

28. *Production of petal-like graphite sheets by hydrogen arc discharge.* **Y. Ando, X. Zhao, M. Ohkohchi.** 1997, Carbon, Vol. 35, pp. 123-158.

29. *Carbon nanowalls grown by microwave plasma enhanced chemical vapor deposition.* **Y. Wu, P. Qiao, T. Chong, Z. Shen.** 2002, Advanced MAterials, Vol. 14, pp. 64-67.

30. *Fabrication of a freestanding boron nitride single layer and its defect assignments.* **C. Jin, F. Lin, K. Suenaga and S. Iijima.** 2009, Phys. Rev. Lett., Vol. 102, pp. 195505-4.

31. *N-Doping of graphene through electrothermal reactions with ammonia.* **X. Wang, X. Li, L. Zhang, Y. Yoon, P.K. Weber, H. Wang, J. Guo, H. Dai.** 2009, Science, Vol. 324, pp. 768-771.

32. *Nitrogen-doped graphene and its electrochemical applications.* **Y. Shao, S. Zhang, M. H. Engelhard, G. Li, G. Shao, Y. Wang, J. Liu, I. A. Aksay and Y. Lin.** 2010, J. Mater. Chem., Vol. 20, pp. 7491-7496.

33. *Transparent, Conductive Graphene Electrodes for Dye-Sensitized Solar Cells.* **X. Wang, L. Zhi, and K. Müllen.** 2008, Nano Lett., Vol. 8, pp. 323-327.

34. *Roll-to-roll production of 30-inch graphene films for transparent electrodes.* **S. Bae, H. Kim, Y. Lee, X. Xu, J.-S. Park, Y. Zheng, J. Balakrishnan, T. Lei, H.R. Kim, Y.II Song, Y.-J. Kim, K.S. Kim,B. Ozyilmaz, J.-H. Ahn, B.H. Hong, and S. Iijima.** 2010, Nanotech., Vol. 5, pp. 574-578.

35. *Uniform and enhanced field emission from chromium oxide coated carbon nanosheets.* **K. Hou, R.A. Outlaw, S. Wang, M. Zhu, R.A. Quinlan, D.M. Manos, M.E. Kordesch, U. Arp, and B.C. Halloway.** 13, 2008, App. Phys. Lett., Vol. 92, p. 133112.

36. *Possibilities for graphene for field emission: modeling studies using the BEM.* **S. Watcharotone, R.S. Ruoff,and F.H. Read.** 2008, Physics Procedia, Vol. 1, pp. 71-75.

37. *Selective Molecular Sieving Through Porous Graphene.* **S. P. Koenig, L. Wang, J. Pellegrino, and J.S. Bunch.** 2012, Nat. Nanotech., Vol. 7, pp. 728-732.

38. *Porous Graphene As the Ultimate Membrane for Gas Separation.* **D. Jiang, V.R. Cooper, and S. Dai.** 2009, Nano Lett., Vol. 9, pp. 4019-4024.

39. *Facile Preparation of Ordered Porous Graphene–Metal Oxide@C Binder-Free Electrodes with High Li Storage Performance.* **J. Zhu, D. Yang, X. Rui, D. Sim, H. Yu, H. E. Hoster, P. M. Ajayan, Q. Yan.** 2013, Small. http://dx.doi.org/10.1002/smll.201300755.

40. *Multifunctional Porous Graphene for Nanoelectronicsand Hydrogen Storage:New Properties Revealed by First Principle Calculations.* **A. Du, Z. Zhu, and S.C Smith.** 2010, J. Am. Chem. Soc, Vol. 132, pp. 2876–2877.

41. *Graphene Nanomesh.* **J. Bai, X. Zhong, S. Jiang, Y. Huang and X. Duan.** 2010, Nat. Nanotech., Vol. 5, pp. 190-194.

42. *Upconversion and Downconversion Fluorescent Graphene Quantum Dots: Ultrasonic Preparation and Photocatalysis.* **S. Zhuo, M. Shao, and S.T. Lee.** 2012, ACS Nano, Vol. 6, pp. 1059-1064.

43. **B.P. Chauhan.** *Hybrid Nanometrials.* s.l. : Wiley and Sons, Inc., 2011.

44. *Possibility of Hybrids Materials.* **A. Makisima.** 2004, Caramic Japan, Vol. 39, pp. 90-91.

45. *Designing Hybrid Materials.* **M.F. Ashby, and Y.J.M. Bréchet.** 2003, Acta Mater., Vol. 51, pp. 5801-5821.

46. *Fracture Mechanics.* **Y. Hagiwara, H. Suzuki.** Tokyo, Japan : s.n., 2000, pp. 135-138.

47. *Fullerene-multiwalled carbon nanotube complexes for bulk heterojunction photovoltaic cells.* **C. Li, Y. Chen, S. Ntim, S. Mitra.** 2010, Applied Physics Letters, Vol. 96, pp. 143303-5.

48. *Selective host-guest interaction of single-walled carbon nanotubes with functionalised fullerenes.* **D.A. Britz, A.N. Khlobystov, J. Wang, A.S. O'Neil, M. Poliakoff, A. Ardavan, G.A.D. Briggs.** 2004, Chemical Communications, pp. 176-177.

49. *Low temperature assembly of fullerene arrays in single-walled carbon nanotubes using supercritical fluids.* **A.N. Khlobystov, D.A. Britz, J. Wang, S.A. O'Neil, M. Poliakoff, G.A.D. Briggs.** 2004, Journal of Materials Chemistry, Vol. 14, pp. 2852-2857.

50. *Controlled synthesis of carbon nanotubes and linear C chains by arc discharge in liquid nitrogen.* **S. Scalese, V. Scuderi, S. Bagiante, F. Simone, P. Russo, L. D'Urso, G. Compagnini, V. Privitera.** 2010, Journal of Applied Physics, Vol. 107, pp. 014304-6.

51. *Surface-enhanced Raman scattering study on 1D-2D graphene-based structures.* **L. D'Urso, G. Forte, P. Russo, C. Caccamo, G. Compagnini, O. Puglisi.** 2011, CArbon, Vol. 49, pp. 3149-3157.

52. *Encapsulated C60 in carbon nanotubes.* **B.W. Smith, Marc Monthioux and D.E. luzzi.** 1998, Nature, Vol. 396, pp. 323-324.

53. **F. Simon, and M. Monthioux,.** *Fullerenes inside Carbon Nanotubes: The Peapods, in Carbon Meta-Nanotubes: Synthesis, Properties and Applications.* [ed.] M. Monthioux. Chichester : John Wiley & Sons, Ltd, 2011.

54. *Vertically aligned peapod formation of position-controlled multi-walled carbon nanotubes (MWNTs).* **D. Kondo, A. Kawabata, M. Horibe, M. Nihei and Y Awano.** 2003, Supperlatt. Microstruct., Vol. 34, pp. 389-394.

55. *Insertion of C60 into multi-wall carbon nanotubes – a synthesis of C60@MWCNT.* **T. Frohlich, P. Scharff, W. Schliefke, H. Romanus, V. Gupta, C. Siegmund, O. Ambacher and L. Spiess.** 2004, Carbon, Vol. 42, pp. 2759-2762.

56. *Packing C60 in boron nitride nanotubes.* **W. Mickelson, S. Aloni, W.Q. Han, J. Cumings and A. Zettl.** 2003, Science, Vol. 300, pp. 467-469.

57. **M.S. Dresselhaus, G. Dresselhaus and P.C. Ecklund.** *Science of fullerenes and carbon nanotubes.* New York : Academic Press, 1996.

58. *One-dimensional metallofullerene crystal generated inside single-walled carbon nanotubes.* **K. Hirahara, K. Suenaga, S. Bandow, H. Kato, T. Okazaki, T. Shinohara and S. Iijima.** 2000, Phys.Rev. Lett., Vol. 85, pp. 5384-5387.

59. *Tumbling atoms and evidence for charge transfer in La–2@C80@SWNT.* **B.W. Smith, D.E. Luzzi and Y. Achiba.** 2000, Chem. Phys. Lett., Vol. 331, pp. 137-142.

60. *Observation of atom-like nitrogen in nitrogen-implanted solid C60.* **T. Almeida Murphy, T. Pawlik, A. Weidinger, M. Hhne, R. Alcala and J.-M. Spaeth.** 1996, Phys. Rev. Lett., Vol. 77, pp. 1075-1078.

61. *Selective host-guest interaction of single-walled carbon nanotubes with functionalized fullerenes.* **D.A. Britz, A.N. Khlobystov, J.W. Wang, A.S. O'Neil, M. Poliakoff, A. Ardavan and G.A. Briggs.** 2, 2004, Chemm. Comm, pp. 176-177.

62. *Encapsulating C59N azafullerene derivatives inside single-wall carbon nanotubes.* **F. Simon, H. Kuzmany, J. Bernardi, F. Hauke and A. Hirsch.** 2006, Carbon, Vol. 44, pp. 1958-1962.

63. *Magnetic fullerenes inside single-wall carbon nanotubes.* **F. Simon, H. Kuzmany, B. Nafradi, T. Fehér, L. Forro, F. Fülöp, A. Janossy, A. Rockenbauer,L. Korecz, F. Hauke and A. Hirsch,.** 2006, Phys. Rev. Lett., Vol. 97, p. 136801.1/4.

64. *Isotope engineering of carbon nanotube systems.* **F. Simon, C. Kramberger, R. Pfeiffer, H. Kuzmany, V. Zolyomi, J. Kürti, P.M. Singer and H. Alloul.** 2005, Phys. Rev. Lett., Vol. 95, p. 017401.1/4.

65. *Nanotube 'Peapods' show electrifying promise.* **R.F. Service.** 2001, Science, New Series, Vol. 292, p. 45.

66. *Photoinduced electron transfer in C60 encapsulated single-walled carbon nanotube.* **Y.F. Li, T. Kaneko and R. Hatakeyama.** (2008)., Appl. Phys. Lett., Vol. 92, pp. 183115/1–3.

67. *Carbon Nanowire Made of a Long Linear Carbon Chain Inserted Inside a Multiwalled Carbon Nanotube.* **X. Zhao, Y. Ando, Y. Liu, M. Jinno and T. Suzuki.** 18, 2003, Phys. Rev. Lett., Vol. 90, pp. 187401-4.

68. *Single-wall carbon nanotubes encaging linear chain C10H2 polyyne molecules inside.* **D. Nishide, H. Dohi, T. Wakabayashi, E. Nishibori, S. Aoyagi, M. Ishida, S. Kikuchi, R. Kitaura, T. Sugai, M. Sakata, H. Shinohara.** 2006, Chemical Physics Letters, Vol. 428, pp. 356-360.

69. *Reductive Preparation of Carbyne with High Yield. An in Situ Raman Scattering Study.* **J. Kastner, H. Kuzmany, L. Kavan, F. P. Dousek and J. Kurti.** 1995, Macromolecules, Vol. 28, pp. 344-353.

70. *Raman and SERS investigation of isolated sp carbon chains.* **A. Lucotti, M. Tommasini, M. Del Zoppo, C. Castiglioni, G. Zerbi, F. Cataldo, C.S. Casari, A. Li Bassi, V. Russo, M.**

Bogana, C.E. Bottani. 2006, Chem. Phys. Lett., Vol. 417, pp. 78–82.

71. *Can graphene be used as a substrate for Raman enhancement?* **X. Ling, L. Xie, Y. Fang, H. Xu, H. Zhang, J. Kong.** 2010, Nano Lett, Vol. 10, pp. 553-561.

72. *Graphene-enhanced Raman imaging of TiO2 nanoparticles.* **D. Naumenko, V. Snitka, B. Snopok, S. Arpiainen and H. Lipsanen.** 2012, Nanotechnology, Vol. 23, pp. 465703-465709.

73. *Nanoscale and edge effect on electronic properties of graphene.* **K. Wakabayashi, S. Dutta.** 2012, Solid State Communications, Vol. 152, pp. 1420-1430.

74. *The electronic properties of graphene.* **A.H. Castro Neto, F. Guinea, N.M.R. Peres, K.S. Novoselov and A.K. Geim.** 1, 2009, Rev. Mod. Phys., Vol. 81, pp. 109-162 .

75. **W. Choi, J-w. Lee.** *Graphene: Synthesis and apllications.* s.l. : CRC Press, Taylor & Francis group, 2012. ISBN: 978-1-4398-6187-5.

76. **M. Di Ventra, S. Evoy, and J.E. Hughes Jr.** *Introduction to Nanoscale Science and Technology* . Berlin : Springer, 2004. ISBN: 1-4020-7720-3.

77. *Nanoelectromechanical systems.* **H.G. Craighead.** 2000, Science, Vol. 290, pp. 1532-1535.

78. *Experimental Review of Graphene.* **D.R. Cooper, B. D'Anjou, N. Ghattamaneni, B. Harack, M. Hilke, A. Horth, N. Majlis,M. Massicotte, L. Vandsburge, E. Whiteway and V. Yu.** 2011, ISRN Condensed Matter Physics, Vol. 2012, pp. 1-56.

79. *Mechanical properties of suspended graphene sheets.* **I.W. Frank, D.M. Tanenbaum, A.M. Van der Zande, and P.L. McEuen.** 6, 2007, J. Vac. Sci. Techno.l B, Vol. 25, pp. 2558-2561.

80. *Measurement of the elastic properties and intrinsic strength of monolayer graphene.* **C. Lee, X. Wei, J.W. Kysar, and J. Hone,.** 5887, 2008, Science, Vol. 321, pp. 385-388.

81. *Transparent, flexible, low-temperature, and solution-processible graphene composite electrode.* **H. Chang, G. Wang, A. Yang, X. Tao, X. Liu, Y. Shen, and Z. Zheng.** 2010, Adv. Funct. Mater., Vol. 20, pp. 2893–2902.

82. *Graphene-based electrochemical sensors and biosensors: a review.* **Y. Shao, J. Wang, H. Wu, J. Liu, I.A. Aksay, and Y. Lin.** 2010, Electroanalysis, Vol. 22, pp. 1027-1036.

83. *Fabrication and electric-field-dependent transport measurements of mesoscopic graphite devices.* **Y. Zhang, J.P. Small, W.V. Pontius, and P. Kim.** 2005, Appl. Phys. Lett., Vol. 86, pp. 073104-6.

84. *The two-dimensional phase of boron nitride: Few-atomic-layer sheets and suspended membranes.* **D. Pacilé, J.C. Meyer, Ç.Ö. Girit, and A. Zettl.** 2008, Appl. Phys. Lett., Vol. 92, pp. 133107-09.

85. *Frictional characteristics of atomically thin sheets.* **C. Lee, Q. Li, W. Kalb, X-Z. Liu, H. Berger, R.W. Carpick, and James Hone.** 2010, Science, Vol. 328, pp. 76-79.

86. **M. Inagaki, F. Kang, M. Toyoda.** Exfoliation of Graphite via Intercalation Compounds. [book auth.] L.R. Radovic. *Chemistry and Physics of Carbon.* s.l. : Marcel Dekker, 2004, Vol. 29.

87. *A Chemical Route to Carbon Nanoscrolls.* **L.M. Viculis, J.J. Mack, R.B. Kaner.** 5611, 2003, Science, Vol. 299, p. 1361.

88. *High-yield production of graphene by liquid-phase exfoliation of graphite.* **Y. Hernandez, V. Nicolosi, M. Lotya, F.M. Blighe, Z. Sun, S. De, I.T. Mcgovern, B. Holland, M. Byrne, Y.K. Gun'ko, J.J. Boland, P. Niraj, G. Duesberg, S. Krishnamurthy, R. Goodhue, J. Hutchison, V. Scardaci,**

A.C. Ferrari, and J.N. Coleman. 2008, Nature Nanotechnology, Vol. 3, pp. 563-568.

89. *Theory for the ultrafast ablation of graphite films.* **H.O. Jeschke, M.E. Garcia, and K.H. Bennemann.** 1, 2001, Phys. Rev. Lett., Vol. 87, pp. 015003-4.

90. *Structural preablation dynamics of graphite observed by ultrafast electron crysallography.* **F. Carbone, P. Baum, P. Rudolf, and A.H. Zewail.** 2008, Phy. Rev. Lett., Vol. 100, pp. 035501-4.

91. *Photoexfoliation of graphene from graphite: An ab initio study.* **Y. Miyamoto, H. Zhang, and David Tomanek.** 2010, Phys. Rev. Lett., Vol. 104, pp. 208302-4.

92. *Formation of graphene sheets through laser exfoliation of highly ordered pyrolytic graphite.* **M. Qian, Y.S. Zhou, Y. Gao, J.B. Park, T. Feng, S.M. Huang, Z. Sun, L. Jiang, and Y.F. Lu.** 2011, Appl. Phys. Lett., Vol. 98, pp. 173108-3.

93. *Laser assisted green synthesis of free standing reduced graphene oxides at the water–air interface.* **G. Compagnini, P. Russo, F. Tomarchio, O. Puglisi, L. D'Urso, and S. Scalese.** 2012, Nanotech, Vol. 23, pp. 505601-6.

94. *Laser ablation of metals: a new method for preparing SERS active colloids.* **J. Neddersen, G. Chumanov, T.M. Cotton.** 1993, Applied Spectroscopy, Vol. 47, pp. 1959-1964.

95. *Formation of Stable Platinum Nanoparticles by Laser Ablation in Water.* **F. Mafune, J.Y. Kohno, Y. Takeda, and T. Kondow.** 2003, J. Phys. Chem. B, Vol. 107, pp. 4218–4223.

96. *Laser Ablation Synthesis in Solution and Size Manipulation of Noble Metal Nanoparticles.* **V. Amendola, and M. Meneghetti.** 2009, Phys. Chem. Chem. Phys., Vol. 11, pp. 3805–382.

97. *Preparation of Nanocrystalline Diamonds Using Pulsed Laser Induced Reactive Quenching.* **G.W. Yang, J.B Wang, and Q.X. Liu.** 1998, J. Phys. , Vol. 10, pp. 7923–7927.

98. *Preparation of Graphitic Oxide.* **W.S. Hummers Jr., and R.E. Offeman.** 6, 1958, J. Am. Chem. Soc., Vol. 80, pp. 1339–1339.

99. *High-throughput solution processing of large-scale graphene.* **V.C. Tung, M.J. Allen, Y. Yang, and R.B. Kaner.** 2009, Nature Nanotechnology, Vol. 4, pp. 25-29.

100. *Langmuir-Blodgett Assembly of Graphite Oxide Single Layers.* **L.J. Cote, F. Kim, and J. Huang.** 2009, J. Am. Chem. Soc. , Vol. 131, pp. 1043–1049.

101. *Visibility of graphene flakes on a dielectric substrate.* **D.S.L. Abergel, A. Russell, and V.I. Falko.** 6, 2007, Appl. Phys. Lett., Vol. 91, pp. 063125-3.

102. *Simple Approach for High-Contrast Optical Imaging and Characterization of Graphene-Based Sheets.* **I. Jung, M. Pelton, R. Piner, D.A. Dikin, S. Stankovich, S. Watcharotone, M. Hausner, and R.S. Ruoff.** 12, 2007, Nano Lett., Vol. 7, pp. 3569–3575.

103. *Making graphene visible.* **P. Blake, E. Hill, A.H.C. Neto, K.S. Novoselov, D. Jiang, R. Yang, T.J. Booth, and A.K. Geim.** 6, 2007, Appl Phys Lett, Vol. 91, pp. 063124-3.

104. *Determination of the Number of Graphene Layers: Discrete Distribution of the Secondary Electron Intensity Stemming from Individual Graphene Layers.* **H. Hiura, H. Miyazaki, and K. Tsukagoshi.** 2010, Appl. Phys. Exp., Vol. 3, pp. 095101-3.

105. *Two-dimensional atomic crystals.* **K.S. Novoselov, D. Jiang, F. Schedin, T.J. Booth, V.V. Khotkevich, S.V. Morozov, and A.K. Geim.** 2005, PNAS, Vol. 102, pp. 10451–10453.

106. *Raman Spectrum of Graphene and Graphene Layers.* **A.C. Ferrari, J.C. Meyer, V. Scardaci, C. Casiraghi, M. Lazzeri,**

F. Mauri, S. Piscanec, D. Jiang, K.S. Novoselov, S. Roth, and A.K. Geim. 2006, Phys. Rev. Lett, Vol. 97, pp. 187401-4.

107. *Nanostructured molecular surfaces: advances in investigation and patterning tools.* **Pignataro, B.** 2009, J. Mater. Chem, Vol. 19, p. 3338.

108. *Raman spectroscopy in graphene.* **L.M. Malard, M.A. Pimenta, G. Dresselhaus, and M.S. Dresselhaus.** 2009, Physics Reports, Vol. 473, pp. 51-87.

109. *Probing Strain-Induced Electronic Structure Change in Graphene by Raman Spectroscopy.* **M. Huang, H. Yan, T. F. Heinz, and J. Hone.** 2010, Nano Lett., Vol. 10, pp. 4074–4079.

110. *Atomic Correlation Between Adjacent Graphene Layers in Double-Wall Carbon Nanotubes.* **A. Hashimoto, K. Suenaga, K. Urita, T. Shimada, T. Sugai, S. Bandow, H. I. Shinohara, and S. Iijima.** 2005, Phys. Rev. Lett. , Vol. 94, p. 045504 .

111. *Raman 2D-band splitting in graphene: theory and experiment.* **O. Frank, M. Mohr, J. Maultzsch, C. Thomsen, I. Riaz, R. Jalil, K.S. Novoselov, G. Tsoukleri, J. Parthenios, K. Papagelis, L. Kavan and C. Galiotis.** 2011, ACS Nano, Vol. 5, pp. 2231223-9.

112. *Raman Monitoring of Strain Induced Effects in Mechanically Deposited Single Layer Graphene.* **P. Russo, G. Compagnini, C. Musumeci, B. Pignataro.** 2012, J. Nanosci. Nanotechnol., Vol. 12, pp. 8755–8758.

113. *Short polyyne chains produced by pulsed laser ablation of graphite in water.* **G. Compagnini, V. Mita, R.S. Cataliotti, L. D'Urso,O. Puglisi.** 2007, Carbon, Vol. 45, pp. 2456–2458.

114. *An Electrochemical Avenue to Blue Luminescent Nanocrystals from Multiwalled Carbon Nanotubes (MWCNTs).* **J. Zhou, C. Booker, R. Li, X. Zhou, T. –K, Sham, X. Sun, and Z. Ding.** 2007, J. Am. Chem. Soc. , Vol. 129, pp. 744-745.

115. *Lossless Synthesis of Tiny CdS Quantum Dots-decorated Graphene Nanosheets with Large Nonlinear Optical Properties.* **M. Feng, R. Sun, H. Zhan, and Y. Chen.** 2010, Nanotechnol., Vol. 21, pp. 075601-7.

116. *Graphene nanosheets for enhanced lithium storage in lithium ion batteries.* **G. Wang, X. Shen, J. Yao, and J. Park.** 2009, Carbon, Vol. 47 , pp. 2049-2053.

117. *Graphene oxide papers modified by divalent ions—enhancing mechanical properties via chemical cross-linking.* **S. Park, S. LeeK, G. Bozoklu, W. Cai, S.T. Nguyen and R.S. Ruoff.** 2008, ACS Nano, Vol. 2, pp. 572–578.

118. *Chemical analysis of graphene oxide films after heat and chemical treatments by x-ray photoelectron and micro-Raman spectroscopy.* **D. Yang, A. Velamakanni, G. Bozoklu, S. Park, M. Stoller, R. D. Piner, S. Stankovich, I. Jung, D. A. Field, C. A. Ventrice Jr.and R. S. Ruoff.** 2009, Carbon, Vol. 47, pp. 145–152.

119. *Electron emission from nanostructured carbon composite materials - an important role of the interface for enhancing the emission..* **H. Hiraki, N. Jiang, H.X. Wang, and A. Hiraki.** 2006, Journal Physics IV, Vol. 132, pp. 111-115.

120. *Origin of field emission from a nano-diamond/carbon nanowall electron emitter.* **G. Takyo, S. Kono, T. Goto, H. Sasaoka, and K. Nishimura.** 2008, Jpn J Appl Phys, Vol. 47, pp. 2241-2243.

121. *Enhanced electrocatalytic activity of Pt subnanoclusters on graphene nanosheet surface.* **E. Yoo, T. Okata, T. Akita, M. Kohyama, J. Nakamura, I. Honma.** 2009, Nano Lett., Vol. 9, pp. 2255-2259.

122. **M. Hiramatsu, M. Hori.** *Carbon Nanowalls: Synthesis and Emerging Applications.* s.l. : Springer, 2010. p. 161. 3211997172.

123. *Vertical growth of carbon nanowalls using rf plasma-enhanced chemical vapor deposition.* **K. Shiji, M. Hiramatsu, A. Enomoto, M. Nakamura, H. Amano, M. Hori.** 2005, Diamond and Related Materials, Vol. 14, pp. 831-834.

124. *Fabrication of vertically aligned carbon nanowalls using capacitively coupled plasma-enhanced chemical vapor deposition assisted by hydrogen radical injection.* **M. Hiramatsu, K. Shiji, H. Amano, and M. Hori.** 2004, Appl. Phys. Lett., Vol. 84, pp. 4708-4710.

125. *Uniform carbon nanoflake films and their field emissions.* **N.G. Shang, F.C.K. Au, X.M. Meng, C.S. Lee, I. Bello, S.T. Lee.** 2002, Chem. Phys. Lett., Vol. 358, pp. 187-191.

126. *Preparation and electron field emission of carbon nanowall by Cat-CVD.* **T. Itoh, S. Shimabukuro, S. Kawamura, and S. Nonomura.** 2006, Thin Solid Films, Vol. 501, pp. 314-317.

127. *Freestanding carbon nanowalls by microwave plasma-enhanced chemical vapour deposition.* **A. T. H. Chuang, B. O. Boskovic, J. Robertson.** 2006, Diamond and Related Materials, Vol. 15, pp. 1103–1106.

128. *Fabrication of carbon nanowalls using electron beam excited plasma-enhanced chemical vapor deposition .* **T. Mori,**

M. Hiramatsu, K. Yamakawa, K. Takeda, M. Hori. 2008, Diamond and Related Materials, Vol. 17, pp. 1513-1517.

129. *Carbon nanowalls growth by radiofrequency plasma-beam-enhanced chemical vapor deposition.* **S. Vizireanu, L. Nistor, M. Haupt, V. Katzenmaier, C. Oehr, G. Dinescu.** 2008, Plasma Processes and Polymers, Vol. 5, pp. 263–268.

130. *Free-standing subnanometer graphite sheets.* **J. J. Wang, M. Y. Zhu, R. A. Outlaw et al.** 2004, Appl. Phys. Lett., Vol. 85, pp. 1265–1267.

131. *Lithium insertion behavior of carbon nanowalls by dc plasma CVD and its heattreatment effect.* **O. Tanaike, N. Kitada, H. Yoshimura, H. Hatori, K. Kojima, M. Tachibana.** 2009, Solid State Ion, Vol. 180, pp. 381-385.

132. *Deposition of carbon nanowall flowers on two-dimensional sheet for electrochemical capacitor application.* **T.C. Hung, C.F. Chen, W.T. Whang.** 2009, Electrochem. Solid State Lett. , Vol. 12, pp. K41-K44.

133. *Electrochemical synthesis and characterization of magnetic nanoparticles on carbon nanowalls templates.* **B.J. Yang, Y.H. Wu, B.Y. Zong, Z.X. Shen.** 2002, Nano Letters, Vol. 2, pp. 751-754.

134. *Fabrication of a TiO2/carbon nanowalls heterojunction and its photocatalytic ability.* **H. Wang, X. Quan, H.T. Yu, S. Chen.** 2008, Carbon, Vol. 46, pp. 1126-1132.

135. *Fabrication of a class of nanostructured materials using carbon nanowalls as the templates.* **Y.H. Wu, B.J. Yang, G.C. Han, B.Y. Zong, H.Q. Ni, P. Luo, T.C. Chong, T.S. Low, Z.X. Shen.** 2002, Adv. Funct. Mater. , Vol. 12, pp. 489-494.

136. *Deposition of few layer graphene nanowalls at the electrodes during electric field-assisted laser ablation of carbon in water.* **G. Compagnini, M. Sinatra, P. Russo, G. Messina, O. Puglisi, S. Scalese.** 2012, Carbon , Vol. 50, pp. 2362-2365.

137. *Direct Synthesis of Sp-Bonded Carbon Chains on Graphite Surface by Femtosecond Laser Irradiation.* **A. Hu, M. Rybachuk, Q.-B. Lu, W.W. Duley.** 2007, Appl. Phys. Lett. , Vol. 91, pp. 131906-3.

138. *Spectroscopic Study of Polyynes Obtained by Laser Ablation in Liquids.* **G. Compagnini, V. Mita, L. D'Urso, R.S. Cataliotti, O. Puglisi.** 2008, J. Raman Spectrosc. , Vol. 39, pp. 177–181.

139. *Preparation of Polyynes by Laser Ablation of Graphite in Aqueous Media.* **S.K. Shin, J.K. Song, J. K, S.M. Park.** 2011, Applied Surface Science , Vol. 257, pp. 5156–5158.

140. *Direct Synthesis of Polyyne Molecules in Acetone by Dissociation Using Femtosecond Laser Irradiation.* **A. Hu, J. Sanderson, A.A. Zaidi, C. Wang, T. Zhang, Y. Zhou, W.W. Duley.** 2008, Carbon , Vol. 46, pp. 1823-1825.

141. *Preparation of Polyynes by the Laser Ablation of Graphite in Water and Organic Solvents.* **S.K. Shin, S.MK. Park.** 2012, Bull. Korean Chem. Soc., Vol. 33, pp. 597-600.

142. *Trapping high-pressure nanophase of Ge upon laser ablation in liquid.* **P. Liu, Y.L. Cao, X.Y. Chen, G.W. Yang.** 2009, Cryst. Growth. Des. , Vol. 9, pp. 1390-1393.

143. *Controllable Fabrication and Cathodoluminescence Performance of High-index Facets GeO2 Micro- and Nanocubes and Spindles upon Electrical-field-assisted Laser Ablation in Liquid.* **P. Liu, C. Wang, X. Chen, G. Yang.** 2008, J. Phys. Chem. C, Vol. 112, pp. 13450-13456.

144. *Synthesis of polyynes in a submerged electric arc in organic solvents.* **Cataldo, F.** 2004, Carbon, Vol. 42, pp. 129–142.

145. **M. Hiramatsu, M. Hori.** *Carbon Nanowalls: Synthesis and Emerging Applications.* s.l. : Springer, 2010. p. 161. 3211997172.

146. *Electrochemical Preparation of Hydrogen-Free Carbyne-like Materials.* **Kavan, L.** 1998, Carbon, Vol. 36, pp. 801-808.

147. *Control of pore structure in carbon.* **T. Kyotani.** 2000, Carbon, Vol. 38, pp. 269-286.

148. **C.R. Bansal, J.B. Donnet, F. Stoeckli.** *Active Carbon.* New York : Marcel Dekker, 1988.

149. *Impermeable atomic membranes from graphene sheets.* **J.S. Bunch, S.S Verbridge, J.S. Alden, A.M. van der Zande, J.M. Parpia, H.G. Craighead, P.L. McEuen.** 2008, Nano Lett., Vol. 8, pp. 2458–2462.

150. *Graphene nanostructures as tunable storage media for molecular hydrogen.* **S. Patchkovskii, J.S. Tse, S.N. Yurchenko, L. Zhechkov, T. Heine, G. Seifert.** 2005, Proc. Natl. Acad. Sci. , Vol. 102, pp. 10439-10444.

151. *Two-dimensional gas of massless Dirac fermions in graphene.* **K.S. KNovoselov, A.K. Geim, S.V. Morozov, D. Jiang, Katsnelson, M. I., et al.** 2005, Nature, Vol. 438, pp. 197–200.

152. *Porous raphene: Properties, preparation, and potential applications.* **P.T. Xu, J.X. Yang, K.S. Wang, Z. Zhou and P.W. Shen.** 23, 2012, Chinese Science Bullettin, Vol. 57, pp. 2948-2955.

153. *Porous graphenes: two-dimensional polymer synthesis with atomic precision.* **M. Bieri, M. Treier, J. Cai, K. Ait-Mansour, P. Ruffieux, O. Groning, P. Groning, M. Kastler, R. Rieger, X. Feng, K. Mullen, and R. Fasel.** 2009, Chem. Comm., Vol. 45, pp. 6919-6921.

154. *Two-dimensional polyphenylene: experimentally available porous graphene as a hydrogen purification membrane.* **Y. Li, Z. Zhou, P. Shena and Z. Chen.** 2010, Chem. Commun., Vol. 46, pp. 3672–3674.

155. *Mechanical properties of suspended graphene sheets.* **I.W. Frank, D.M. Tanenbaum, A.M. Van der Zande, and P.L. McEuen.** 2007, J. Vac. Sci. Technol. B, Vol. 25, pp. 2558-2561.

156. *Measurement of the elastic properties and intrinsic strength of monolayer graphene.* **C. Lee, X. Wei, J.W. Kysar, and J. Hone.** 2008, Science, Vol. 321, pp. 385-388.

157. *Superior thermal conductivity of single-layer graphene.* **A.A. Balandin, S. Ghosh, W. Bao, I. Calizo, D. Teweldebrhan, F. Miao and C.N. Lau.** 2008, Nano Letters, Vol. 8, pp. 902-907.

158. *Thermal conductivity of graphene in corbino membrane geometry.* **C. Faugeras, B. Faugeras, M. Orlita, M. Potemski,**

R. R. Nair and A. K. Geim. 2010, ACS Nano, Vol. 4, pp. 1889-1892.

159. *Thermal transport in suspended and supported monolayer graphene grown by chemical.* **W. Cai, A. L. Moore, Y. Zhu, X. Li, S. Chen, L. Shi and R. S. Ruoff.** 2010, Nano Lett., Vol. 10, pp. 1645-1651.

160. *Aerographite: ultra lightweight, flexible nanowall, carbon microtube material with outstanding mechanical performance.* **M. Mecklenburg, A. Schuchardt, Y. K. Mishra, S. Kaps, R. Adelung, A. Lotnyk, L. Kienle and K. Schulte.** 2012, Adv. Mater., Vol. 24, pp. 3486–3490.

161. *Preparation of activated graphene and effect of activation parameters on electrochemical capacitance.* **S. Murali, J. R. Potts, S. Stoller, J.o Park, M. D. Stoller, L. L. Zhang, Y. Zhu, R. S. Ruoff.** 2012, Carbon, Vol. 50, pp. 3482–3485.

162. *Easy synthesis of porous graphene nanosheets and their use in supercapacitors.* **Z. Fan, Q. Zhao, T. Li, J. Yan, Y. Ren, J. Feng and T. Wei.** 2012, Carbon, Vol. 50, pp. 1699-1703.

163. *Helium Separation Using Porous Graphene Membranes.* **J. Schrier.** 2010, J. Phys. Chem. Lett., Vol. 1, pp. 2284-2287.

164. *Porous Graphene as an Atmospheric Nanofilter.* **S. Blankenburg, M. Bieri, R. Fasel, K. Mullen, C. A. Pignedoli and D. Passerone.** 2010, Small, Vol. 6, pp. 2266-2271.

165. *Separation of Hydrogen and Nitrogen Gases with Porous Graphene.* **H. Du, J. Li, J. Zhang, G. Su, X. Li, and Y. Zhao.** 2011, J. Phys. Chem. C, Vol. 115, p. 23261.

166. *Hierarchically Porous Graphene as a Lithium-Air Battery Electrode.* **J. Xiao, D. Mei, X. Li, W. Xu, D. Wang, G. L. Graff, W. D. Bennett, Z. Nie, L. V. Saraf, I. A. Aksay, J. Liu and J.-G. Zhang,.** 2011, Nano Lett., Vol. 11, pp. 5071-5078.

167. *Advanced asymmetric supercapacitors based on Ni (OH) 2/graphene and porous graphene electrodes with high energy density.* **J. Yan, Z. Fan, W. Sun, G. Ning, T. Wei, Q. Zhang, R. Zhang, L. Zhi and F. Wei,.** 2012, Adv. Funct. Mater., Vol. 22, pp. 2232-2641.

168. *Band Ga Opening in Graphene Induced by Patterned Hydrogen Adsorption.* **R. Balog, B. Jørgensen, L. Nilsson, M. Andersen, E. Rienks, M. Bianchi, M. Fanetti,E. Lægsgaard, A. Baraldi, S. Lizzit, Z. Sljivancanin, F. Besenbacher, B. Hammer,Thomas G. Pedersen, P. Hofmann and L. Hornekaer.** 2010, Nat. Mater., Vol. 9, p. 315.

169. *Edgefunctionalized and substitutionally doped graphene nanoribbons: electronic and spin properties.* **F. Cervantes-Sodi, G. Csanyi, S. Piscanec, and A. C Ferrari.** 2008, Phys. Rev. B, Vol. 77, p. 165427 .

170. *Character of electronic states in graphene antidot lattices: flat bands and spatial localization.* **M. Vanevıc, M. S. Stojanovıc and M. Kindermann.** 2009, Phys. Rev. B, Vol. 80, p. 045410.

171. *Ab Initio Periodic Simulation of the Spectroscopic and Optical Properties of Novel Porous Graphene Phases.* **M. De La Pierre, P. Karamanis, J. Baima, R. Orlando, C. Pouchan, and R. Dovesi.** 2013, J. Phys. Chem. C, Vol. 117, p. 2222−2229.

172. *A Nonzero Gap Two-Dimensional Carbon Allotrope from Porous Graphene.* **G. Brunetto, P. A. S. Autreto, L. D. Machado, B. I. Santos, R. P. B. dos Santos, D. S. Galvão.** 2012, J. Phys. Chem. C, Vol. 116, pp. 12810-12813.

173. *Definitive Band Gaps for Single-Wall Carbon Nanotubes.* **Y. Matsuda, J. Tahir-Kheli, W.A. III Goddard.** 2010, J. Phys. Chem. Lett., Vol. 1, p. 2946.

174. *Selective Ion Passage through Functionalized Graphene Nanopores.* **K.Sint, B. Wang and P. Kral.** 2008, J. Am. Chem. Soc., Vol. 130, pp. 16448-16449.

175. *Energy Band-Gap Engineering of Graphene Nanoribbons.* **M.Y. Han, B. Oylmaz, Y. Zhang and P. Kim.** 2007, Phys. Rev. Lett., Vol. 98, pp. 206805-4.

176. *Electron beam nanosculpting of suspended graphene sheets.* **M.D. Fishbein, and M. Drndic.** 2008, Appl. Phys. Lett., Vol. 93, p. 113107.

177. *Nitrogen assisted etching of graphene layers in a scanning electron microscope.* **D. Fox, A. O'Neill, D. Zhou, M. Boese, J. N. Coleman and H. Z. Zhang.** 2011, Appl. Phys. Lett., Vol. 98, p. 243117 .

178. *Photochemical Engineering of Graphene Oxide Nanosheets.* **M. Koinuma, C. Ogata, Y. Kamei, K. Hatakeyama, H. Tateishi, Y. Watanabe, T. Taniguchi, K. Gezuhara, S. Hayami, A. Funatsu, M. Sakata, Y. Kuwahara, S. Kurihara and Y. Matsumoto.** 2012, J. Phys. Chem. C, Vol. 116, pp. 19822-198227.

179. *Large-scale production of porous graphene and graphene quantum dots by femtosecond laser ablation of highly oriented*

pyrolytic graphite in water. **P. Russo, A. Hu, G. Compagnini, W. W. Duley, and N. Y. Zhou.** Submitted to Nanoscale.

180. *Luminscent Graphene Quantum Dots for Organic Photovoltaic Devices.* **V. Gupta, N. Chaudhary, R. Srivastava, G. D. Sharma, R. Bhardwaj and S. Chand.** 2011, J. Am. Chem. Soc., Vol. 133, pp. 9960-9963.

181. *Quantum Dots for Live Cells, in Vivo Imaging, and Diagnostics.* **X. Michalet, F.F. Pinaud, L.A. Bentolila, J.M. Tsay, S. Doose, J.J. Li, G. Sundaresan, A.M. Wu, S.S. Gambhir and S. Weiss.** 2005, Science, Vol. 307, pp. 538-544.

182. *Hydrothermal Route for Cutting Graphene Sheets Into Blue-Luminescent Graphene Quantum Dots.* **D. Pan, J. Zhang, Z. Li and M. Wu.** 2010, Adv. Mater., Vol. 22, pp. 734-738.

183. *Cutting sp2 clusters in graphene sheets into colloidal graphene quantum dots with strong green fluorescence.* **D. Pan, L. Guo, J. Zhang, C. Xi, Q. Xue, H. Huang, J. Li, Z. Zhang, W. Yu, Z. Chen, Z. Li and M. Wu.** 2012, J. Mater. Chem., Vol. 22, pp. 3314-3318.

184. *Focusing on luminescent graphene quantum dots: current status and future perspectives.* **L. Li, G. Wu, G. Yang,J. Peng, J. Zhao, J. J Zhu.** 2013, Nanoscale, Vol. 5, pp. 4015-4039.

185. *Deep Ultraviolet Photoluminescence of Water-Soluble Self-Passivated Graphene Quantum Dots.* **L. Tang, R. Ji, X. Cao, J. Lin, H. Jiang, X. Li, K. S. Teng, C. M. Luk, S. Zeng, J. Hao and S. P. Lau.** 2012, ACS Nano, Vol. 6, pp. 5102-5110.

186. *Anomalous Behaviors of Visible Luminescence from Graphene Quantum Dots: Interplay between Size and Shape.* **S. Kim, S. W. Hwang, M.-K Kim, D. Y. Shin, D. H. Shin, C. O. Kim, S. B. Yang, J. H. Park, E. Hwang, S.-H. Choi, G. Ko, S. Sim, C. Sone, H. J. Choi, S. Bae, and B. H. Hong.** 2012, ACS Nano, Vol. 6, pp. 8203–8208.

187. *Semiconductor Clusters, Nanocrystals, and Quantum Dots.* **A. P. Alivisatos.** 1996, Science, Vol. 271, pp. 933-937.

188. *Strongly green-photoluminescent graphene quantum dots for bioimaging applications.* **S. Zhu, J. Zhang, C. Qiao, S. Tang, Y. Li, W. Yuan, B. Li, L. Tian, F. Liu, R. Hu, H. Gao, H. Wei, H. Zhang, H. Sun and B. Yang.** 2011, Chem. Commun., Vol. 47, pp. 6858-6860.

189. *Carbon nanodots: synthesis, properties and applications.* **H. Li, Z. Kang, Y. Liu and S.-T. Lee.** 2012, J. Mater. Chem., Vol. 22, pp. 24230-24253.

190. *Surface Chemistry Routes to Modulate the Photoluminescence of Graphene Quantum Dots: From*

Fluorescence Mechanism to Up-Conversion Bioimaging Applications. **S. Zhu, J. Zhang, S. Tang, C. Qiao, L. Wang, H. Wang, X. Liu, B. Li, Y.Li, W. Yu, X. Wang, H. Sun and B. Yang.** 2012, Adv. Funct. Mater., Vol. 22, pp. 4732-4740.

191. *Luminscent Graphene Quantum Dots for Organic Photovoltaic Devices.* **V. Gupta, N. Chaudhary, R. Srivastava, G. D. Sharma, R. Bhardwaj and S. Chand.** 2011, J. Am. Chem. Soc., Vol. 133, pp. 9960–9963.

192. *Blue luminescent graphene quantum dots and graphene oxide prepared by tuning the carbonization degree of citric acid.* **Y. Q. Dong, J. W. Shao, C. Q. Chen, H. Li, R. X. Wang, Y. W. Chi, X. M. Lin and G. N. Chen.** 2012, Carbon, Vol. 50, pp. 4738-4743.

193. *Titanium Dioxide Nanomaterials: Synthesis, Properties, Modifications, and Applications.* **Mao., X. Chen and S.S.** 2007, Chem. Rev., Vol. 107, pp. 2891–2959.

194. *Water Soluble Fluorescent Carbon Quantum Dots and Photocatylist Design.* **H. Li, X. He, Z. Kang, H. Huang, Y. Liu, J. Liu, S. Lian, C. A. Tsang, X. Yang and S.-T Lee.** 2010, Angew. Chem. Int. Ed. , Vol. 49, pp. 4430-4434.

195. *Use of Ultrafiltration Membranes for the Separation of TiO2 Photocatalysts in Drinking Water Treatment. .* **S.-A. Lee, K.-H**

Choo, C.-H. Lee, H.-I. Lee, T. Hyeon. W. Choi, and H.-H. Kwon. 2001, Ind. Eng. Chem. Res., Vol. 40, pp. 1712-1719.

196. *Carbon quantum dot sensitized TiO2 nanotube arrays for photoelectrochemical hydrogen generation under visible light.* **X. Zhang, F.Wang, H. Huang, H. Li, X. Han, Y. Liu and Z. Kang.** 2013, Nanoscale , Vol. 5, pp. 2274-2278.

197. *Recent Applications of TiO2 Nanomaterials in Chemical Sensing in Aqueous Media.* **J. Qiu, S. Zhang and H. Zhao..** 2011, Sensor Actuator B Chem. , Vol. 160, pp. 875-890.

198. *Photocatalytic Activity of a TiO2 Photocatalyst Doped with C4+ and S4+ Ions Having a Rutile Phase Under Visible Light.* **T. Ohno, T. Tsubota, M.Toyofuku, and R. Inaba.** 2004, Catalysis Letters , Vol. 98, pp. 255-258.

199. *TiO2/Graphene Composite from Thermal Reaction of Graphene Oxide and its Photocatalytic Activity in Visible Light.* **Pan., Y. Zhang and C.** 2011, J. Mater. Sci., pp. 2622-2626.

200. *Organic Photovoltaic Devices Using Highly Flexible Reduced Graphene Oxide Films as Transparent Electrodes.* **Z. Yin, S. Sun, T. Salim, S. Wu, X. Huang, Q. He, Y. M. Lam and H. Zhang.** 2010, ACS Nano, Vol. 4, pp. 5263-5268.

201. *Facile Preparation and Upconversion Luminescence of Graphene Quantum Dots.* **J. Shen, Y. Zhu, C. Chen, X. Yang and C. Li.** 2011, Chem. Commun., Vol. 47, pp. 2580-2582.

202. *Photo-Fenton Reaction of Graphene Oxide: A new strategy to Prepare Graphene Quantum Dots for DNA Cleavage.* **X. Zhou, Y. Zhang, C. Wang, X. Wu, Y. Yang, B. Zheng, H. Wu, S. Guo and J. Zhang.** 2012, ACS Nano, Vol. 6, pp. 6592-6599.

203. *Large, Solution-Processable Graphene Quantum Dots as Light Absorbers for Photovoltaics.* **X. Yan, X. Cui, B. Li and L.S. Li.** 2010, Nano Lett., Vol. 10, pp. 1869-1873.

204. *Oxidation of Tartaric Acid in the Presence of Iron.* **Fenton., H. J. H.** 1894, J. Chem. Soc., Vol. 65, pp. 899–910.

205. *Visible-Light-Assisted Degradation of Dye Pollutants over Fe(III)-Loaded Resin in the Presence of H2O2 at Neutral pH Values.* **M. Cheng, W. Ma, J. Li, Y. Huang and J. Zhao.** 2004, Environ. Sci. Technol., Vol. 38, pp. 1569–1575.

206. *Aqueous Pesticide Degradation by Hydrogen Peroxide/Ultraviolet Irradiation and Fentontype Advanced Oxidation Processes: A Review.* **El-Din., K. Ikehata and M. G.** 2006, J. Environ. Eng. Sci., Vol. 5, pp. 81–135.

207. *The Photo-Fenton Oxidation -A Cheap and Efficient Wastewater Treatment Method.* **R. Fallmann, and H. Bauer.** 1997, Res. Chem. Intermed., Vol. 23, pp. 341–354.

208. *Determination of the Local Chemical Structure of Graphene Oxide and Reduced Graphene Oxide.* **K. Erickson, R. Erni, Z. Lee, N. Alem, W. Gannett and A. Zettl.** 2010, Adv. Mater., Vol. 22, pp. 4467–4472.

209. *Graphene Thickness Determination Using Reflection and Contrast Spectroscopy.* **Z. H. Ni, M. H. and Wang, J. Kasim, H. M. Fan, T. Yu, Y. H. Wu, Y. P. Feng, and Z. X. Shen.** 2007, Nano Lett., Vol. 7, pp. 2758-2763.

210. *Structure and Performance of Porous Graphitic Carbon in Liquid Chromatography.* **J. H. Knox, K. Bulvinder, and G. R. Millward.** 1986, Journal Of Chromatography, Vol. 352, pp. 3-25.

211. *Examining the Stability of Folded Graphene Edges Against Electron Beam Induced Sputtering with Atomic Resolution.* **J. H. Warner, M. H. Rummeli, A. Bachmatiuk, and B. Buchner.** 2010, Nanotechnology , Vol. 21, pp. 325702-6.

212. *Examining the Edges of Multi-Layer Graphene Sheets.* **J. H. Warner, F. Schaffel, M. H. Rummeli, and B. Buchner.** 2009, Chem. Mater. , Vol. 21, pp. 2418-2421.

213. *Identification of Nano-sized Holes by TEM in the Graphene Layer of Graphite and the High Rate Discharge Capability of Li-ion battery anodes.* **T. Takamura, K. Endo, L. Fu, Y. Wu, K. J. Lee, and T. Matsumoto.** 2007, Electrochimica Acta, Vol. 53, pp. 1055–1061.

214. *Direct Evidence for Atomic Defects in Graphene Layers. .* **A. Hashimoto, K. Kazusuenaga, A. Gloter, K. Urita, and S. Iijima.** 2004, Nature, Vol. 430, pp. 870-873.

215. *Direct Imaging of LatticeAtoms and Topological Defects in Graphene Membranes.* **J. C. Meyer, C. Kisielowski, R. Erni, M. D. Rossell, M. F. Crommie, and A. Zettl.** 2008, Nano Lett., Vol. 8, pp. 3582-3586.

216. *An Electrochemical Avenue to Blue Luminiscent Nanocrystals from Multiwalled Carbon Nanotubes (MWCNTs).* **J. Zhou, C. Booker, R. Li, X. Zhou, T-K. Sham, X. Sun and Z. Ding.** 2007, J. Am. Chem. Soc., Vol. 129, pp. 744-745.

217. *Lossless Synthesis of Graphene Nanosheets Decorated with Tiny Cadmium Sulfide Quantum Dots with Excellent Nonlinear Optical Properties.* **M. Feng, R. Sun, H. H. Zhan and Y. Chen.** 2010, Nanotechnology , Vol. 21, pp. 075601-7.

218. *Graphene Nanosheets for Enhanced Lithium Storage in Lithium Ion Batteries.* **G. Wang, X. Shen, J. Yao and J. Park.** 2009, Carbon, Vol. 47, pp. 2049-2053.

219. *Focusing on luminescent graphene quantum dots: current status and future perspectives.* **L. Li, G.i Wu, G. Yang, J. Peng, J. Zhao and J.-J. Zhu.** 2013, Nanoscale, Vol. 5, pp. 4015-4039.

220. *Creating High Yield Water Soluble Luminescent Graphene Quantum Dots Via Exfoliating and Disintegrating Carbon Nanotubes and Graphite Flakes.* **L. Lin, and S. Zhang.** 2012, Chem. Commun. , Vol. 48, pp. 10177-10179.

221. *Generation of H2, O2, and H2O2 From Water by the use of Intense Femtosecond Laser Pulses and the Possibility of Laser Sterilization.* **S. L. Chin, and S. Lagace.** 1996, Appl.Opt., Vol. 35, pp. 907-11.

222. **Smoot, L. D. Smith. and P. J.** Gasification of Coal in Practical Flames. *Coal Combustion and Gasification.* s.l. : D. Luss., 1985, pp. 151-162.

223. *Laser Ablation in Liquids: Applications in the Synthesis of Nanocrystals.* **G.W. Yang.** 2007, Prog. Mater. Sci., Vol. 52, pp. 648–698.

224. *Direct Synthesis of Polyyne Molecules in Acetone by Dissociation Using Femtosecond Laser Irradiation.* **A. Hu, J. Sanderson, A. A. Zaidi, C. Wang, T. Zhang, Y. Zhou and W. W. Duley.** 2008, Carbon, Vol. 46, pp. 1823-1825.

225. *Polyynes: a New Class of Carbon Allotropes. About the Formation of Dicyanopolyynes From an Electric Arc Between Graphite Electrodes in Liquid Nitrogen.* **Cataldo., F.** 2004, Polyhedron, Vol. 23, pp. 1889–1896.

226. *Cyanopolyynes: Carbon Chains Formation in a Carbon Arc Mimicking the Formation of Carbon Chains in the Circumstellar Medium.* **Cataldo, F.** 2004, International Journal of Astrobiology, Vol. 3, pp. 237–246.

227. *Polyynes and Cyanopolyynes Synthesis from the Submerged Electric Arc: About the Role Played by the Electrodes and Solvents in Polyynes Formation.* **Cataldo., F.** 2004, Tetrahedron, Vol. 60, pp. 4265–4274.

228. *Organic molecules in the Interstellar Medium, Comets, and Meteorites: A Voyage from Dark Clouds to the Early Earth.* **P. Ehrenfreund, and S. B. Charnley.** 2000, Annu. Rev. Astron. Astrophys., Vol. 38, pp. 427–483.

229. *Raman and Surface-Enhanced Raman Scattering of a Series of Size-Separated Polyynes.* **H. Tabata, M. Fujii, S.**

Hayashi, T. Doi and T. Wakabayashi. 2006, Carbon, Vol. 44, pp. 3168–3176.

230. *Raman and SERS Investigation of Isolated sp Carbon Chains.* **A. Lucotti, M. Tommasini, M. Del Zoppo, C. Castiglioni, G. Zerbi, F. Cataldo, C. S. Casari, A. Li Bassi, V. Russo, M. Bogana and C. E. Bottani.** 2006, Chem. Phys.Lett., Vol. 417, pp. 78–82.

231. *Raman Spectroscopy of Size-Selected Linear Polyyne Molecules C2nH2 (n = 4-6) Encapsulated in Single-Wall Carbon Nanotubes.* **D. Nishide, T. Wakabayashi, T. Sugai, R. Kitaura, H. Kataura, Y. Achiba and H. Shinohara.** 2007, J. Phys. Chem. C, Vol. 111, pp. 5178-5183.

232. *Surface-Enhanced Raman Scattering from Polyyne Solutions.* **H. Tabata, M. Fujii and S. Hayashi.** 2006, Chem. Phys. Lett., Vol. 420, pp. 166–170.

233. *Spectroscopic Characterization of Carbon Chains in Nanostructured Tetrahedral Carbon Films Synthesized by Femtosecond Pulsed Laser Deposition.* **A. Hu, Q.-B. Lu, W. W. Duley and M. Rybachuk.** 2007, J. Chem. Phys., Vol. 126, pp. 154705-5.

234. *On the Mechanism of Carbon Clusters Formation Under Laser Irradiation. The Case of Diamond Grains and Solid C60*

Fullerene. **Keheyan, F. Cataldo and Y.** 2002, Fullerenes, Nanotubes and Carbon Nanostructures, Vol. 10, pp. 313-332.

235. *Surface Enhanced Raman Spectroscopic Characterization of Molecular Structures in Diamond-Like Carbon Films.* **A. Hu and W. W. Duley.** 2008, Chem. Phys. Lett., Vol. 450, pp. 375–378.

236. *Raman spectra of polycyclic aromatic hydrocarbons. Comparison of Calculated Raman intensity distributions with Observed Spectra for Naphthalene, Anthracene, Pyrene, and Perylene.* **H. Shinohara, Y. Yamakita and K. Ohno.** 1998, Journal of Molecular Structure, Vol. 442, pp. 221-234.

237. *A Simple Predictive Model for Molecular Vibrations of Polycyclic Aromatic Hydrocarbons: An Extended Version of the MO/8 Model.* **K. Ohno, R. Takahashi, M. Yamada and Y. Isogai.** 2002, Internet Electron. J. Mol. Des., Vol. 1, pp. 636–658. http://www.biochempress.com..

238. *Cyanopolyynes: Carbon Chains Formation in a Carbon Arc Mimicking the Formation of Carbon Chains in the Circumstellar Medium.* **Cataldo, F.** 2004, International Journal of Astrobiology, Vol. 3, pp. 237–246.

239. *Polycyclic Aromatic Hydrocarbon Formation in Carbon-Rich Stellar Envelopes.* **I. Cherchneff, J. R. Barker and A. G.**

Tielens. 1992, The Astrophysical Journal, Vol. 401, pp. 269-287.

List of Publications

1. Paola Russo, Anming Hu, Giuseppe Compagnini, Walter W. Duley, and Norman Y. Zhou, "Femtosecond laser ablation of highly oriented pyrolytic graphite: green route for large-scale production of porous graphene and graphene quantum dots", Submitted to Nanoscale (2013)
2. Russo, Paola; Hu, Anming; Compagnini, Giuseppe, "Synthesis, properties and potential applications of porous graphene: a review", Nano-Micro Lett. 5(4), 260-273 (2013).
3. P. Russo, G. Compagnini, C. Musumeci, B. Pignataro; "Raman monitoring of strain induced effects in mechanically deposited single layer graphene", Journal of Nanoscience and Nanotechnology, 12, 8755-8758, (2012).
4. G.Compagnini, P. Russo, F.Tomarchio, O. Puglisi, L.D'Urso, S. Scalese; "Laser assisted green synthesis of free standing reduced graphene oxides at the water–air interface". Nanotechnology, 23, 505601, (2012).

5. G. Compagnini, M. Sinatra, P. Russo, G. Messina, O. Puglisi, S. Scalese; "Deposition of fewlayer graphene nanowalls at the electrodes during electric field-assisted laser ablation of carbon in water". Carbon, 50, 6, 2362-2365, (2012).
6. L. D'Urso, G. Forte, P. Russo, C. Caccamo, G. Compagnini, O. Puglisi; "Surface-enhanced Raman Scattering study on 1D-2D graphene-based structures"; Carbon 49, 10, 3149-3157, (2011).
7. S. Scalese, V. Scuderi, S. Bagiante, S. Fabiano, P. Russo, L. D'Urso, G. Compagnini, V. Privitera; "Controlled synthesis of carbon nanotubes and linear carbon chains by arc discharge in liquid", Journal of Applied Physics, 107, 014304, (2010).

Acknowledgements

I would like to thank Professor Giuseppe Compagnini, my research supervisor, for his support and guidance throughout these years.

I would like also to express my sincere gratitude to Professor Norman Zhou and Professor Anming Hu for the possibility to work at the University of Waterloo at the Department of Mechanical and Mechatronics engineering in Canada. I thank all the group members of CAMJ group. I am grateful to Sally Seibert, the kindest woman I have ever met. During the time I spent in Canada, she made me feel like I was at home. Thanks also to her sister Diane and her friends Marilyn, Sheila and Shirley.

I would like to offer my thanks to Dr. Silvia Scalese at CNR-IMM of Catania for SEM images, to Professor Francesca Simone at the Physics Departments for the experimental setup for the fabrication of GNWs, and to Professor Franco Cataldo at University of Roma "Tor Vergata" for his help for providing me comments and suggestions.

I am grateful to my research group the LABFSN Research Group for the support and the many discussions about science and in particular, about life…

I wish to thank Tirdad, Carmela, Chiara P. and Chiara G. for their support, friendship and love. They are always there for me, no matter where I am or where I will be.

My warmest thanks go to my parents and family for their endless love, support and encouragement. Thanks for everything!!